Solvothermal Synthesis of Rare Earth Oxides and Rare-Earth-Based Mixed-Oxides(Dissertation_全文)

AUTHOR(S):

Hosokawa, Saburo

Solvothermal Synthesis of Rare Earth Oxides and Rare–Earth–Based Mixed–Oxides

Saburo Hosokawa

2007

Solvothermal Synthesis of Rare Earth Oxides and Rare–Earth–Based Mixed–Oxides

Saburo Hosokawa

2007

Contents

General Introduction

It is generally accepted that rare earth (RE) elements include the group 3 elements scandium and yttrium and the lanthanide group from lanthanum to lutetium. RE elements have peculiar properties that differ from those of other elements. The peculiarity arises from their unique electronic configurations and radial distribution functions in 4f orbitals. The electronic configuration of the outermost shell of a trivalent lanthanide ion is $5s^2 5p^6$, and 4f orbitals exist deep inside the 5s and 5p orbitals (Fig. 1). Since the electron clouds of 5s and 5p orbitals shroud that of 4f orbitals, the extensity of the electrons in the 4f orbitals is small. An electron is first introduced into one of the seven-fold degenerate 4f orbitals of cerium (III) ion, and all 4f orbitals are finally filled with 14 electrons in lutetium (III) ion (Table 1). A characteristic of RE elements is that the 4f orbitals exist deep in the atom and are not completely filled with electrons. A phenomenon known as lanthanoid contraction—a monotonous decrease in the ionic size with an increase in the atomic number—results from the peculiar electronic states in 4f orbitals. Recently, RE elements have been used to produce phosphor, magnetic material, hydrogen storage alloy, fuel cell, solid electrolyte, catalyst, superconductors, etc [1].

Typically, RE ions in RE oxides take a trivalent state with the general formula RE_2O_3. However, some RE elements take divalent or tetravalent states, and in the case of Ce, Pr, and Tb, intermediate states also appear as REO_{2-x} [2]. RE mixed oxides such as $REMeO_3$ (Me = transitional metals) with a perovskite structure and $RE_3Me_5O_{12}$ (Me: Al, Ga, etc.) with a garnet structure are also known to exist. The former is used as a high-temperature superconductivity material, while the latter is used to form matrices for laser emission [3].

Recently, remarkable progress has been made in the development of metal oxide nanoparticles. Further, it is expected that the properties of nanoparticles obtained by

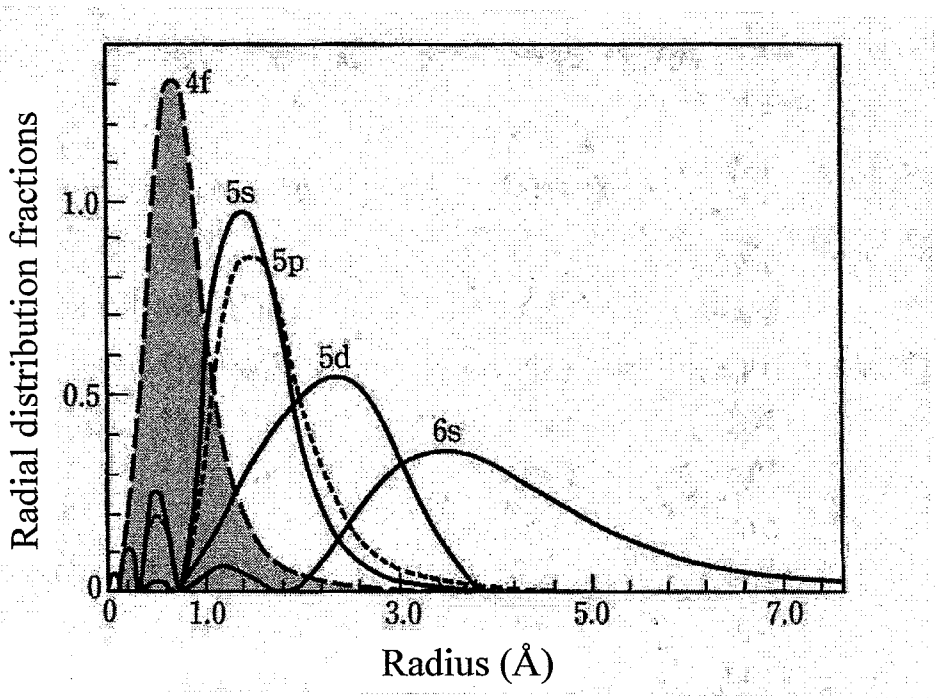

Fig. 1. Radial distribution functions for 4f, 5s, 5d and 6s orbitals [3].

Table 1 Electron configurations of rare earth elements (3+).

Sc	$[Ne]3s^2 3p^6$	Gd	$[Xe]4f^7 5s^2 5p^6$
Y	$[Ar]3d^{10} 4s^2 4p^6$	Tb	$[Xe]4f^8 5s^2 5p^6$
La	$[Kr]4d^{10} 5s^2 5p^6$	Dy	$[Xe]4f^9 5s^2 5p^6$
Ce	$[Xe]4f^1 5s^2 5p^6$	Ho	$[Xe]4f^{10} 5s^2 5p^6$
Pr	$[Xe]4f^2 5s^2 5p^6$	Er	$[Xe]4f^{11} 5s^2 5p^6$
Nd	$[Xe]4f^3 5s^2 5p^6$	Tm	$[Xe]4f^{12} 5s^2 5p^6$
Pm	$[Xe]4f^4 5s^2 5p^6$	Yb	$[Xe]4f^{13} 5s^2 5p^6$
Sm	$[Xe]4f^5 5s^2 5p^6$	Lu	$[Xe]4f^{14} 5s^2 5p^6$
Eu	$[Xe]4f^6 5s^2 5p^6$		

these techniques will differ from those of bulk particles. The new properties of nano-sized metal particles are derived from the defect structure in the crystal, size and its distribution, morphology of the primary particle, peculiar aggregation state that is caused by the unusual charged state of the particle surface during the aggregation process, etc.

It is expected that RE oxide nanoparticles exhibit peculiar properties such as superplasticity due to their small particle sizes. For example, $Y_2O_3:Eu^{3+}$ is used as a red light emission material in fluorescence lamps. Sharma et al. have reported that the luminescence intensity of $Y_2O_3:Eu^{3+}$ is stronger with smaller particles (10 nm) [4]. RE oxides can be used as catalysts or catalyst supports [5–8]. Therefore, it is very interesting to develop methods for synthesizing nano-sized RE oxides with large surface areas.

In a simple method for synthesizing RE oxide composed of a single RE metal species, RE hydroxide is precipitated from the corresponding aqueous RE nitrate by adding alkali solutions such as aqueous ammonium hydroxide or ammonium carbonate [9]. Then, the precipitate is dried and calcined. The concentration of the precipitating agents may become heterogeneous in the solution during particle formation. To avoid the concentration heterogeneity of the precipitating agents, urea can be used while heating [10].

$$(NH_2)_2CO + 3H_2O \rightarrow 2NH_4^+ + CO_2 + 2OH^-$$

The precipitation proceeds under the same condition through the solution due to mild and homogeneous decomposition of urea. This method is referred to as the homogeneous precipitation method. However, the resulting RE oxides have low surface areas due to the aggregation of particles during drying, particularly, during the vaporization of water whose surface tension is high.

RE oxide nanoparticles cannot be obtained by calcination or thermal decomposition of RE acetate or oxalate in air because RE carbonate oxides formed as intermediates remain stable up to high temperatures (600–800 °C) [11–13].

Recently, many studies have been conducted on the syntheses of RE oxide nanoparticles by using organic compounds [14–20]. For example, $Y(OH)_3$ is precipitated by adding aqueous $Y(NO_3)_3$ to aqueous ammonium hydroxide. The aggregation of the resulting hydroxide particles is prevented by a polymer surface modification agent added before the precipitation process [4]. It is reported that the particle size can be controlled by changing the concentration of the surface modification agent, and Y_2O_3 nanoparticles (10 nm) are obtained. Masui et al. have reported that ultrafine CeO_2 particles (2.6 nm) have been prepared by a reaction in reversed micelles formed with a surfactant in oil [21]. The ultrafine particles are obtained by mixing water-in-oil microemulsions containing cerium nitrate solution with those containing ammonium hydroxide. $Y_2O_3:Eu^{3+}$ phosphor nanoparticles (~8 nm) are obtained by a combustion method, i.e., co-ignition of RE nitrate and glycin [22].

Recently, morphology control of RE oxides has attracted considerable attention. Shape-controlled RE oxides are highly valuable; for example, for CO oxidation, rod-shaped or spindle-like CeO_2 particles have higher activity than spherical CeO_2 particles [23]. One-dimensional or hollow shaped RE oxides have been synthesized. In this case, a gel prepared by a sol-gel or homogeneous precipitation method is laminated on various templates such as an alumina anode or micelle formed with surfactants; this process is followed by the elimination of the template and calcination [24–26].

Powders of RE mixed oxides with the perovskite structure are used not only as photocatalysts [27] but also as catalysts for automotive exhaust gas purification [28] or NO decomposition [29]. Mixed oxides with the garnet structure, particularly $Y_3Al_5O_{12}$,

are used as phosphors [30]. Therefore, RE mixed oxides can potentially be used as advanced ceramic materials, and it is crucial to synthesize RE mixed oxide nanoparticles with high surface areas.

Since mixed oxides are composed of various metal species, the homogeneity of the metal species in the precursors before calcination determines the crystal phases or physical properties of the mixed oxides. Therefore, methods for the synthesis of mixed oxides are different from those for single component metal oxides. Solid-phase reaction is one of the classical methods. In this method, mixed oxides are synthesized by the high-temperature calcination of combined metal oxides or carbonates that are physically mixed beforehand and crushed to microparticles by ball milling. When the desired products are mixed oxides with structures such as perovskite, garnet, and pyrochlore structures, heat treatment at high temperatures (>1000 °C) is required. However, this process sometimes yields oxides with the pseudomorphs of the desired product or the starting materials remain intact. Therefore, repeated crushing and calcination must be carried out repeatedly to obtain phase-pure mixed oxides. Moreover, when a large amount of thermal energy is applied to decompose the precursors, it causes sintering of the product particles.

Liquid phase syntheses are preferred to prepare inorganic materials with well-defined morphologies. These synthetic reactions proceed at relatively lower temperatures and therefore require lower energies; the sol-gel (alkoxyide) method and coprecipitation method are typical examples of such syntheses. In the coprecipitation method, a precursor product is obtained by adding an alkali solution to a solution containing target metal ions. In the sol-gel method, metal alkoxides are hydrolyzed to yield corresponding metal hydroxides, and the precursor products are obtained by the condensation polymerization of the hydroxides. The calcination of these precursor products is required in order to obtain crystallized products. However, the

reproducibility of these two methods may sometimes be poor depending on various factors such as the reaction temperature, pH of the solution, and rate of precipitation or hydrolysis. The phase separation can occur due to the heterogeneous distribution of metal atoms in the precursor products caused by various factors. Recently, Liu et al. have reported the synthesis of $Y_3Al_5O_{12}$ nanoparticles by the coprecipitation method using ultrasonic waves [31]. The precursor powder thus obtained can be crystallized into the $Y_3Al_5O_{12}$ phase by calcination at a low temperature of 900 °C for 2 h due to the uniform distribution of Al and Y ions; a solid-phase reaction requires considerably higher temperatures (>1600 °C) and prolonged calcination time. To the author's knowledge, $Y_3Al_5O_{12}$ particles obtained by this method have the smallest particle size (15 nm).

New methods such as the polymerized complex method have been developed in which organic solvents are used to obtain mixed oxides with a highly uniform distribution of the constituent metal atoms. The polymerized complex method can be explained by a simple chemical scheme in which a mixture of ethylene glycol and citric acid containing pertinent metal ions is polymerized to form a polyester-type resin with a random distribution of the metal ions. The calcination of the resin yields mixed metal oxide. Because the mobility of the metal ions in the polyester-type resin is low, their aggregation or segregation during calcination can be prevented. Consequently, the composition of the mixed oxide is uniform at the atomic level. For example, the crystallization of $LaAlO_3$ synthesized by the polymerized complex method occurs at a temperature (750 °C) that is significantly lower than that in solid-phase reactions (1500–1700 °C) [32]. Therefore, the surface area of $LaAlO_3$ synthesized by the polymerized complex method (15 m^2/g) is larger than that of $LaAlO_3$ prepared by the solid-phase reaction (0.3 m^2/g). Other mixed oxides (e.g., $RE_2Ti_2O_7$ [32], Y_3NbO_7 [32], and $Y_3Al_5O_{12}$ [33]) synthesized by the polymerized complex method are also

crystallized at low temperatures.

There are various methods for synthesizing inorganic materials, as described above. Recently, the syntheses of inorganic materials by a solvothermal reaction have been actively studied. When the term "solvothermal" is searched in the *Web of Science*, it is observed that the number of pertinent papers has drastically increased in recent time, as shown in Fig. 2. This term is used for reactions in liquids or supercritical media at temperatures higher than their boiling points [34]. Although hydrothermal reactions or reactions in NH_3 and HF solutions are also types of solvothermal reactions, "solvothermal" is used in this dissertation to refer to the reactions in organic media.

Most of the solvothermal products are nano- or microparticles with well-defined morphologies. The distribution of the particle size of the products is usually very narrow; the formation of monodispersed particles has been reported frequently [35]. When solvent molecules or additives are preferentially adsorbed on (or have a specific interaction with) a certain surface of a product, the growth of the surface is inhibited, and therefore a product with a unique morphology can be formed. Thus, various types of products (nanorods, wires, tubes, and sheets) have been obtained by this reaction [36, 37].

Regarding the synthesis of RE oxide, Demazeau et al. reported that well-crystallized CeO_2 particles were prepared by the solvothermal reaction of a colloidal suspension of $Ce(OH)_4$ in ethanol. The thermal stability of CeO_2 synthesized by this method was higher than that of CeO_2 obtained by a hydrothermal reaction [38]. Nano-sized $Y_3Al_5O_{12}:Ce^{3+}$ particles were synthesized from a precursor by a solvothermal reaction in ethanol. The precursor was precipitated from a stoichiometric mixture of aluminum and yttrium nitrates with ammonium hydrogen carbonate in the presence of a small amount of cerium nitrate [39]. The crystallite and particle sizes of $Y_3Al_5O_{12}$ were 14.6

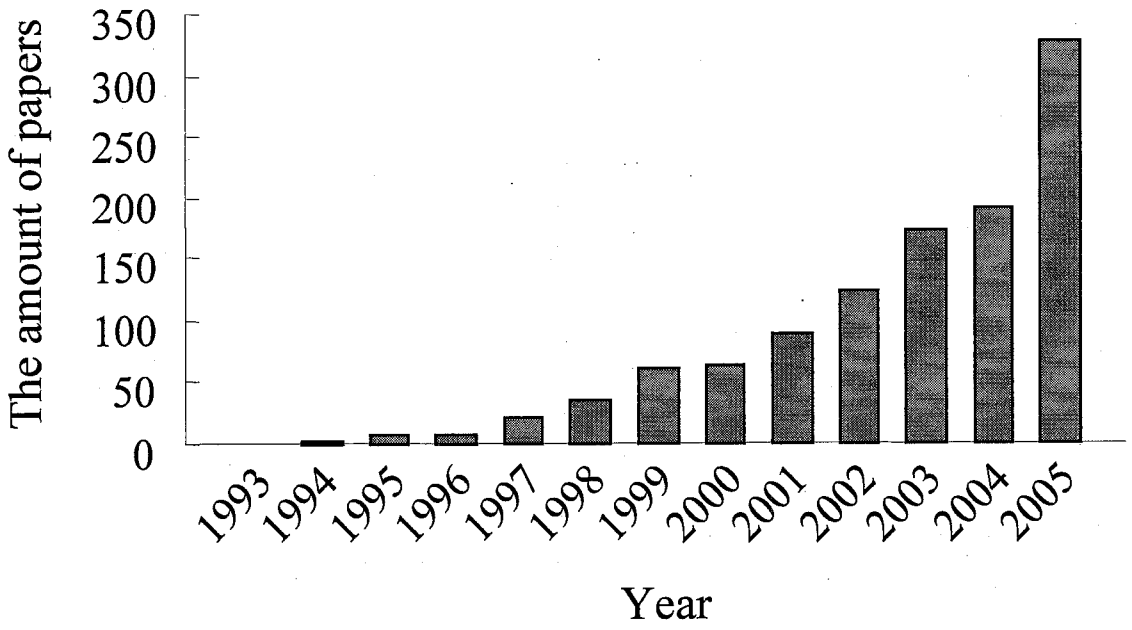

Fig. 2. The search results for the annual number of the papers which use the term "solvothermal".

nm and 60 nm, respectively. Kominami et al. reported that an amorphous product, which was obtained by the solvothermal decomposition of $La(OiPr)_3$ and $Fe(Obu)_3$ in toluene, was crystallized into perovskite-type $LaFeO_3$ in the subsequent solvothermal treatment in 1,4-butanediol [40].

Since 1984, Inoue et al. have actively investigated various methods for the synthesis of inorganic materials by solvothermal reactions at elevated temperatures (200–300 °C) under autogeneous pressures of organic media [41]. A transparent colloidal solution of ultrafine particles (particle size, 2–4 nm) of CeO_2 is directly obtained by the reaction of Ce metal in 2-methoxyethanol at 200–300 °C [42]. Various oxides (TiO_2 [43], ZrO_2 [44], etc.) and mixed oxides ($ZnAl_2O_4$ [45], Ga_2O_3-Al_2O_3 solid solutions [46], etc.) are also directly crystallized under mild conditions when suitable starting materials such as metal alkoxide, acetylacetonate, or acetate are allowed to react in 1,4-butanediol at 200–300 °C. This solvothermal reaction using glycols as the organic solvents is termed "glycothermal reaction." For the syntheses of RE mixed oxides, glycothermal reactions in 1,4-butanediol yielded $REPO_4$ [34], $REVO_4$ [47], RE_3NbO_7 [48], $RE_3Al_5O_{12}$ [49], $RE_3Ga_5O_{12}$ [50], and $REFeO_3$ [51].

The properties or morphologies of inorganic materials synthesized by solvothermal reactions in organic media differ significantly from those of the compounds synthesized in water (coprecipitation, sol-gel methods, etc.) [52, 53]. Therefore, RE oxides or mixed oxides synthesized by solvothermal reactions have high potential to serve as functional materials in various fields .

With this background the present thesis focuses on the synthesis of RE oxides or mixed oxides by solvothermal reactions.

The solvothermal reactions of RE metals in 2-methoxyethanol and 2-aminoethanol are described in Chapter 1. Transparent colloidal solutions of CeO_2, Sm_2O_3, and Yb_2O_3

were obtained by the solvothermal reactions. Their particle sizes were extremely small in the range of 2–3 nm.

Chapter 2 deals with the thermal decomposition behavior of the products synthesized by the glycothermal treatment of RE acetates in vic-glycol (ethylene glycol, 1,2-propanediol, and 1,2-butanediol). The physical properties of the RE oxides obtained by thermal decomposition are clarified. The RE oxide nanoparticles (RE = Gd-Yb, Y) obtained by the glycothermal treatment of RE acetates in 1,2-propanediol and the subsequent calcination had remarkably high surface areas.

Chapter 3 deals with further analysis of the morphology of the RE oxides obtained by the glycothermal treatment of RE acetate in 1,2-propanediol and the subsequent calcination. RE_2O_3 with a high surface area was a nano-hollow shaped particle.

Chapter 4 explains the solvothermal treatment of RE chloride hydrates in the presence of amine bases to neutralize liberated HCl. The crystalline structures of the products are clarified, and the relationship between the crystalline structure and the ionic size of the RE elements is described.

Chapter 5 describes the physical properties of $Yb_2O_3 \cdot xH_2O$ obtained by the solvothermal treatment of ytterbium chloride hydrate in various solvents in the presence of amines. The relationship between the morphology of $Yb_2O_3 \cdot xH_2O$ and the effect of the solvents or amines are discussed.

The synthesis of RE borate ($REBO_3$) by the glycothermal method is discussed in chapter 6. The YBO_3 particles obtained by this method were spheroidal with a mean diameter of 1 μm. Selected area electron diffraction analysis indicated that each particle was a "single crystal" of YBO_3 developed from a single nucleus.

Chapter 7 deals with the defective structure of RE aluminium garnet ($RE_3Al_5O_{12}$) obtained by the glycothermal method. It is suggested that Al and oxygen vacancies are present in $RE_3Al_5O_{12}$ synthesized in 1,4-butanediol.

References

[1] G. Adachi, Syokubai, 44 (2002) 29.

[2] G. Adachi, N. Imanaka, Chem. Rev., 98 (1998) 1479.

[3] G. Adachi ed. in Kidorui no Kagaku: Science of Rare Earth, Kagaku Doujin, Kyoto, 1999.

[4] P. K. Sharma, M. H. Jilavi, R. Nass, H. Schmidt, J. Lumin., 82 (1999) 187.

[5] K. M. Minachev, Y. S. Khodakov, V. S. Nakhshunov, J. Catal., 49 (1977) 207.

[6] Y. Fukuda, H. Hattori, K. Tanabe, Bull. Chem. Soc. Jpn., 51 (1978) 3150.

[7] B. H. Davis, Ind. Eng. Chem., Prod. Res. Dev., 21 (1982) 389.

[8] K. Asami, K. Kusakabe, N. Ashi, Y. Ohtsuka, Appl. Catal. A: General, 156 (1997) 43.

[9] G. Tsuboi, M. Haneda, Y. Nagao, Y. Kintaichi, H. Hamada, J. Jpn. Petrol. Inst., 48 (2005) 53.

[10] M. Kobayashi, J. Mater. Chem. Lett., 11 (1992) 767.

[11] G. A. M. Hussein, Powder Technology, 118 (2001) 285.

[12] H. M. Ismail, G. A. M. Hussein, Powder Technology, 87 (1996) 87.

[13] G. A. M. Hussein, Thermochim. Acta, 244 (1994) 139.

[14] J. A. Nelson, M. J. Wagner, Chem. Mater., 14 (2002) 915.

[15] I. W. Lenggoro, Y. Itoh, K. Okuyama, T. O. Kim, J. Mater. Res., 19 (2004) 3534.

[16] J. Dhanaraj, R. Jagannathan, T. R. N. Kutty, C.-H. Lu, J. Phys. Chem. B, 105 (2001) 11098.

[17] R. Bazzi, M. A. Flores-Gonzalez, C. Louis, K. Lebbou, C. Dujardin, A. Brenier, W. Zhang, O. Tillement, E. Bernstein, P. Perriat, J. Lumin., 102–103 (2003) 445.

[18] T. Hirai, Y. Asada, I. Komasawa, J. Colloid Interface Sci., 276 (2005) 339.

[19] L. Yin, Y. Wang, G. Pang, Y. Koltypin, A. Gedanken, J. Colloid Interface Sci., 246 (2002) 78.

[20] S. Polozzi, S. Bucella, A. Speghini, F. Vetrone, R. Naccache, J. C. Boyer, J. A. Capobianco, Chem. Mater., 16 (2004) 1330.

[21] T. Masui, K. Fujiwara, K. Machida, G. Adachi, Chem. Mater., 9 (1997) 2197.

[22] T. Ye, Z. Guiwen, Z. Weiping, X. Shangda, Mater. Res. Bull., 32 (1997) 501.

[23] C. Ho, J. C. Yu, T. Kwong, A. C. Mak, S. Lai, Chem. Mater., 17 (2005) 4514.

[24] G. Wu, L. Zhang, B. Cheng, T. Xie, X. Yuan, J. Am. Chem. Soc., 126 (2004) 5976.

[25] M. Yada, M. Mihara, S. Mouri, M. Kuroki, T. Kijima, Adv. Mater., 14 (2002) 309.

[26] H. Wang, R. Wang, X. Sun, R. Yan, Y. Li, Mater. Res. Bull., 40 (2005) 911.

[27] D. W. Hwang, K. Y. Cha, J. Kim, H. G. Kim, H. G. Kim, S. W. Bae, J. S. Lee, Ind. Eng. Chem. Res., 42 (2003) 1184.

[28] Y. Nishihata, J. Mizuki, T. Akao, H. Tanaka, M. Uenishi, M. Kimura, T. Okamoto, N. Hamada, Nature, 418 (2002) 164.

[29] T. Ishihara, M. Ando, K. Sada, K. Takiishi, K. Yamada, H. Nishiguchi, Y. Takita, J. Catal., 220 (2003) 104.

[30] W.-T. Hsu, W.-H. Wu, C.-H. Lu, Mater. Sci. Eng. B, 104 (2003) 40.

[31] X. Li, H. Liu, J. Wang, X. Zhang, H. Cui, Opt. Mater., 25 (2004) 407.

[32] M. Kakihana, "New Development of Studies on Rare Earth Complexes," ed. by G. Adachi, T. Yamase, J. Inagaki, M. Komiyama, K. Machida, The Ministry of Education, Science, Sports and Culture, Japan(1997), P. 773.

[33] M. K. Cinibulk, J. Am. Ceram. Soc., 83 (2000) 1276.

[34] M. Inoue, "Solvothermal Synthesis," in Chemical Processing of Ceramics, 2nd Ed., Chap. 2, ed. by B. Lee, S. Komarneni, Taylor & Francis, Boca Raton, FL (2005).

[35] S.-J. Chen, X.-T. Chen, Z. Xue, L.-H. Li, X.-Z. You, J. Cryst. Growth, 246 (2002) 169.

[36] G. R. Patzke, F. Krumeich, R. Nesper, Angew. Chem. Int. Ed., 41 (2002) 2446.

[37] S. I. Stupp, P. V. Braun, Science, 277 (1997) 1242.

[38] E. Verdon, M. Devalette, G. Demazeau, Mater. Lett., 25 (1995) 127.

[39] X. Li, H. Liu, J. Wang, H. Cui, F. Han, Mater. Res. Bull., 39 (2004) 1923.

[40] H. Kominami, H. Inoue, S. Konoshi, Y. Kera, J. Am. Ceram. Soc., 85 (2002) 2148.

[41] M. Inoue, Y. Kondo, T. Inui, Chem. Lett., (1986) 1421.

[42] M. Inoue, M. Kimura, T. Inui, Chem. Commun., (1999) 957.

[43] M. Inoue, H. Kominami, H. Otsu, T. Inui, Nippon Kagaku Kaishi (J. Chem. Soc. Japan), (1991) 1364.

[44] M. Inoue, H. Kominami, T. Inui, Appl. Catal. A: General, 97 (1993) L25.

[45] M. Inoue, H. Otsu, H. Kominami, T. Inui, Nippon Kagaku Kaishi (J. Chem. Soc. Japan), (1991) 1036.

[46] M. Takahashi, N. Inoue, T. Takeguchi, S. Iwamoto, M. Inoue, T. Watanabe, J. Am. Ceram. Soc., 89 (2006) 2158.

[47] M. Inoue, "New Development of Studies on Rare Earth Complexes," ed. by G. Adachi, T. Yamase, J. Inagaki, M. Komiyama, K. Machida,, The Ministry of Education, Science, Sports and Culture, Japan(1997), P. 767.

[48] H. Kominami, M. Inoue, T. Inui, Catal. Today, 16 (1993) 309.

[49] M. Inoue, H. Otsu, H. Kominami, T. Inui, J. Alloys Compd., 226 (1995) 146.

[50] M. Inoue, T. Nishikawa, H. Otsu, H. Kominami, T. Inui, J. Am. Ceram. Soc., 81 (1998) 1173.

[51] M. Inoue, T. Nishikawa, T. Nakamura, T. Inui, J. Am. Ceram. Soc., 80 (1997) 2157.

[52] M. Takahashi, N. Inoue, T. Nakatani, T. Takeguchi, S. Iwamoto, T. Watanabe, M. Inoue, Appl. Catal. B: Environmental, 65 (2006) 142.

[53] H. Ozaki, S. Iwamoto, M. Inoue, Chem. Lett., 34 (2005) 1082.

Chapter 1

Solvothermal reaction of rare earth metals in 2-methoxyethanol and 2-aminoethanol

1.1. Introduction

Hydrothermal methods have been widely studied for the synthesis of a variety of minerals and inorganic materials [1-5]. Hydrothermal oxidation of metals has been also examined as a synthesis route for inorganic materials and various compounds having specific properties have been prepared [6-9]. Although it is known that some metals corrode in alcohols, oxidation of metals in alcohols has been scarcely examined from the view point of material synthesis [10-12]. Alcothermal reaction to prepare inorganic materials uses liquid (or supercritical) alcohols as the reaction media at temperatures higher than their boiling points. Inoue et al. examined alcohothermal oxidation of cerium metal and reported that a transparent colloidal solution of ultrafine particles of ceria was directly obtained by the reaction in 2-methoxyethanol at 200-300 °C [13,14]. High-surface-area ceria powder (183 m^2/g) was recovered by coagulation of ceria colloidal particles caused by the addition of an ammonia solution. Because of high surface energy of the product particles, however, the surface area of the ceria powders abruptly decreased by calcination at relatively low temperatures (the sample calcined at 600 °C had a surface area of 2.7 m^2/g with the crystallite size of 21 nm). Addition of a nonionic surfactant to the recovered ceria powder prevented the crystal growth and ceria powder particles maintained a high-surface-area ceria (76 m^2/g) even after calcination at 600 °C [15].

In this chapter, the present author describes solvothermal oxidation of rare earth (RE) metals in various organic solvents, together with the synthesis of RE oxide nanoparticles.

1.2 Experimental

Chips of RE metals were purchased from Wako Pure Chemical Industry and were used without further purification. RE metal (2 g; ca. 3.5 mm×2.0 mm×1.0 mm) and 2-methoxyethanol (80 ml; Nacalai Tesque, Guaranteed Grade) were placed in a test tube, which was then set in an autoclave (200 ml). In the gap between the test tube and the autoclave wall, an additional 40 ml of 2-methoxyethanol was placed. After completely purged with nitrogen, the autoclave was heated to a prescribed temperature (250-315 °C) at the rate 2.5 °C/min and kept at that temperature for a desired period (2 or 8 h) under the autogeneous pressure of the alcohol. After the autoclave was cooled to room temperature, the product was centrifuged at 3500 rpm to remove the coarse particles originating from the superficial layer of the metal chips. To the clear supernatant, a small amount of ammonia was added. The solution became turbid and precipitate was formed. The precipitate was washed with deionized water, dried in air, and calcined at various temperatures for 1 h. Flow chart for the solvothermal oxidation of RE metals is illustrated in Fig. 1-1.

For the reaction systems where the starting RE metal chips were recovered, the reaction in 2-methoxyehanol in the presence of acetic acid was examined. Besides the addition of 5 ml of acetic acid (Wako, GR grade) to 80 ml of 2-methoxyehanol, completely the same procedure was adapted. The solvothermal reaction of RE metals (2 g) in 2-aminoethanol (80 ml; Wako, EP grade) was carried out by using the solvent in place of 2-methoxyethanol of the aforementioned procedure.

X-ray powder diffraction (XRD: Model XD-D1, Shimadzu, Kyoto, Japan) was performed using CuKα radiation and a carbon monochromator. The crystallite size was estimated by the Scherrer equation. The morphology of the colloidal particles was observed with a transmission electron microscope (TEM; Model H-800, Hitachi, Tokyo, Japan) operated at 200 kV. The TEM specimen was prepared by dipping a microgrid in

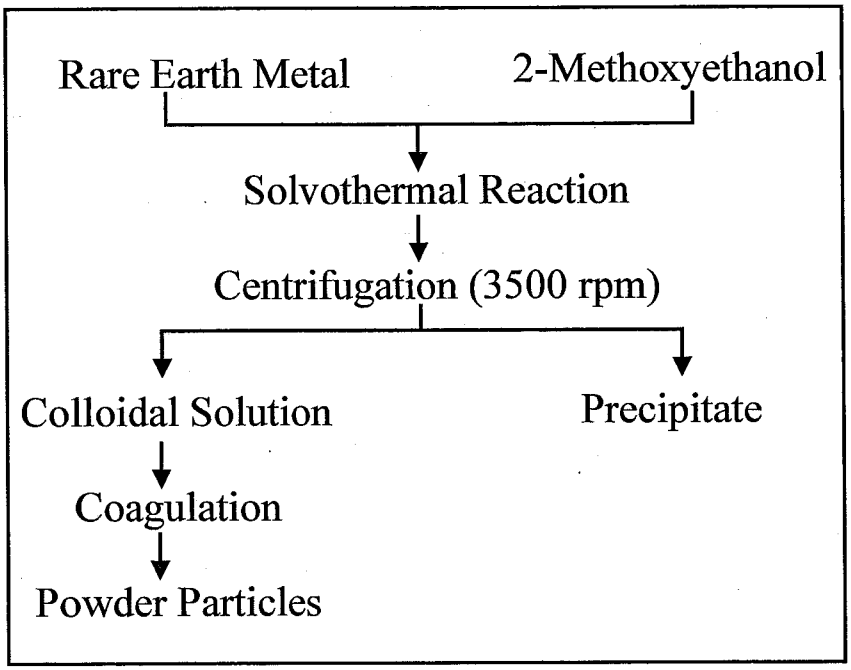

Fig. 1-1. Flow chart of solvothermal oxidation of RE metals.

a diluted colloidal solution (colloidal solution : distilled water = 1 : 100). Simultaneous thermogravimetric and differential thermal analyses were performed on a thermal analyzer (Model DTG-50, Shimadzu, Kyoto, Japan). Raman spectra were recorded (Model, T64000, Jobin-Yvon, Edison, NJ) at room temperature using a 514.5 nm line of argon laser.

1.3 Results and Discussion

1.3.1 Solvothermal reaction of Yb and Sm in 2-methoxyethanol

Figure 1-2 shows the XRD patterns of the RE metal chips. For lanthanum, cerium and praseodymium, metal oxide peaks were clearly detected, indicating that the metal chips of these RE elements were covered with relatively thick superficial layers of metal oxide. For heavy REs, on the other hand, diffraction peaks due to pure metal were found and no other peaks were detected, indicating that the superficial layer is amorphous or quite thin beyond the detection of the crystalline phase by XRD.

The reaction of Yb metal or Sm metal in 2-methoxyethanol proceeded completely. In these reactions, yellow transparent solutions were obtained after the removal of the coarse particles derived from the superficial layer of the metal chips. Addition of a salt solution such as aqueous NaCl to the transparent solutions caused the formation of gelatinous precipitates, indicating that these solutions contained colloidal particles. The TEM image of the Yb_2O_3 colloidal particles is shown in Fig. 1-3. Loosely agglomerated Yb_2O_3 particles with a diameter of ca. 3 nm were observed.

The colloidal particles were coagulated by the addition of aqueous NH_3 to the colloidal solutions. The precipitate was separated by centrifugation and dried in air. The XRD patterns of the products obtained by the reaction of Yb and Sm metals at various reaction temperatures and times are shown in Fig. 1-4. Although the diffraction peaks were quite broad, the XRD profiles coincided with those of Yb_2O_3 and Sm_2O_3. With the

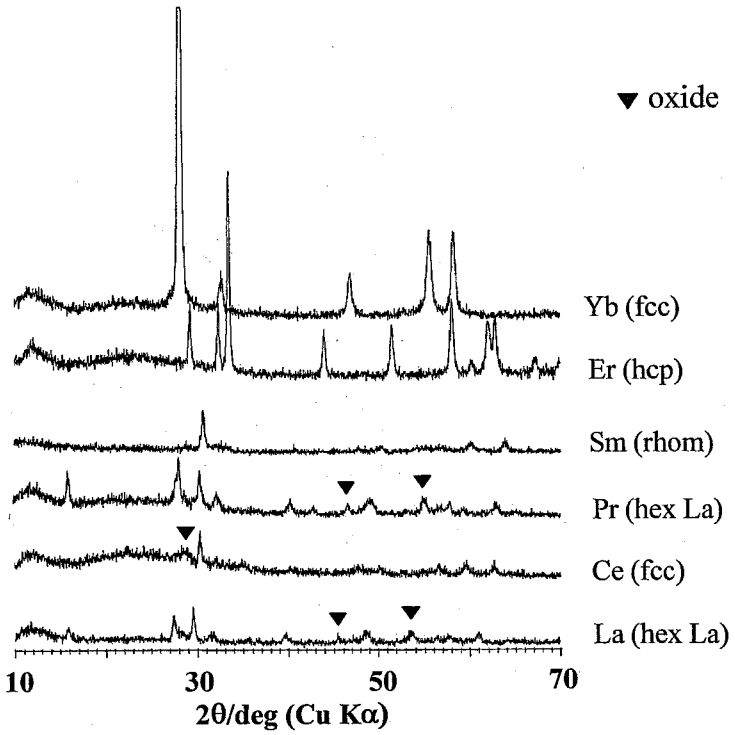

Fig. 1-2. XRD patterns of RE metal chips.

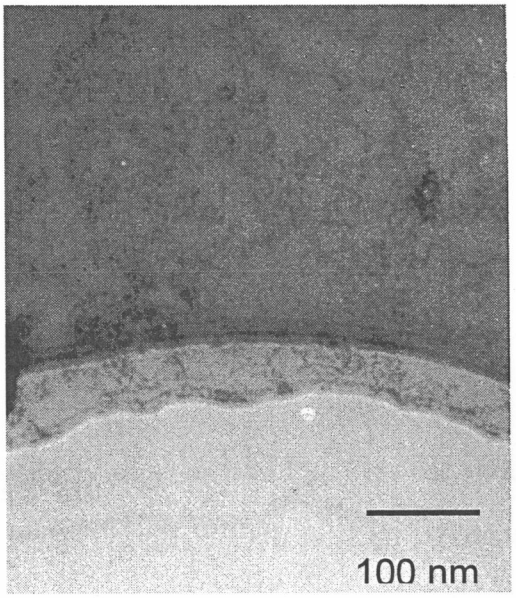

Fig. 1-3. The TEM image of the Yb_2O_3 colloidal particles obtained by solvothermal oxidation of Yb metal at 300 °C for 2 h.

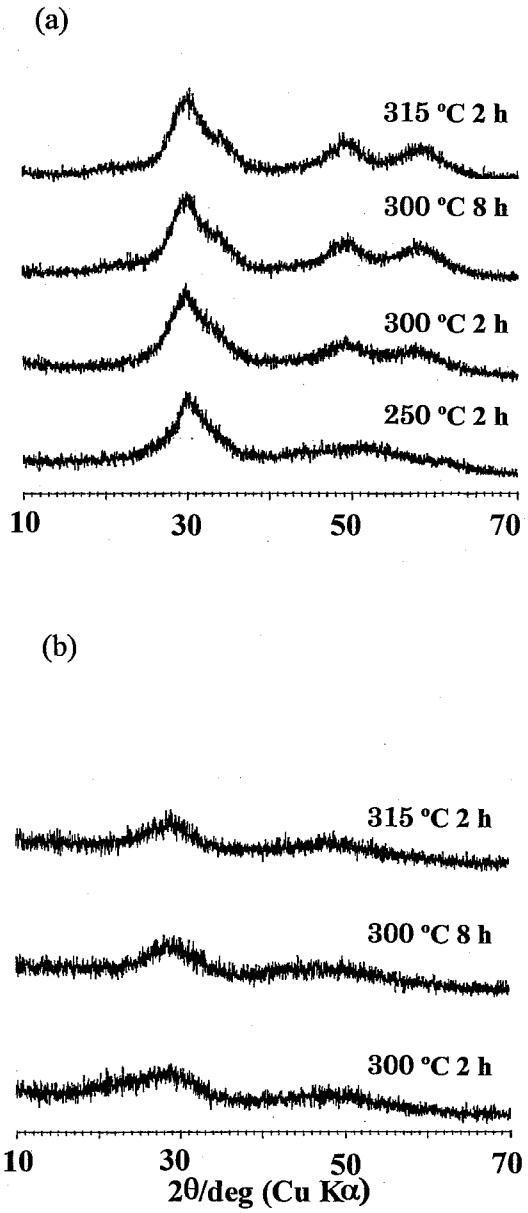

Fig. 1-4. The XRD patterns of the products obtained by the solvothermal oxidation of (a) Yb and (b) Sm at various temperatures for various periods, specified in the figure.

increase in reaction temperature and time, the XRD peaks became sharp, indicating that these particles were crystallized to some extent. From the half-height width of the diffraction peaks, the crystallite size of Yb_2O_3 was estimated to be ca. 3 nm which is in good agreement with the particle size observed by TEM.

When the reaction was carried out at 315 °C for 8 h, growth of the oxide particles occurred and the colloidal solutions were not obtained. The products exhibited the XRD patterns due to the Yb_2O_3 and Sm_2O_3 phases and the XRD peaks were relatively sharp (crystallite size, 24 nm for Yb_2O_3; 37 nm for Sm_2O_3). However, these products seem to contain the coarse particles originating from the superficial layers of the metal chips.

Figure 1-5 shows TG-DTA profiles of the colloidal particles after coagulation and drying. A large weight decrease associated with an exothermic response in DTA is attributed to the combustion of the organic matter remaining on the surface of the product particles.

The IR spectra of the products are shown in Fig. 1-6. The spectra showed bands due to the organic residue at 2980 ($\nu_{as}CH_3$), 2930 ($\nu_{as}CH_2$), 2880 (ν_sCH_2), 1230(t CH_2), 1130(t CH_2), 1100 (νCO), 930 (νCO), and 866 (νCC) cm^{-1} for Sm_2O_3 and 2980, 2940, 2880, 1230, 1140, 1110, and 868 cm^{-1} for Yb_2O_3. Comparison of these spectra with that of liquid 2-methoxyethanol clearly indicates the presence of $CH_3OCH_2CH_2O$- moieties on the surface of the products. The aforementioned assignment for each band is based on the reported data for 2-methoxyethanol [16]. Besides the bands due to the organic moieties, rather strong bands were observed at 1620 and 1460 cm^{-1}. These bands are assigned to carbonate ions, which were formed by adsorption of carbon dioxide during the storage of the products.

If one assumes that 2-methoxyethyl moieties are aligned on 3 nm spherical particles in the closest packing with fully expanded conformation with a molecular radius equivalent to the van der Waals radius of an ethylene group, one can estimate that the

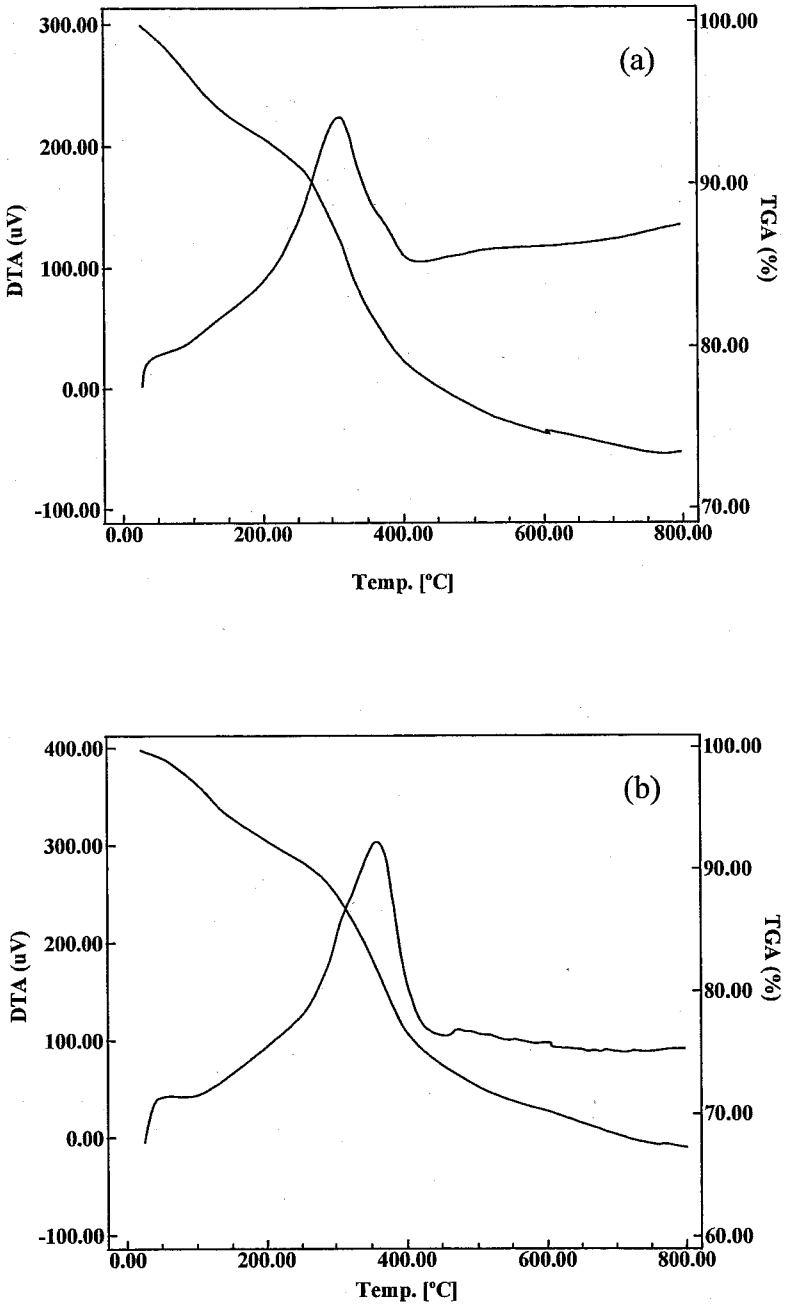

Fig. 1-5. TG-DTA profiles of the powders obtained by coagulation of colloidal particles formed by solvothermal oxidation of (a) Yb and (b) Sm in 2-methoxetanol at 300 °C for 2 h

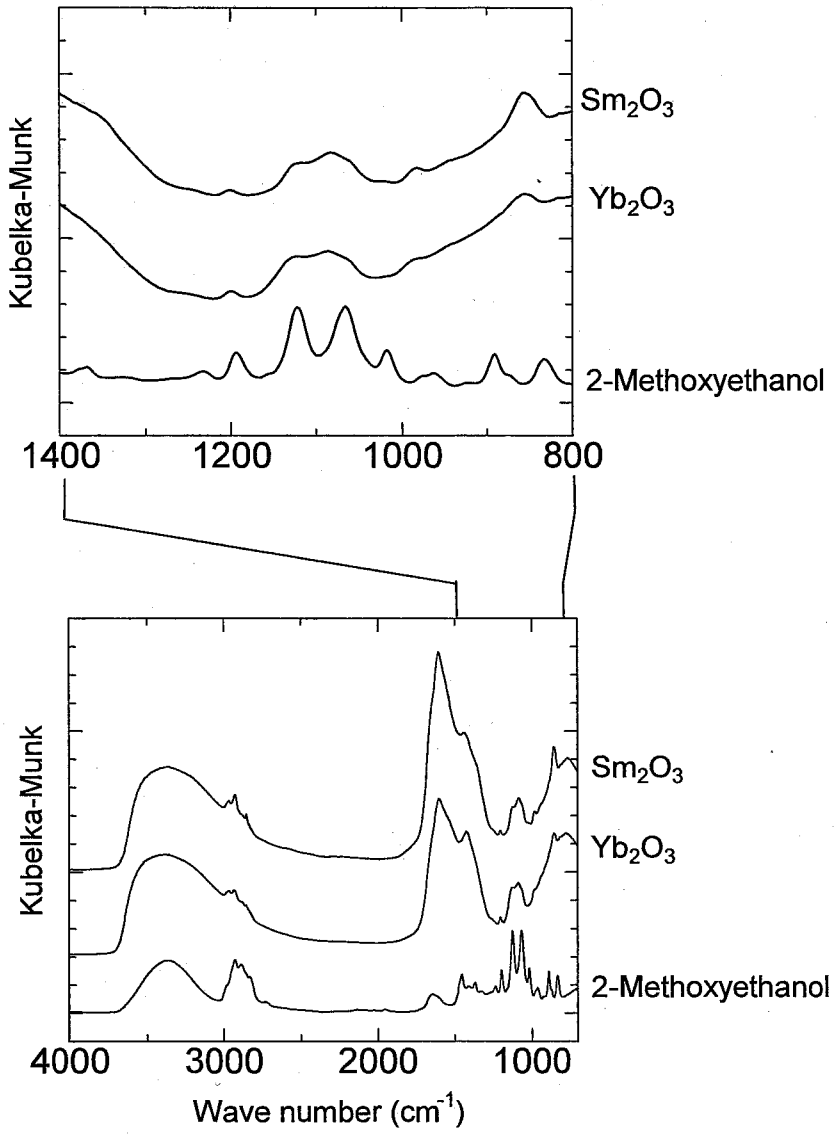

Fig. 1-6. IR spectra of Yb_2O_3 and Sm_2O_3 obtained by coagulation of colloidal particles formed by the reaction of Yb and Sm at 300 °C for 2 h.

weight loss due to desorption of the moieties is ca. 13 %. This value is in good agreement with the observed weight loss at around 350 °C (ca. 15 %).

Figure 1-7 shows the XRD patterns of the thermally treated samples. The XRD peaks due to Yb_2O_3 and Sm_2O_3 suddenly became sharp by heat treatment at 500 °C and 600 °C, respectively. These temperatures are approximately the same as the Tamman temperatures of these oxide phases. These results show a sharp contrast against the sintering behavior of the ceria powders prepared by solvothermal oxidation of cerium metal, where gradual increase in the crystallite size was observed from very low temperatures [13,14]. Nonstoichiometry of cerium oxide seems to contribute to its sintering behavior, since oxidation-reduction cycles cause the cleavage and formation of Ce-O bonds, which facilitates the sintering of ceria particles.

Figure 1-8 shows the Raman spectra of RE oxides obtained by solvothermal oxidation. The ceria particles showed a quite broad peak at 460 cm^{-1}. This result confirmed that ceria powders obtained by solvothermal oxidation of Ce metal were crystallized. Fluorite structure of ceria allows only one Raman T_{2g} mode, which can be viewed as a symmetric breathing mode of the O atoms around cerium cation. Graham et al. reported that Raman spectrum of CeO_2 was systematically changed by the crystallite size [17]. They showed that the Raman linewidth was inversely correlated with the crystallite size of ceria, and they gave the following empirical equation:

$$\Gamma\ (cm^{-1}) = 5.26 + 436 / D\ (Å),$$

where Γ is the half line width at half-maximum and D is the crystallite size of ceria. Other researches also confirmed this relation [18,19]. Lower energy shift of Raman peak with the decrease in the crystallite size was also noted. Although the origin of this change is a controversial issue, Spanier et al. recently concluded that combined effect of the inhomogeneous strain broadening and phonon confinement is the origin of the spectrum change [20]. They also suggested the spectra are also affected by the presence

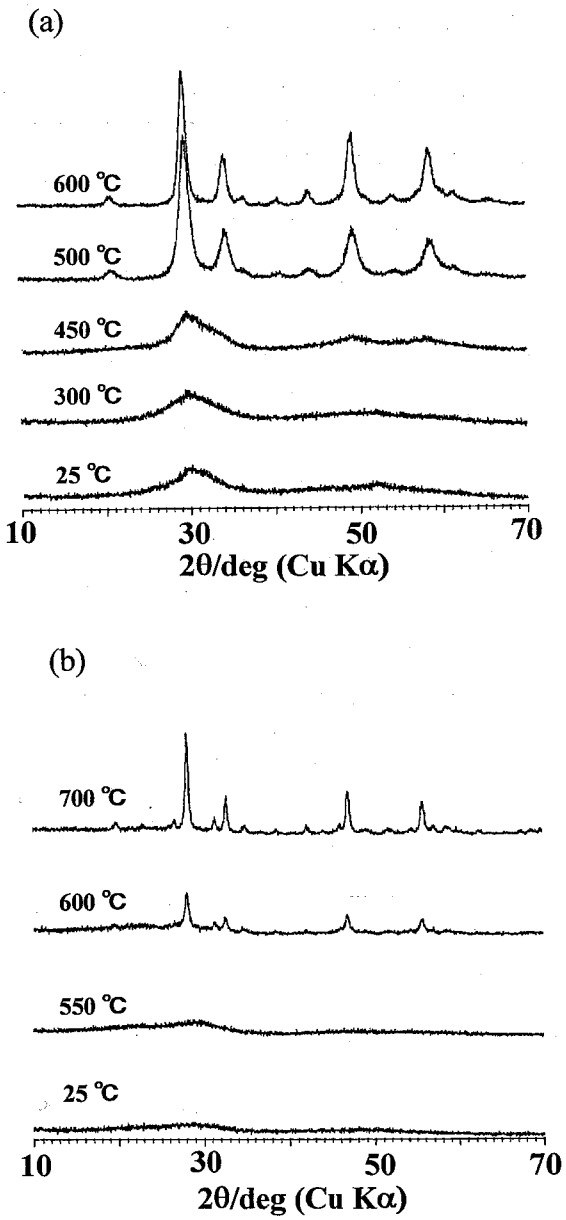

Fig. 1-7. XRD patterns of the powders obtained by coagulation of colloidal particles formed by the reaction of (a) Yb and (b) Sm at 300 ℃ for 2 h, and samples obtained by calcination thereof at various temperature.

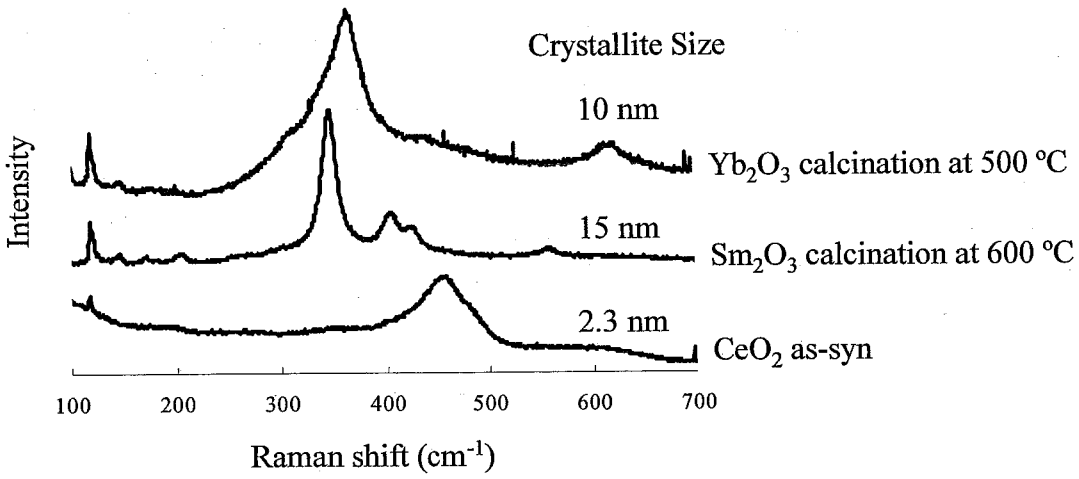

Fig. 1-8. Raman spectra of RE oxides obtained by solvothermal oxidation at 300 °C for 2 h.

of oxygen vacancies [20]. Although the crystallite size (2.3 nm) of the ceria particles obtained by solvothermal oxidation of cerium metal was much smaller than the crystallite-size range used for determination of the empirical equation [17], the observed linewidth (48 cm^{-1}; Γ = 24cm^{-1}) is in good agreement with that predicted by the equation (Γ = 23.8 cm^{-1}). The observed Raman frequency (460 cm^{-1}) is much lower than that for well-crystallized ceria (467 cm^{-1}) [17]. However, the low energy shift of the Raman frequency of the present product is also within the expectation from the reported correlation between linewidth and frequency [17]. On the other hand, the present author could not obtain Raman peaks for the as-synthesized Sm_2O_3 and Yb_2O_3 particles. One reason is fluorescence due to the organic moieties remaining on the surface of the products, but line broadening beyond the detection of Raman peaks caused by the small crystallite size is also likely to contribute to the absence of Raman peaks. After heat treatment, Raman peaks for type C oxides were detected [21-23]. Note that the Yb_2O_3 sample exhibited quite broad Raman peaks in spite of the fact that the sample was calcined at 500 °C, which caused a significant increase in the crystallite size.

The results of solvothermal oxidation of RE metals in 2-methoxyethanol at 300 °C are summarized in Table 1-1. The reaction of La, Pr, and Nd metals proceeded completely. However, after the removal of coarse particles by centrifugation, colloidal solutions were not obtained: Addition of a salt solution to the supernatants caused no apparent change in the supernatants. It is interesting to note that the reactivity of the RE metal in 2-methoxyethanol may depend on the crystal structure of the metal. Hexagonal La type metals (La, Pr and Nd) reacted easily yielding coarse products, and RE metals with the fcc structure (Ce and Yb) and rhombohedral crystal symmetry (Sm) reacted in 2-methoxethanol yielding colloidal solutions, while the RE metals having hexagonal crystal symmetry were inert in 2-methoxyethanol.

Table 1-1 Solvothrmal oxidation of RE metals in 2-methoxyethanol at 300 °C for 2 h.

Metal	Crystal structure of metal	Reaction[1]	Colloidal solution[2]	Product phase
Y	hcp	×	×	—
La	hex La	○	×	$La_2O_2CO_3$, $La(OH)_3$
Ce	fcc	○	○	CeO_2
Pr	hex La	○	×	$Pr_2O_2CO_3$, PrOOH
Nd	hex La	○	×	$Nd_2O_2CO_3$, $Nd(OH)_3$
Sm	rhom	○	○	Sm_2O_3
Eu	bcc	×	×	—
Gd	hcp	×	×	—
Tb	hcp	×	×	—
Dy	hcp	×	×	—
Ho	hcp	×	×	—
Er	hcp	×	×	—
Tm	hcp	×	×	—
Yb	fcc	○	○	Yb_2O_3

hcp, hexagonal close packed; hex, hexagonal; fcc, face-centered cubic; rhom, rhombohedral; bcc, body-centered cubic. 1○, reaction yielded product(s) specified in the last column; ×, reaction resulted in recover of the starting material. 2○, formation of colloidal solution; ×, product was obtained as precipitate.

1.3.2 Solvothermal reaction of RE metals in 2-methoxyethanol in the presence of acetic acid

Since the recovery of the starting metal chips means low solubility of the superficial layers into 2-methoxyethanol, reaction in the presence of a small amount of acetic acid was examined. The results are summarized in Table 1-2. As described in the previous section, colloidal solutions of CeO_2, Sm_2O_3, and Yb_2O_3 were obtained without the addition of acetic acid, while the other metals, such as Y, Eu, Gd, and Tb, did not afford colloidal solutions. However, colloidal solutions were obtained by the reaction of these metals in the presence of acetic acid. In Fig 1-9, a picture of the colloidal solution obtained by the reaction of Eu metal in 2-methoxyethanol together with a small amount of acetic acid is shown. Tyndall phenomenon was clearly observed. Figure 1-10 shows the XRD patterns and TG-DTA profiles of the powders obtained by coagulation of the colloidal particles. The particles are only poorly crystallized. An exothermic response at around 650 °C in DTA can be attributed to the crystallization of Eu_2O_3 from $Eu_2(CO_3)O_2$. The carbonate ions were formed by combustion of the organic moieties remaining on the product particles. Besides formation of Eu_2O_3 and Tb_2O_3, Gd and Y metals yielded transparent colloidal solutions. Calcination of the powders obtained by coagulation of the colloidal particles gave GdOOH and a mixture of Y_2O_3 and YOOH. Phases formed by calcination are summarized in Table 1-3.

By the addition of acetic acid to the solvothermal reaction systems, colloidal particles were obtained from the RE metal chips having superficial layers. These results indicate that acetic acid dissolves the superficial layers of RE metal chips and then facilitates the reaction of RE metal with 2-methoxyethanol (and/or acetic acid).

It must be noted that the reaction of Ce metal in a mixture of 2-methoxyethanol and acetic acid did not yield the colloidal solution of ceria but coarse ceria particles were sedimented by centrifugation. In previous work [13,14], Inoue et al. examined

Table 1-2 Solvothermal oxidation of RE metals in 2-methoxyethanol (80 ml) and acetic acid (5 ml) or in 2-aminoethanol at 300 °C for 2 h.

Medium	Metal	Reaction	Colloidal solution	Product phase
2-Methoxyethanol and Acetic Acid	Y	○	○	YOOH
	Eu	○	○	Eu_2O_3, $Eu_2(CO_3)O_2$
	Gd	○	○	GdOOH
	Tb	○	○	Tb_2O_3
2-Aminoethanol	Y	○	—	YOOH
	La	○	—	$La(OH)_3$
	Ce	○	○	CeO_2
	Pr	○	—	PrOOH, Pr_2O_3
	Nd	○	—	NdOOH, Nd_2O_3
	Sm	○	○	SmOOH, Sm_2O_3
	Eu	○	—	EuOOH
	Gd	×	—	—
	Er	×	—	—
	Yb	○	○	Yb_2O_3

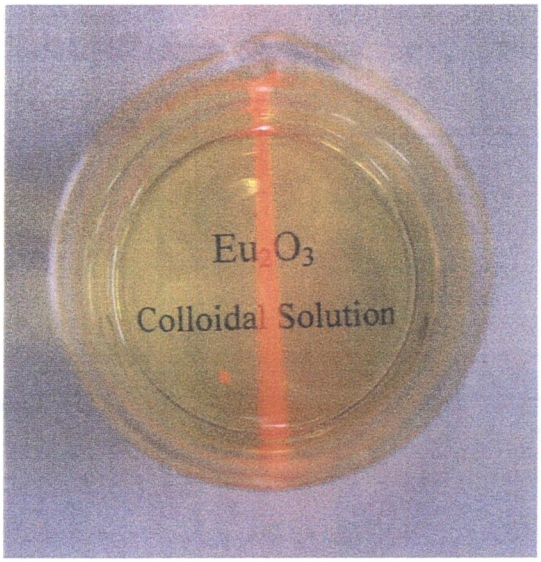

Fig. 1-9. Transparent colloidal solution of Eu_2O_3 obtained by the reaction of Eu metal in 2-methoxyethanol and acetic acid at 300 °C for 2 h.

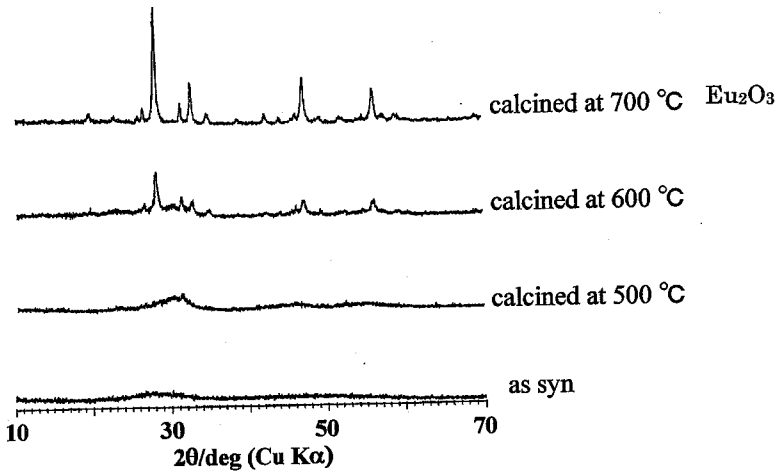

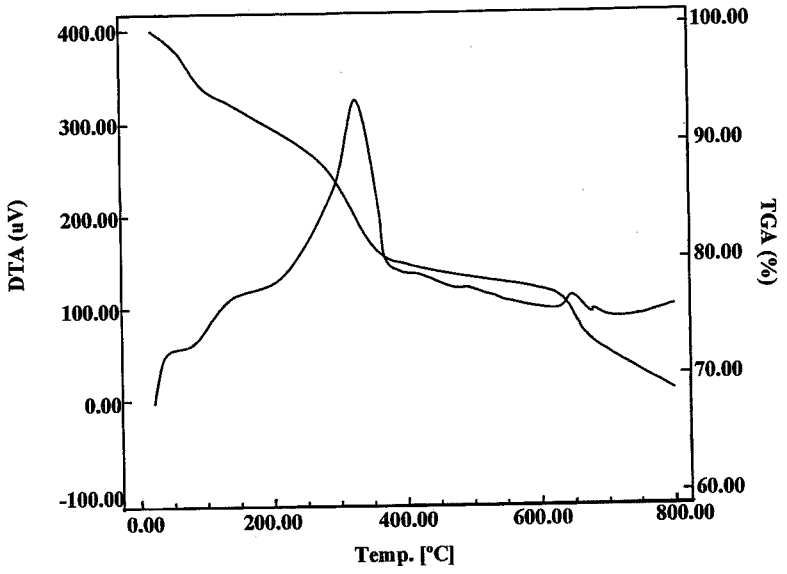

Fig. 1-10. XRD patterns and TG-DTA profiles of products obtained by reaction of Eu metal in 2-methoxyethanol and acetic acid at 300 °C for 2 h.

Table 1-3 Phase formed by calcination of coagulated particles formed by solvothermal oxidation of RE metals.

Medium	Metal	as-syn.	500 °C	600 °C	700 °C	800 °C
2-Methoxyethanol and Acetic Acid	Eu	broad peaks	broad peaks	Eu_2O_3, $Eu(CO_3)_2$	Eu_2O_3	-
	Tb	broad peaks	broad peaks (Tb_2O_3)	Tb_2O_3	Tb_2O_3	-
	Y	broad peaks	broad peaks (Y2O3, YOOH)	Y_2O_3, YOOH	Y_2O_3	-
	Gd	broad peaks	broad peaks	GdOOH	Gd_2O_3, GdOOH	Gd_2O_3 (1000 °C)
2-Aminoethanol	Sm	Sm_2O_3, SmOOH	Sm_2O_3	-	-	Sm_2O_3
	Yb	Yb_2O_3	Yb_2O_3	-	-	-
	Ce	CeO_2	CeO_2	-	-	-

the reaction of cerium acetylacetonate in 2-methoxyethanol and found coarse ceria particles were formed. Therefore, the present author concluded that the presence of the superficial layers is essential for the formation of the ceria colloidal solution. Dissolution of the superficial layers at high temperatures causes very rapid reaction of cerium metal with the solvent alcohol yielding cerium alkoxide and hydrogen. High concentration of the alkoxide causes bust nucleation of ceria resulting in formation of the colloidal particles. The present result supports this mechanism, since the dissolution of the superficial layer at lower temperatures will give a solution of the alkoxide, which gradually decomposes yielding a limited number of ceria nuclei. Crystal growth takes place lowering the alkoxide concentration and finally yielding coarse ceria particles.

1.3.3 Solvothermal reaction of RE metals in 2-aminoethanol

The XRD patterns of the products obtained by the solvothermal reaction of RE metal chips in 2-aminoethanol are shown in Fig. 1-11. From Ce, Sm, and Yb metals, turbid colloidal solutions were obtained after the removal of the coarse particles. The XRD pattern of the powder recovered by coagulation of the colloidal particles by the addition of an NH_3 solution showed the formation of CeO_2, a mixture of Sm_2O_3 and SmOOH, and Yb_2O_3.

The TG-DTA profiles of the powders, which were recovered from the colloidal solution obtained by solvothermal reaction of Sm metal in 2-aminoethanol, are shown in Fig. 1-12. The DTA curve exhibited endothermic peaks. These peaks were due to the decomposition of SmOOH and desorption of the organic moieties remaining on the product particles. The former process yielded Sm_2O_3 and the XRD pattern of the sample calcined at 500 °C showed the peaks due to Sm_2O_3. The latter process occurred since the presence of the nitrogen atom in the organic moieties makes them difficult to combust.

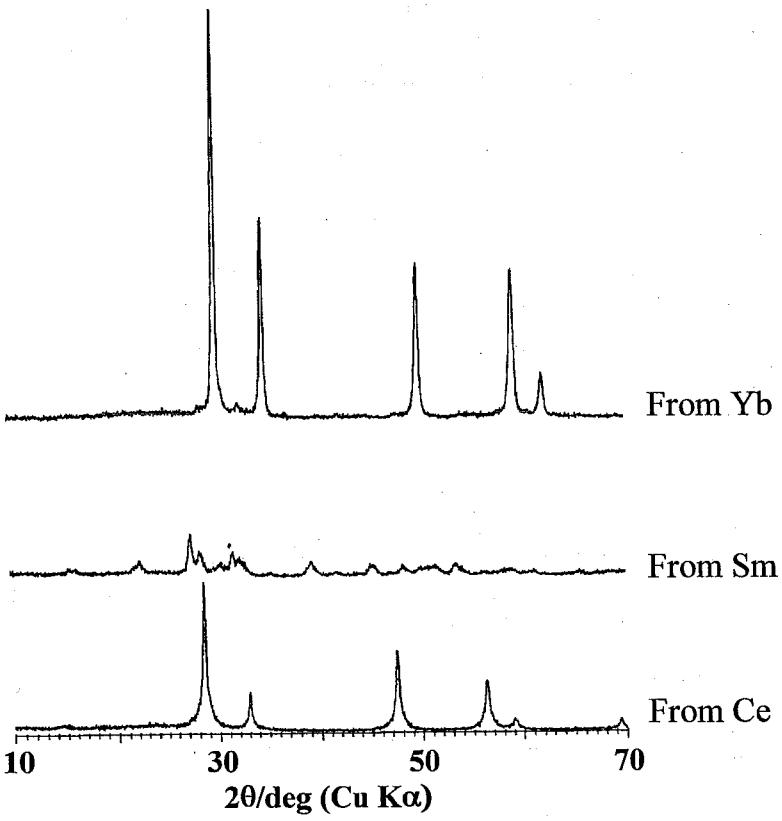

Fig. 1-11. XRD patterns of products obtained by solvothermal reaction of RE metals in 2-aminoethanol. at 300 °C for 2 h.

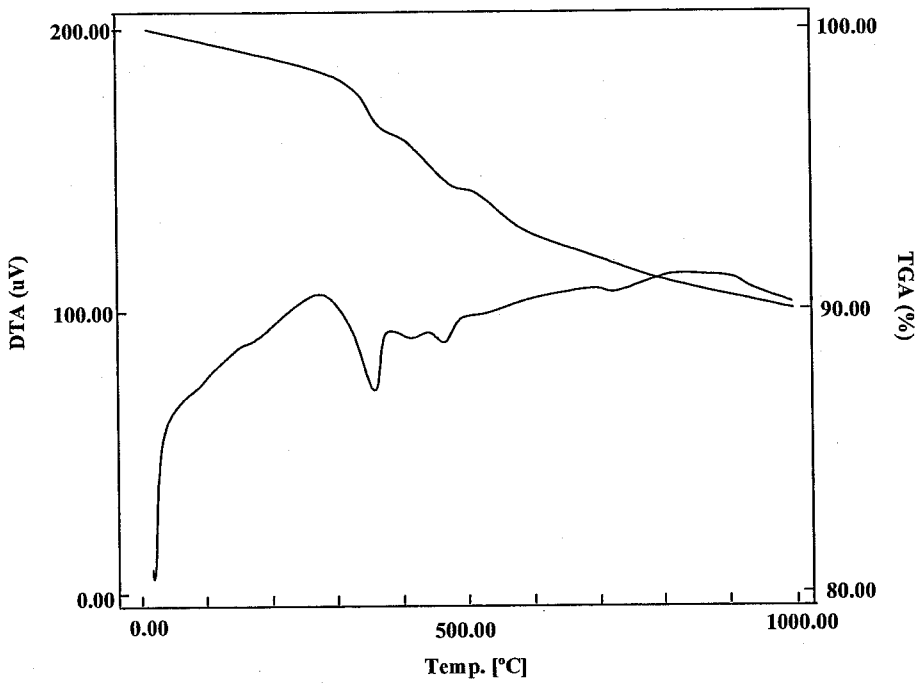

Fig. 1-12. TG-DTA profiles of powders obtained by solvothermal oxidation of Sm metal in 2-aminoethanol at 300 °C for 2 h.

The results for solvothermal reaction of RE metals in 2-aminoethanol are summarized in Table 1-2. Besides Ce, Sm and Yb metals, which gave the colloidal solutions albeit turbid, Y, La, Pr, Nd and Eu reacted in 2-aminoethanol yielding YOOH, $La(OH)_3$, mixture of PrOOH and Pr_2O_3, mixture of NdOOH and Nd_2O_3, and EuOOH. However, colloidal solutions were not obtained from these metals. The phases formed by calcination of the samples obtained by coagulation of the colloidal particles formed by reaction of Ce, Sm and Yb are summarized in Table 1-3.

As compared with the reaction in 2-methoxyethanol, oxides or hydroxide oxides of RE elements were obtained from a wide range of RE metals, and the reaction took place easily. In 2-aminoethanol, the products are fairly well crystallized. These results seem to be due to higher polarity of 2-aminoethanol (ε = 37.72) as compared with 2-methoxyethanol (ε = 16.93).

1.3.4 Proposed reaction mechanisms

RE metals are highly active and they are flammable when fresh surfaces are exposed to moist air. However, in the present experiments, metal chips with superficial layers were used, and therefore safe experiments were carried out. The reaction of RE metal with water proceeds according to the following equation:

$$2RE + 6H_2O \rightarrow 2RE(OH)_3 + 3H_2.$$

Similarly, the reaction of RE metal with alcohol proceeds easily:

$$2RE + 6ROH \rightarrow 2RE(OR)_3 + 3H_2.$$

However, the superficial layer must be dissolved or broken before the reaction takes place, and addition of acetic acid or use of 2-aminoethanol having higher polarity than 2-methoxyethanol facilitated the dissolution of the superficial layers. The thermal decomposition of RE alkoxide yields RE oxide according to the following reaction:

$$2RE(OR)_3 \rightarrow RE_2O_3 + 3ROR$$

Importance of the superficial layers of metal chips was discussed in section (1.3.2).

1.4 Conclusions

1. Transparent colloidal solutions of Sm_2O_3 and Yb_2O_3 were obtained by solvothermal oxidation of Sm and Yb metals in 2-methoxyethanol at 300 °C for 2 h.

2. Transparent colloidal solutions of Y, Eu, Gd and Tb species were obtained by solvothermal oxidation of the corresponding metals in 2-methoxyethanol in the presence of a small amount of acetic acid. The dissolution of the superficial layers of RE metal chips was facilitated by the presence of acetic acid.

3. The reaction of Ce, Sm and Yb metals in 2-aminoethanol yielded turbid colloidal solutions of the oxides. In addition, the reaction of some other RE metals afforded the precipitates of the corresponding oxides or hydroxide oxides, and the reaction took place easily because of high polarity of 2-aminoethanol.

References

[1] G. W. Morey, J. Am. Ceram. Soc., 36 (1953) 279.

[2] R. A. Laudise, "Hydrothermal Growth: The Growth of Single Crystals," Prentice Hall, Englewood Cliffs, NJ, 275 (1970).

[3] S. Somiya, "Advanced Materials: Frontiers in Materials Science and Engineering," vol. 19B, Elsevier Science, Amsterdam, 1105 (1993).

[4] W. J. Dawson, Am. Ceram. Soc. Bull., 67 (1988) 1673.

[5] S. Somiya, R. Roy, S. Komarneni, "Hydrothermal Synthesis of Ceramic Powders," in Chemical Processing of Ceramics, 2nd Ed., Chap. 1, Ed. by B. Lee and S. Komarneni, Taylor & Francis, Boca Raton. FL. (2005).

[6] K. Torkar, H. Worel, H. Krischner, Monatsh. Chem., 91 (1960) 653.

[7] K. Torkar, H. Krischner, Monatsh. Chem., 91 (1960) 658.

[8] M. Yoshimura, S. Somiya, Am. Ceram. Soc., Bull., 59 (1980) 246.

[9] H. Toraya, M. Yoshimura, S. Somiya, J. Am. Ceram. Soc., 65 (1982) C-72.

[10] M. Inoue, M. Kimura, T. Inui, Adv. Sci. Tech., 16 (1999) 593.

[11] M. Inoue, M. Kimura, T. Inui, Chem. Matter., 12 (2000) 55.

[12] S.-J. Chen, L.-H. Li, X.-T. Chen, Z. Xue, J.-M. Hong, X.-Z. You, J. Cryst. Growth, 252 (2004) 184.

[13] M. Inoue, M. Kimura, T. Inui, "Transparent Colloidal Solution of 2 nm Ceria Particles," Chem. Commun., 957-58 (1999).

[14] M. Inoue, M. Kimura, T. Inui, Ceram. Trans., 108 (2000) 53.

[15] T. Kobayashi, S. Iwamoto, M. Inoue, J. Alloys Compd., 408-412 (2006) 1149.

[16] F. P. S. C. Gil, R. Fausto, A. M. A. da Costa, J. J. C. Teixeira-Dias, J. Chem. Soc., Faraday Trans., 90 (1994) 689.

[17] G. W. Graham, W. H. Weber, C. R. Peters, R. Usmen, J. Catal., 130 (1991) 310.

[18] W. H. Werber, K. C. Hass, J. R. McBride, Phys. Rev. B, 48 (1993) 178.

[19] Z. C. Orel, Appl. Spectro., 53 (1999) 241.

[20] J. E. Spanier, R.D. Robinson, F. Zhang, S.-W. Chan, I. P. Herman, Phys. Rev., 64 (2001) 245407-1-8.

[21] W. B. White, V. G. Keramidas, Spectrochim. Acta, 28A (1972) 501.

[22] J.-F. Martel, S. Jandl, A. M. Lejus, B. Viana, D. Vivien, J. Alloys. Compd., 275-277 (1998) 353.

[23] J. B. Gruber, R. D. Chirico, E. F. Westrum, Jr., J. Chem. Phys., 76 (1982) 4600-05.

Chapter 2

Synthesis of nanocrystalline rare earth oxides by glycothermal method

2.1. Introduction

Many methods have been reported for the synthesis of RE oxide nanoparticles, as stated in General Introduction section. They include oxidation of metal [1,2] or metal hydride [3] nanoparticles, vaporization/condensation of ceramics [4-6], chemical vapor deposition [7], thermal decomposition [8,9], spray pyrolysis [10], combustion synthesis [11-13], high energy mechanical milling [14], polyol process [15-17], reverse micellar synthesis [18,19], sonochemical synthesis [20], hydrothermal synthesis [21], and so on. However, most of these methods give RE oxide particles with crystallite sizes larger than 10 nm, and only a few methods are available for the synthesis of RE oxide nanoparticles with the crystallite size less than 10 nm.

The $Y_2O_3:Eu^{3+}$ phosphor nanoparticles were obtained by a reverse micelle method (4-8 nm) [18] or by a glycine-nitrate combustion method (~8 nm) [12]. Monodispersed RE oxide particles with an average diameter in range 2-5 nm were prepared by direct precipitation from a diethylene glycol solution [15]. So far as the present author knows, the smallest RE oxide particle ever was attained that reported by Nelson et al.; they prepared Y_2O_3 nanoparticles by homogeneous reduction of YCl_3 with $K^+(15\text{-crown-}5)_2Cl^-$ and subsequent oxidation [1,2]. The as-synthesized product is amorphous (particle size: 1-3 nm), and the sample crystallized by annealing at 500 °C for 4 h has a surface area of 84 m^2/g and a crystallite size of 11.8 nm.

The reaction of RE acetate hydrates in 1,4-butanediol yields $RE(OAc)_2(OH)$, $RE(OAc)(OH)_2$ or RE(OAc)O depending on the ionic size of the RE elements [22]. However, the reaction of RE acetate hydrates in ethylene glycol yields

$RE_2O(OCH_2CH_2O)(OAc)_2$ or $RE_2O(OCH_2CH_2OH)_2(OAc)(OH)$ containing glycol moieties depending on the ionic size of the RE element [23]. This difference in reaction behaviour is attributed to the high coordinating ability of the vicinal glycol as compared with 1,4-buntanediol. The products obtained in 1,4-bunanediol decompose to RE oxides at around 700 °C via RE carbonate oxide phase ($RE_2O_2CO_3$), while the products obtained in ethylene glycol directly decompose to RE oxide at around 400 °C without the formation of RE carbonate oxide.

Chapter 1 addressed RE oxide nanoparticles obtained by the solvothermal oxidation of RE metals in 2-methoxyethanol. This chapter discussed the RE oxide nanoparticles obtained by the glycothermal treatment of RE acetate hydrate in vicinal glycols (ethylene glycol, 1,2-propanediol or 1,2-butanediol) and subsequent calcination at low temperature.

2.2. Experimental

2.2.1 Glycothermal treatment of yttrium acetate hydrate

Ethylene glycol (EG), 1,2-propanediol (1,2-PG), 1,2-butanediol (1,2-BG), 1,3-propanediol (1,3-PG) and 1,4-butanediol (1,4-BG) were used as solvents. Yttrium acetate hydrate ($Y(OAc)_3 \cdot 4H_2O$) (8.453 g, 25 mmol) was suspended in 120 ml of solvent in a test tube serving as an autoclave liner. The test tube was placed in a 300-ml autoclave. An additional 40 ml of the solvent was placed in the gap between the autoclave wall and test tube. The autoclave was completely purged with nitrogen, heated to 300 °C at a rate of 2.3 °C/min and maintained at the same temperature for 2 h. After the assembly was rapidly cooled to room temperature, the resulting product was collected by centrifugation. The product was washed with methanol by vigorous mixing and centrifuging and then air-dried. For calcination, the products were heated in a box furnace at a rate of 10 °C/min and maintained at the prescribed temperature for 30 min.

The amount of product obtained in 1,2-PG was about 5.5 g, and the ceramic yield of the product as calculated from the weight loss after calcination at 1000 °C exceeded 90%.

These products are labelled as P(abbreviation of the solvent); in the case of calcination, the applied temperature (in Celsius) is added to the above label. For example, P(1,4-BG)400 refers to the product obtained by the reaction in 1,4-BG followed by calcination at 400 °C.

2.2.2 Characterization

Since RE oxides react with H_2O and/or CO_2 in air at room temperature producing hydroxides and/or carbonate hydroxides [24], the characterization of calcined samples was carried out within 24 h after calcination.

The organic species derived by the thermal decomposition of the products were analysed as follows: The product was calcined in O_2 (50 Torr) at 400 °C using a closed circulation system (total dead volume: 150 cm^3), and the generated gases were trapped with liquid nitrogen. These gases were analysed using gas chromatographs equipped with FID (Porapak Q column, 2 m, 180 °C) and TCD (Porapak N column, 2 m, 50 °C) detectors and by mass spectrometry (SX102, JEOL, Tokyo, Japan).

The X-ray powder diffraction patterns (XRD: XD-D1, Shimadzu, Kyoto, Japan) were recorded using Cu $K\alpha$ radiation and a carbon monochromator. The crystallite sizes of RE oxides were calculated from the full width at half maximum (FWHM) of the 222 diffraction peak using Scherrer's equation:

$$D\ (\mathrm{nm}) = \frac{0.9 \times 0.1542}{\beta \times \cos\theta}$$

where D is the crystallite size; θ, the diffraction angle; and $\beta = \beta_{exp} - \beta_{app}$. Here, β_{exp} and β_{app} are the FWHM of the diffraction peak and the instrumental broadening width, respectively.

The diffuse reflectance FT-IR spectra of the products were recorded in the range of 4000–700 cm^{-1} using a Nicolet spectrophotometer (Magna-IR 560, Madison, USA) with KBr as the background. Simultaneous thermogravimetric and differential thermal analyses (TG-DTA) were performed using a thermal analyser (DTG-50, Shimadzu, Kyoto, Japan) at a rate of 5 °C/min in a 40 ml/min flow of dried air. The specific surface area was calculated by BET single-point method on the basis of the N_2 uptake measured at 77 K using a sorptionmeter (Flowsorb II 2300, Micromeritics). The morphology of the product was observed using a transmission electron microscope (TEM, Hitachi H-800) operated at 200 kV.

2.3. Results and Discussion

2.3.1 XRD analysis and IR spectroscopy

The XRD patterns of the products obtained from the reaction at 300 °C are shown in Fig. 2-1. The XRD patterns of P(1,3-PG) and P(1,4-BG) are attributed to Y(OAc)O [22], while that of P(EG) is attributed to $Y_2O(OCH_2CH_2OH)_2(OAc)(OH)$ [23]. The XRD patterns of P(1,2-PG) and P(1,2-BG) differ distinctly from that of Y(OAc)O or $Y_2O(OCH_2CH_2OH)_2(OAc)(OH)$.

The IR spectra of the products are shown in Figs. 2-2a and 2b. In addition to the relatively weak stretching vibration modes attributed to CH_3 of the acetate group, P(1,2-PG) and P(1,2-BG) exhibit strong stretching vibration modes at 2700–3000 cm^{-1} due to the CH_3 and CH_2 groups. However, P(EG) exhibits only the stretching vibration modes of the CH_2 groups. In contrast, the product obtained in 1,4-BG does not exhibit the stretching vibration modes due to the CH_2 groups originating from the solvent. In addition, due to the acetate groups, all spectra exhibit the stretching vibration bands at around 1610 and 1480 cm^{-1}. The spectrum of P(1,4-BG) is fairly similar to that of yttrium acetate hydrate at 1084, 1053 and 955 cm^{-1}, and the peaks due to the 1,4-BG

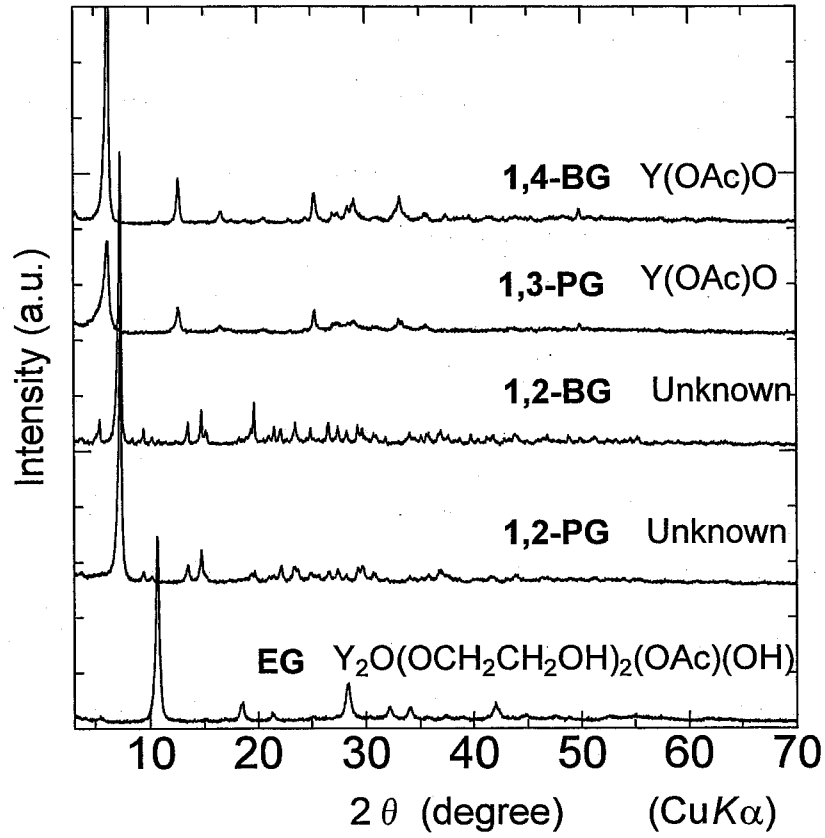

Fig. 2-1. XRD patterns of the products obtained by the reaction of yttrium acetate hydrate in various glycols at 300 °C for 2 h.

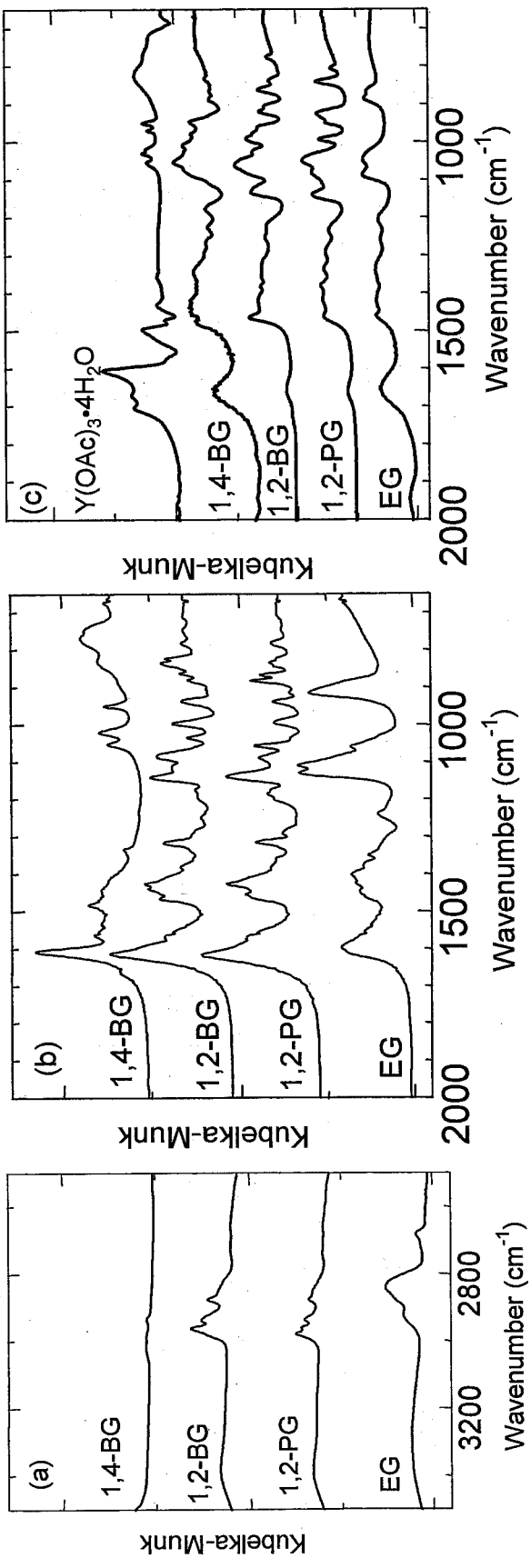

Fig. 2-2. IR spectra of (a and b) the products obtained by the reaction of yttrium acetate hydrate in various glycols at 300 °C for 2 h and (c) standard samples of the glycols together with yttrium acetate hydrate.

moiety are not observed. This spectral feature coincides with the proposed empirical formula (Y(OAc)O) of P(1,4-BG) [22]. At the region from 800 to 1300 cm^{-1}, however, the spectra of the other products exhibit several peaks and are similar to those of the corresponding solvents shown in Fig. 2-2c. However, the peak positions are slightly different, presumably because of the strong coordination of the glycol moieties to yttrium ion. These results indicate that the products obtained in 1,2-PG, 1,2-BG and EG contain both the glycol moieties and acetate ligands.

2.3.2 Analysis of thermal decomposition

The TG-DTA profiles of the products obtained in EG, 1,2-PG, 1,2-BG and 1,4-BG are shown in Fig. 2-3. For P(1,4-BG), the weight loss at 350–400 °C is attributed to the decomposition of Y(OAc)O to $Y_2O_2CO_3$, while the weight loss at ~700 °C is attributed to the decomposition of $Y_2O_2CO_3$ to Y_2O_3 [22]. The thermal decomposition behaviour of P(1,2-PG) is similar to that of P(1,2-BG), and significant weight loss associated with an exothermic peak is detected at 360 °C. On the other hand, in the case of P(EG), weight loss associated with an exothermic peak is observed at 340 °C; weight loss is also detected at 600 °C. The total weight loss cause by calcination at 800 °C increases with the carbon number of glycol—EG < 1,2-PG < 1,2-BG. This result also supports the argument that the product contains the glycol moieties originating from the solvent.

The XRD patterns of the products treated at 400 °C, together with the BET surface areas of the samples, are shown in Fig. 2-4. Y(OAc)O decomposes to $Y_2(CO_3)O_2$, but the products obtained in vicinal glycols decompose directly to Y_2O_3 (JCPDS card No. 41-1105) without the formation of the carbonate oxide phase. The crystallite sizes of these Y_2O_3 samples are less than 3 nm.

The organic species formed by the thermal decomposition of these products were analysed using a closed circulation system. For Y(OAc)O obtained in 1,4-BG, large

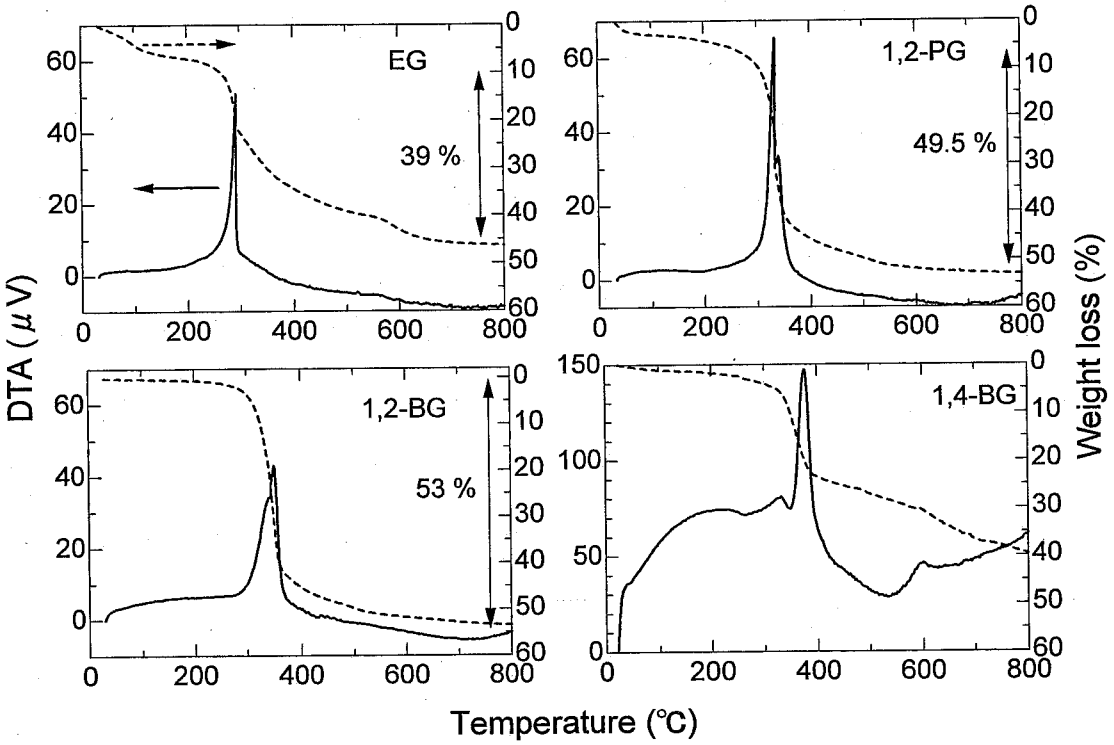

Fig. 2-3. TG-DTA profiles of the products obtained by the reaction of yttrium acetate hydrate in various solvents at 300 °C for 2 h.

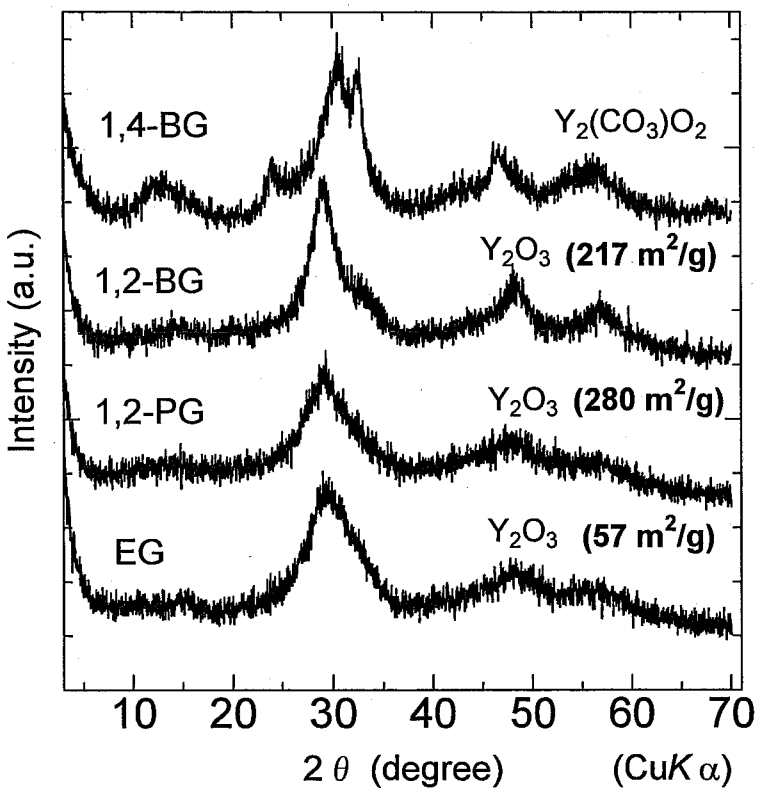

Fig. 2-4. XRD patterns of the samples obtained by calcination of the products at 400 °C for 30 min. Surface area the samples calculated using BET single-point method is given in the parenthesis.

amounts of acetone and CO_2 are generated with traces of various volatile low-boiling-point compounds. For P(EG) and P(1,2-PG), however, high-boiling-point products are generated in addition to those originating from Y(OAc)O. Furthermore, mass spectrometric analysis indicates the presence of vinyl acetate and various acetic acid esters. Therefore, the difference between the thermal transformation sequences of Y(OAc)O and products obtained in vicinal glycols can be attributed to the presence or absence of the glycol moieties: The acetate groups in the former product decomposed into volatile acetone and carbonate ions which remain in the coordination sites of the yttrium ions. On the other hand, the presence of glycol moieties in the latter enables the acetate groups to form volatile esters by reacting with the glycol moieties and be eliminated without the formation of carbonate species.

The surface areas of Y_2O_3 obtained by the thermal decomposition of P(1,2-PG) and P(1,2-BG) are much larger than those obtained from P(EG). The weight loss at around 600 °C observed in the TG profile of P(EG) (Fig. 2-3) suggests that the small surface area of P(EG)400 is due to the presence of a large amount of carbonaceous materials on the surface of the oxide phase formed at low temperatures. The crystallite size of P(1,2-PG)400 with the largest surface area (280 m^2/g) is 2.2 nm; its surface area calculated assuming that each Y_2O_3 particle is spherical with a diameter of 2.2 nm (crystallite size) is 540 m^2/g, which is significantly larger than the BET surface area.

Note that the diameter of the smallest voids in the closest packing of spherical particles with a diameter of 2.2 nm is 0.34 nm ($(2\sqrt{3}/3 - 1)D$, where D is the diameter of the spherical particles). However, the diameter of nitrogen molecules is typically assumed to be 0.45 nm (the area occupied by a nitrogen molecule is assumed to be 16.2 $Å^2$). Therefore, nitrogen molecules (adsorbate) cannot access the void spaces when the particles are closest-packed. The TEM image of P(1,2-PG)400 indicates that it is composed of aggregated particles with a size of ca. 12 nm (Fig. 2-5). A detailed

Fig. 2-5. TEM image of P(1,2-PG)400.

discussion regarding the morphology of Y_2O_3 nanoparticles is shown in chapter 3.

As shown in Fig. 2-6, the IR spectrum of P(1,2-PG)400 exhibits peaks at 1560, 1420 and 840 cm^{-1}; this is attributed to oxycarbonate species. The formation of this species can be ascribed to the reaction of RE oxides with atmospheric CO_2 since it is reported that RE oxides react with H_2O and/or CO_2 in air at room temperature yielding hydroxides and/or carbonate hydroxides [24].

2.3.3 Other RE oxides

Figure 2-7 shows the XRD patterns of the product obtained by the reaction of RE acetate hydrates in 1,2-PG. None of these patterns are found in the JCPDS cards. Based on the XRD patterns, we classify the products into two groups—Group A for La-Nd and Group B for Sm-Yb and Y.

The IR spectra of the products are shown in Fig. 2-8. Liquid 1,2-PG exhibits two bands in the 800–850 cm^{-1} region (Fig. 2-2c). Although both the product groups exhibit the peaks attributed to the glycol moieties, Group A products exhibit peaks with low intensities. This suggests that the glycol moieties are possibly present on the surface of the crystals. Therefore, the coordination states of 1,2-PG to RE ion for Group A and Group B products are completely different. The stretching vibration bands attributed to the acetate groups are observed at around 1610 and 1480 cm^{-1} for both product groups. Moreover, Group A products exhibit two sharp bands at around 3500 and 3600 cm^{-1}, while Group B products do not exhibit these bands. This result suggests that Group A products possess structural OH groups, while Group B products do not.

Figure 2-9 shows the thermal decomposition behaviour of the as-synthesized products obtained from La and Yb acetates as the representatives for Group A and Group B, respectively. Figure 2-10 shows the XRD patterns of the samples obtained by the calcination of the La and Yb products at various temperatures. For the La product,

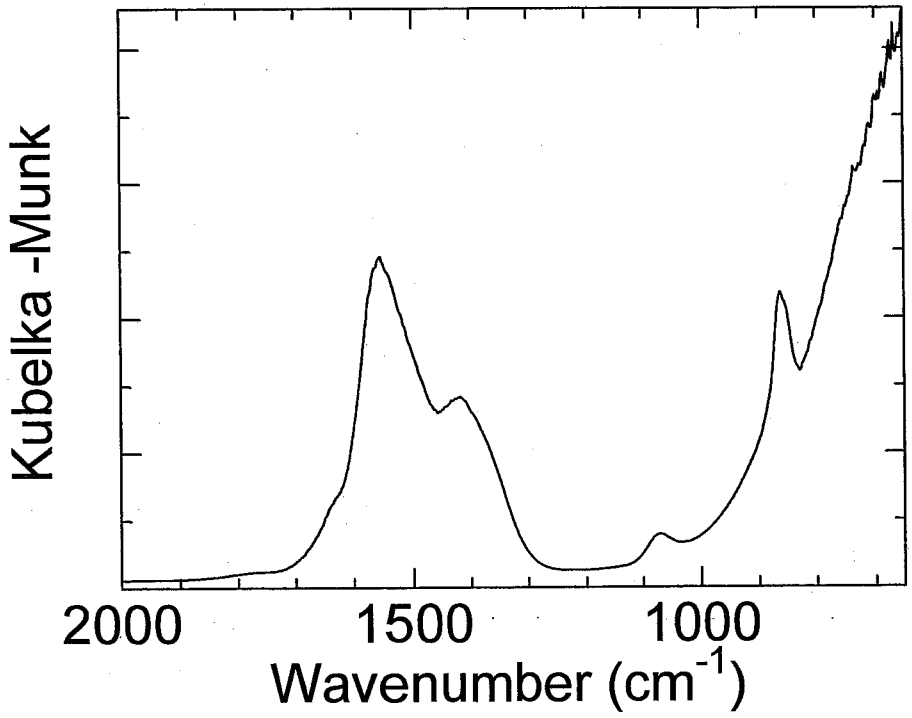

Fig. 2-6. IR spectrum of P(1,2-PG)400.

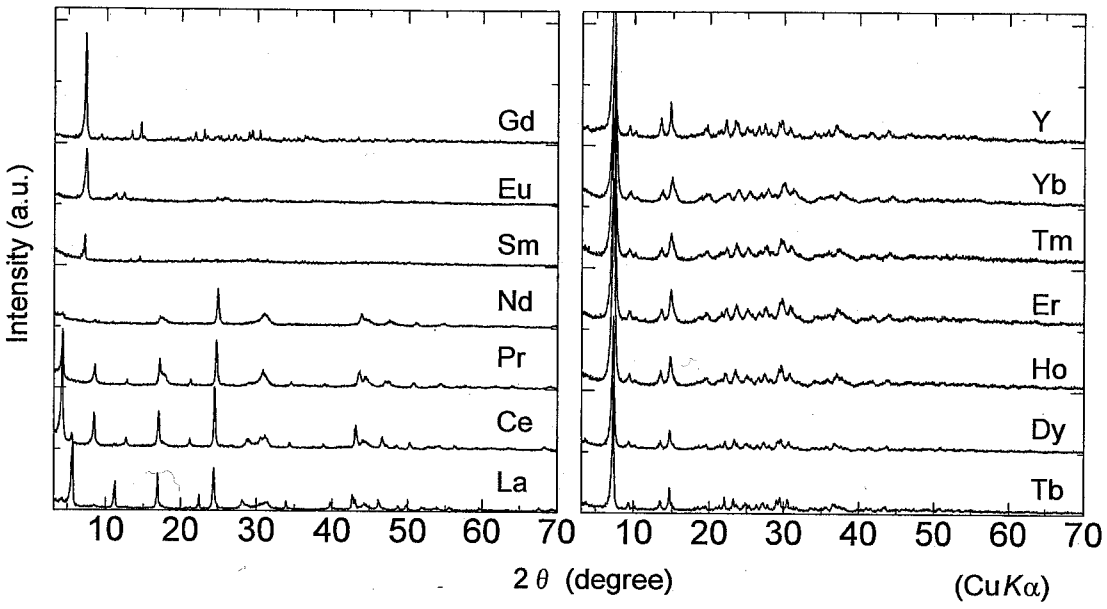

Fig. 2-7. XRD patterns of the products obtained by the reaction of rare earth acetate hydrates in 1,2-propanediol at 300 °C for 2 h.

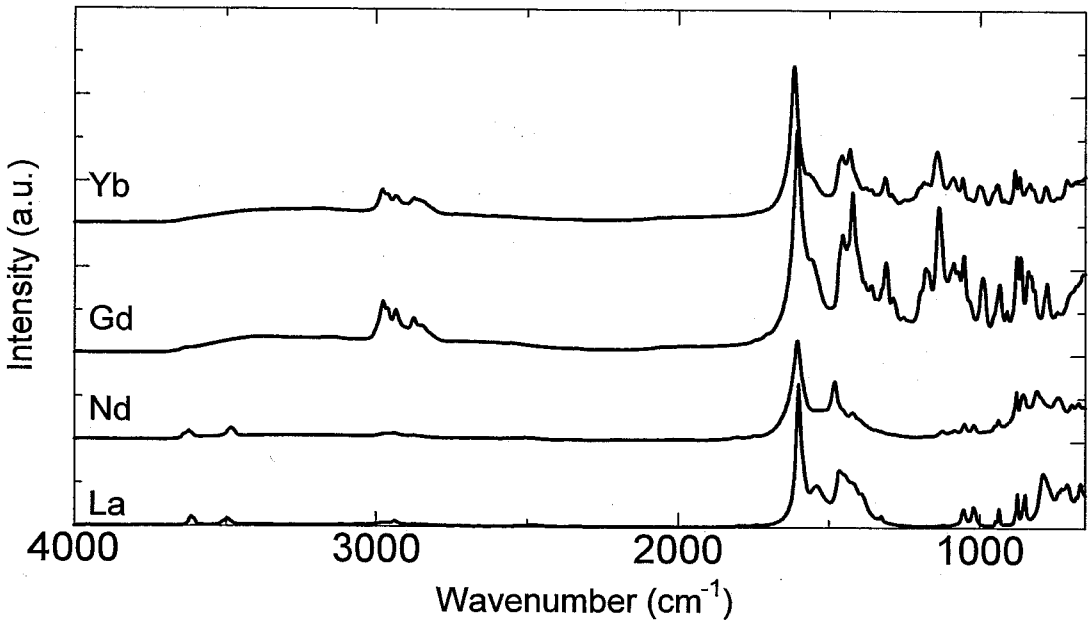

Fig. 2-8. IR spectra of the products.

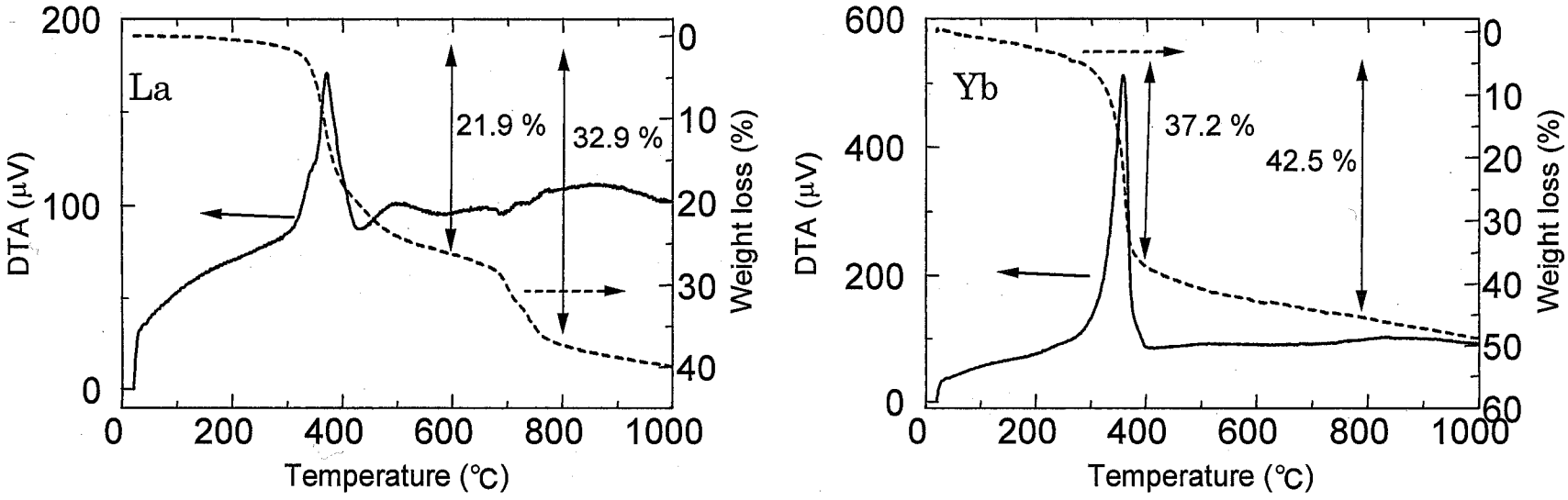

Fig. 2-9. TG-DTA profiles of the products obtained by reaction of La and Yb acetate hydrate in 1,2-propanediol as the representative data for the Group A and Group B products, respectively.

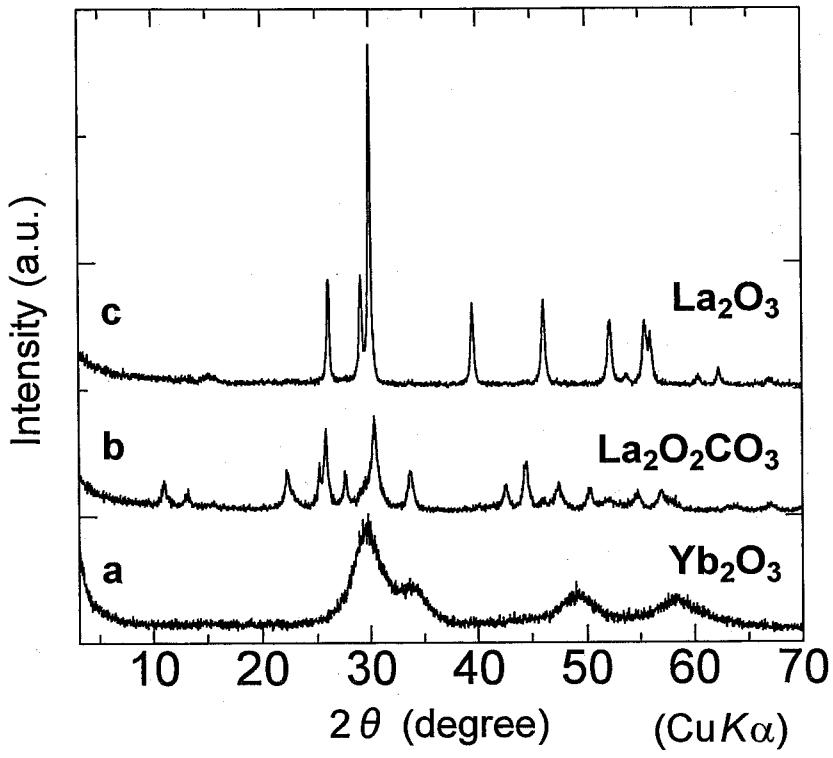

Fig. 2-10. XRD patterns of the samples obtained by calcination of the La or Yb products; a, Yb, 400 °C; b, La, 600 °C; c, La, 800 °C. Identified phases are shown in the figure.

weight loss accompanied by an exothermic peak in DTA is observed at 400 °C, and lanthanum carbonate oxide (JCPDS card No. 37-0804) is crystallized at 600 °C. Another weight loss associated with an endothermic peak is observed at around 700 °C due to the decomposition of lanthanum carbonate oxide to lanthanum oxide. This profile is essentially identical to that of the other Group A products, except for Ce. In the case of Ce, weight loss associated with an exothermic peak in DTA is observed at around 300 °C and CeO_2 (JCPDS card No. 34-0394) is directly crystallized by calcination at 400 °C.

On the other hand, the thermal analyses of the Yb product in Group B reveals weight loss accompanied by an exothermic peak at 350 °C, and the sample calcined at 400 °C for 30 min exhibits the XRD pattern attributed to ytterbium oxide (JCPDS card No. 43-1037). Although gradual weight loss occurs at temperatures higher than 400 °C, no heat response is detected. The TG-DTA profiles of the other Group B products, except for Sm and Eu, are essentially identical to that of the Yb product. Therefore, Group B products (except for Sm and Eu) decompose directly to the oxide phase at ~400 °C.

In the cases of Sm and Eu, the yields of the glycothermal products were much smaller than those of the other products. This result suggests that the glycothermal reaction of $Sm(OAc)_3$ and $Eu(OAc)_3$ proceeds incompletely and large amounts of RE ions remain in the glycol solution. The TG-DTA profile of the Sm product exhibits a much broader exothermic peak at around 350 °C as compared to the Yb product, and the sample decomposes to Sm_2O_3 (JCPDS card No. 15-0813) at ~400 °C. Exothermic and endothermic peaks at around 300 and 550 °C, respectively, are observed in the TG-DTA profile of the Eu product. The endothermic peak is ascribed to the decomposition of the oxycarbonate phase (JCPDS card No. 25-0334).

Table 2-1 lists the phases identified from the XRD patterns, BET surface areas and crystallite sizes of the samples obtained by the 400 °C calcination of the products. Group B products are transformed to the oxide phase with the cubic structure; they have

Table 2-1 BET surface area and crystallite size of the sample obtained by 400 °C calcination of the product formed by reaction rare earth acetate in 1,2-PG.

Rare earth elements	Product phase[a)]	BET surface area (m^2/g)	Crystallite size (nm)[b), c)]
La	$La_2O_2CO_3$	-	-
Ce	CeO_2	85	-
Pr	$Pr_2O_2CO_3$	-	-
Nd	$Nd_2O_2CO_3$	-	-
Sm	Sm_2O_3	27	-
Eu	$Eu_2O_2CO_3$+Eu_2O_3	11	-
Gd	Gd_2O_3	122 (25)[d)]	1.6
Tb	Tb_2O_3	118	3.0
Dy	Dy_2O_3	136 (42)	1.9
Ho	Ho_2O_3	140	1.9
Er	Er_2O_3	132 (39)	2.5
Tm	Tm_2O_3	121	2.6
Yb	Yb_2O_3	128 (35)	2.8
Y	Y_2O_3	280	2.2

a) Phase identified by XRD pattern.
b) Calculated from the FWHM of the 222 diffraction peak by using Scherrer's equation.
c) Although calculated crystallite size has only one significant figure, data to one decimal place are given in the table because measured FWHM has more than two significant figures.
d) Data in parentheses are the BET surface areas of the sample after calcintion at 600 °C.

large surface areas (>100 m^2/g) and small crystallite sizes (<3 nm), except for Sm and Eu. The low surface areas of Sm_2O_3 and Eu_2O_3 can be attributed to amorphous phases and/or oxycarbonate species present in the products.

As described in Introduction, several studies have reported the synthesis of RE_2O_3 nanoparticles. However, few reports have discussed the surface areas of the nanoparticles of RE_2O_3, except for CeO_2. It is reported that the Y_2O_3 nanoparticles synthesized by alkalide reduction and subsequent oxidation have a surface area of 109 m^2/g, but the sample is amorphous [1]. Hussein et al. investigated the thermal decomposition of $Y(OAc)_3 \cdot 4H_2O$, $Y(NO_3)_3 \cdot 5H_2O$ and $Y_2(C_2O_4)_3 \cdot 8H_2O$ [8], and reported that $Y(NO_3)_3 \cdot 5H_2O$ decomposes at 450 °C yielding Y_2O_3 with a large surface area (58 m^2/g), while $Y(OAc)_3 \cdot 4H_2O$ and $Y_2(C_2O_4)_3 \cdot 8H_2O$ decompose at 650 °C yielding Y_2O_3 with surface areas of 55 and 12 m^2/g, respectively. They also reported that Er_2O_3 obtained by the decomposition of $Er(OAc)_3 \cdot 4H_2O$ at 800 °C has a surface area of 55 m^2/g [9]. The RE_2O_3 (RE = Gd-Yb, Y) samples obtained by the 400 °C calcination of the products synthesized by the reaction of RE acetate in 1,2-PG have markedly large surface areas as compared to the reported values. Furthermore, the crystallite sizes of these samples are the smallest among those reported thus far.

2.4. Conclusions

The calcination of the products obtained by the reaction of RE (Y, Gd-Yb) acetate hydrates in EG, 1,2-PG and 1,2-BG at 300 °C yields crystalline RE oxides at temperatures as low as 400 °C. The thus-obtained Y_2O_3 sample has a significantly large surface area (280 m^2/g) and small crystallite size (2.2 nm). The other RE oxides obtained by this method also have large surface areas (>100 m^2/g). These surface areas are much larger than those reported thus far.

References

[1] J. A. Nelson, M. J. Wagner, Chem. Mater., 14 (2002) 915.

[2] J. A. Nelson, E. L. Brant, M. J. Wagner, Chem. Mater., 15 (2003) 688.

[3] T. Liu, Y. Zhang, H. Shao, X. Li, Langmuir, 19 (2003) 7569.

[4] H. Eilers, B. M. Tissue, Mater. Lett., 24 (1995) 261.

[5] B. M. Tissue, H. B. Yuan, J. Solid. State Chem., 171 (2003) 12.

[6] W. Krauss, R. Birringer, Nano. Struct. Mater., 9 (1997) 109.

[7] A. Konrad, U. Herr, R. Tidecks, F. Kummer, K. Samwer, J. Appl. Phys., 90 (2001) 3516.

[8] H. M. Ismail, G. A. M. Hussein, Powder Technol., 87 (1996) 87.

[9] G. A. M. Hussein, Powder Technol., 118 (2001) 285.

[10] I. W. Lenggoro, Y. Itoh, K. Okuyama, T. O. Kim, J. Mater. Res. 19 (2004) 3534.

[11] J. Dhanaraj, R. Jagannathan, T. R. N. Kutty, C.-H. Lu, J. Phys. Chem. B, 105 (2001) 11098.

[12] T. Ye, Z. Guiwen, Z. Weiping, X. Shangda, Mater. Res. Bull., 32 (1997) 501.

[13] S. Polizzi, S. Bucella, A. Speghini, F. Vetrone, R. Naccache, J. C. Boyer, J. A. Capobianco, Chem. Mater., 16 (2004) 1330.

[14] T. Tsuzuki, E. Pirault, P. G. McCormick, Nano. Struct. Mater., 11 (1999) 125.

[15] R. Bazzi, M. A. Flores-Gonzalez, C. Louis, K. Lebbou, C. Dujardin, A. Brenier, W. Zhang, O. Tillement, E. Bernstein, P. Perriat, J. Luminescence., 102-103 (2003) 445.

[16] F. Söderlind, H. Pedersen, R. M. Petoral Jr., P.-O. Käll, K. Uvdal, J. Colloid Interface Sci., 288 (2005) 140.

[17] R. Bazzi, A. Brenier, P. Perriat, O. Tillement, J. Luminescence, 113 (2005) 161.

[18] T. Hirai, Y. Asada, I. Komasawa, J. Colloid Interface Sci., 276 (2005) 339.

[19] T. Masui, K. Fujiwara, K. Machida, G. Adachi, T. Sakata, H. Mori, Chem. Mater.,

9 (1997) 2197.

[20] L. Yin, Y. Wang, G. Pang, Y. Koltypin, A. Gedanken, J. Colloid Interface Sci., 246 (2002) 78.

[21] T. Masui, H. Hirai, N. Imanaka, G. Adachi, T. Sakata, H. Mori, J. Mater. Sci. Lett., 21 (2002) 489.

[22] H. Kominami, M. Inoue, T. Inui, Nippon Kagaku Kaishi (J. Chem. Soc. Jpn.), (1993) 605.

[23] M. Inoue, T. Nishikawa, H. Kominami, T. Inui, J. Mater. Sci., 35 (2000) 1541.

[24] S. Bernal. F. J. Botana, R. Garcia, J. M. RodriGuez-Izquierdo, React. Solids, 23 (1987) 23.

Chapter 3

Synthesis of nano-hollow shaped rare earth oxides by glycothermal treatment of rare earth acetates and subsequent calcination

3.1 Introduction

Recently, there has been intense interest in fabricating micrometer- and nanometer-sized hollow particles [1]. These hollow particles often exhibit properties that are substantially different from those of conventional ordinary particles; e.g., low density, large surface area, stability, surface permeability and so on. Rare earth (RE) oxides have physical and chemical properties suitable for various applications as, for example, phosphors [2-4], catalysts [5-9] or catalyst supports [10,11]. Therefore, it is quite interesting to develop methods to synthesize nano-hollow shaped RE oxides.

Hollow shaped RE oxides have been synthesized by a template method, spray pyrolysis, etc. [12-19]. A synthesis of various RE oxides (La_2O_3, Y_2O_3, Lu_2O_3, and CeO_2) has been developed by using carbonaceous polysaccharide microspheres as templates [12]. In spray pyrolysis, a solution of metal salts is sprayed onto a hot wall reactor, where the reaction occurs in dispersed droplets forming the product particles. Kang et al. prepared Gd_2O_3:Eu and Y_2O_3:Eu particles with hollow structures by spray pyrolysis of nitrate solutions containing polyethylene glycol [15,16].

Chapter 2 manly discussed the thermal decomposition behavior of the product obtained by glycothermal treatment of RE acetate in 1,2-propanediol (1,2-PG) and the surface area of RE oxides obtained by the thermal decomposition at low temperature. However, the detailed morphology or pore structure of RE oxide was not investigated.

In this chapter, the detailed physical properties of nano-hollow shaped RE oxide obtained by glycothermal treatment of RE acetate in 1,2-PG and subsequent calcination were discussed.

3.2. Experimental

3.2.1 Glycothermal treatment

Yttrium acetate hydrate (8.453 g, 25 mmol) was suspended in 120 ml of 1,2-PG in a test tube serving as autoclave liner. The tube was placed in a 300-ml autoclave. An additional 40 ml of 1,2-PG was placed in the gap between the autoclave wall and the test tube. The autoclave was completely purged with nitrogen, heated to 300 °C at a rate of 2.3 °C/min, and kept at that temperature for 2 h. After the assembly was rapidly cooled to room temperature, the resulting product was collected by centrifugation. The product was washed with methanol by vigorous mixing and centrifuging, and then air-dried. For calcination, the products were heated with a rate of 10 °C/min and held at the prescribed temperature for 30 min in a box furnace. The amount of the product obtained in 1,2-PG was ca. 5.5 g, and the ceramic yield calculated on the basis of the observed weight loss of the product yielding yttrium oxide by calcination at 1000 °C was above 90 %.

RE oxides obtained by calcination of the products are designated as RE_2O_3(calcination temperature). For example, Y_2O_3(400) means the product obtained by reaction of yttrium acetate in 1,2-PG followed by calcination at 400 °C.

3.2.2 Characterization

Since a previous report [20] indicated that RE oxide reacts with H_2O and/or CO_2 in air at room temperature giving hydroxide or carbonate hydroxide ($RE(OH)CO_3$), the characterization of the calcined samples was carried out within 24 h after calcination.

The true density of the product was determined by using a pycnometer. X-ray powder diffraction (XRD: Model XD-D1 Shimadzu, Kyoto, Japan) was recorded using Cu$K\alpha$ radiation and a carbon monochromator. The crystallite size of Y_2O_3 was calculated from the half-height width of the peak at 29.1° by Scherrer equation. Simultaneous

thermogravimetric and differential thermal analyses were performed on a thermal analyzer (Model DTG-500, Shimadzu, Kyoto, Japan) at a rate of 5 °C/min in a 40 ml/min flow of dried air. Specific surface area was calculated using the BET single-point method on the basis of N_2 uptake measured at 77 K using a Micrometritics Flowsorb II 2300 sorptionmeter. Nitrogen adsorption isotherm was determined using a volumetric gas-sorption system (Model Autosorb-1, Quantachrome, USA) and the pore-size distribution was calculated by the BJH method on the basis of the desorption branch of the isotherm. The morphology of the products was observed with a scanning electron microscope (SEM), Hitachi S-2500CX, or a transmission electron microscope (TEM), Hitachi H-800, operated at 200 kV.

3.3. Results and Discussion

3.3.1. Physical properties of Y_2O_3 obtained by glycothermal treatment of yttrium acetate and subsequent calcination

Figure 3-1 shows the XRD patterns of the as-synthesized and calcined products. The intense peak at a low angle (7.3° 2θ) suggests that the as-synthesized product has a layer structure. As shown in chapter 2, the FT-IR spectra (data not shown) of the product indicated the presence of the glycol moieties and the acetate ligands. In the thermal decomposition behaiviour of the as-synthesized product, a large weight decrease associated with an exothermic peak was detected at 360 °C (Fig. 3-2). The as-synthesized product was decomposed to Y_2O_3 by calcination at 400 °C. The XRD peaks of the sample calcined above 400 °C became gradually sharp, and coincided with the cubic structure of Y_2O_3 (JCPDS: No. 41-1105). The crystallite size and surface area of Y_2O_3 are summarized in Table 3-1. Y_2O_3(400) had quite a large surface areas (> 200 m^2/g) and a small crystallite size (2^{-2} nm). The surface area decreased and crystallite size increased by calcination at higher temperatures. The surface area of Y_2O_3(700) was

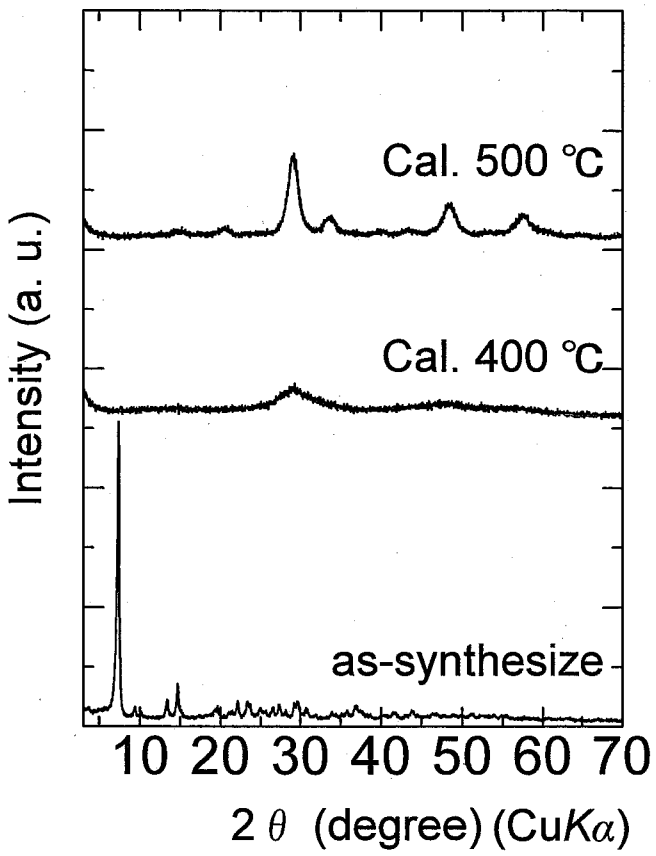

Fig. 3-1. XRD patterns of the product obtained by the reaction of yttrium acetate hydrate in 1,2-PG at 300 ℃ for 2 h and the samples obtained by calcination thereof at 400 and 500 ℃.

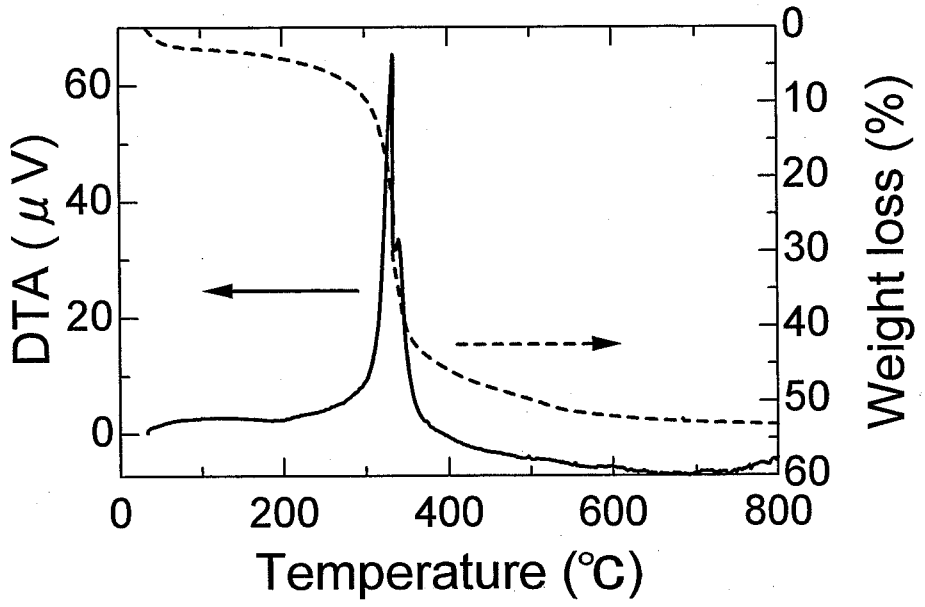

Fig. 3-2. TG-DTA profiles of the product obtained by the reaction of yttrium acetate hydrate in 1,2-PG at 300 °C for 2 h.

Table 3-1Crystallite size and surface area of Y_2O_3 obtained by calcination of the product formed in 1,2-PG.

Calcination temperature (°C)	Crystallite size[a)] (nm)	BET surface area[b)] (m^2/g)
400	$2^{.2}$	280
500	$4^{.1}$	99
600	$9^{.4}$	52
700	$20^{.9}$	17

a) Calculated from half-height width of 222 diffraction peak (29.1° 2θ) by using the Scherrer equation.

b) Calculated using BET single-point method.

17 m^2/g and crystallite size was about 20^{-9} nm. The Y_2O_3 crystals were significantly grown at the temperatures lower than the Tammann temperature (625 °C) [21], which may suggest that the water, generated by the combustion of the organic moieties remaining in the as-synthesized product, contributed to the crystal growth of Y_2O_3.

The SEM images of the as-synthesized product and Y_2O_3(400) are shown in Fig. 3-3. The morphology of the Y_2O_3(400) was essentially identical with that of the as-synthesized product. However, the TEM images indicated that the morphology was completely altered by calcination (Fig. 3-4). The as-synthesized product was composed of nearly spherical dense particles with 17-33 nm diameter (weight mean diameter, 28 nm) and the particle size was essentially identical with the crystallite size ($28^{.5}$ nm) calculated from the diffraction peak at 7.3°. However, the particle size determined from TEM photographs has some errors because of carbon contamination due to beam damage of the organic moieties remaining in quantity in the as-synthesized particles; the real particle size may be smaller than that determined by the TEM image. On the other hands, Y_2O_3(400) was composed of nano hollow spheres with the outer diameter of 7-18 nm and the inner diameter of 2-8 nm (Fig. 3-5). The morphology of Y_2O_3(500) was essentially identical with that of Y_2O_3(400). The wall thickness was 2.5-5 nm, which corresponds to the size of one or two crystallites.

From the weight mean outer and inner diameters of the nano hollow spheres (12 nm and 5.8 nm, respectively), the empirical weight of a hollow sphere was calculated to be 4.0×10^{-18} g assuming the density of Y_2O_3 to be 5.03 g/cm^3 (calculated from the unit cell parameter of the cubic phase of Y_2O_3). From the observed weight loss (49.5 %) due to formation of Y_2O_3 from the as-synthesized product, the average weight of the originating particle was estimated to be 8×10^{-18} g. Taking into account of the true density of the as-synthesized product (1.75 g/cm^3), the average particle size of the product was calculated to be 21 nm, which is in fairly good agreement with the

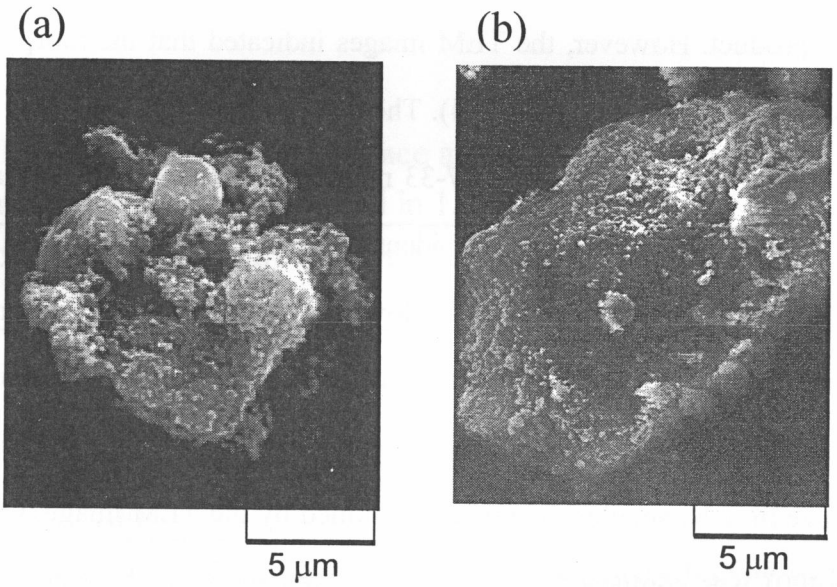

Fig. 3-3. SEM images of: (a), the product obtained by reaction of yttrium acetate hydrate in 1,2-PG at 300 °C for 2 h; (b), Y_2O_3(400).

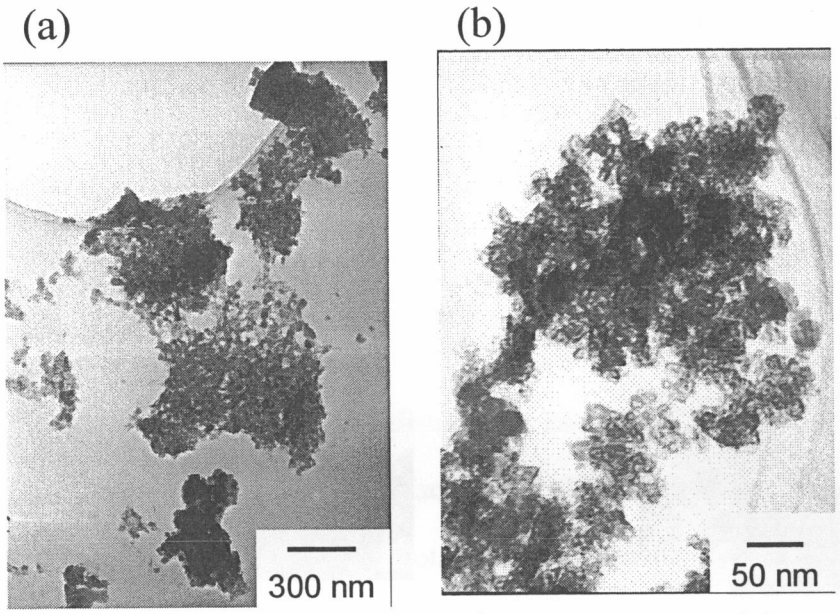

Fig. 3-4. TEM image of: (a), the product obtained by reaction of yttrium acetate hydrate in 1,2-PG at 300 °C for 2 h; (b), Y_2O_3(400).

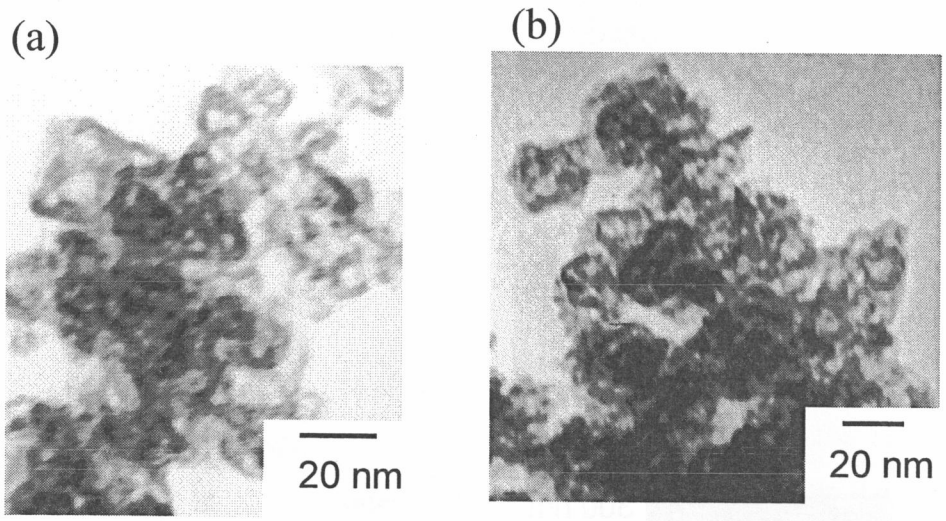

Fig. 3-5. TEM images of: (a), Y_2O_3(400); and (b), Y_2O_3(500).

observed weight mean diameter (28 nm) of the as-synthesized product. These arguments lead to the conclusion that a hollow sphere was formed from a particle of the product.

The N_2 adsorption isotherms of Y_2O_3(400) and Y_2O_3(500) are shown in Fig. 3-6. Hysteresis loop can be assigned as E-type (de Boer classification) [22], indicating that the sample has capillaries with the ink-bottle shape. The pore-size distribution had a sharp peak at 3.5 nm and a broad peak at 33.4 nm. The total surface area calculated by the V-t plot and BET surface area calculated from the multi point method were 285 and 343 m^2/g, respectively, and the external surface area after closing the mesopores by capillary condensation was calculated to be 65 m^2/g. The difference between the total and the external surface areas was 220 m^2/g. Therefore, the most part of the surface area of the sample is due to mesopores.

In the case of Y_2O_3(500), the pore size distribution had two broad peaks around 3 and 15 nm. In addition, the total and external surface areas calculated by the V-t plot were 129 and 63 m^2/g, respectively. Although the total surface area of Y_2O_3(500) was much smaller than that of Y_2O_3(400), the external surface area of Y_2O_3(500) was essentially identical with that of Y_2O_3(400). The particle size calculated assuming that each Y_2O_3 particle is spherical with surface area of 64 m^2/g was 18.6 nm, which is in good agreement with the outer diameter of the nano hollow spheres observed from the TEM image. Therefore, the outer diameter of nano hollow spheres of Y_2O_3(400) was maintained, but mesopores formed between primary particles of Y_2O_3 disappeared by sintering of the primary particles.

From the results mentioned above, change in morphology and pore-structure of the product can be illustrated as shown in Fig. 3-7. Ignition by the reaction between the glycol moieties and oxygen in air occurred on the surface of the as-synthesized spherical particles during calcination, and the heat generated by combustion would decompose the organic moieties inside the particles, resulting in an increase in the

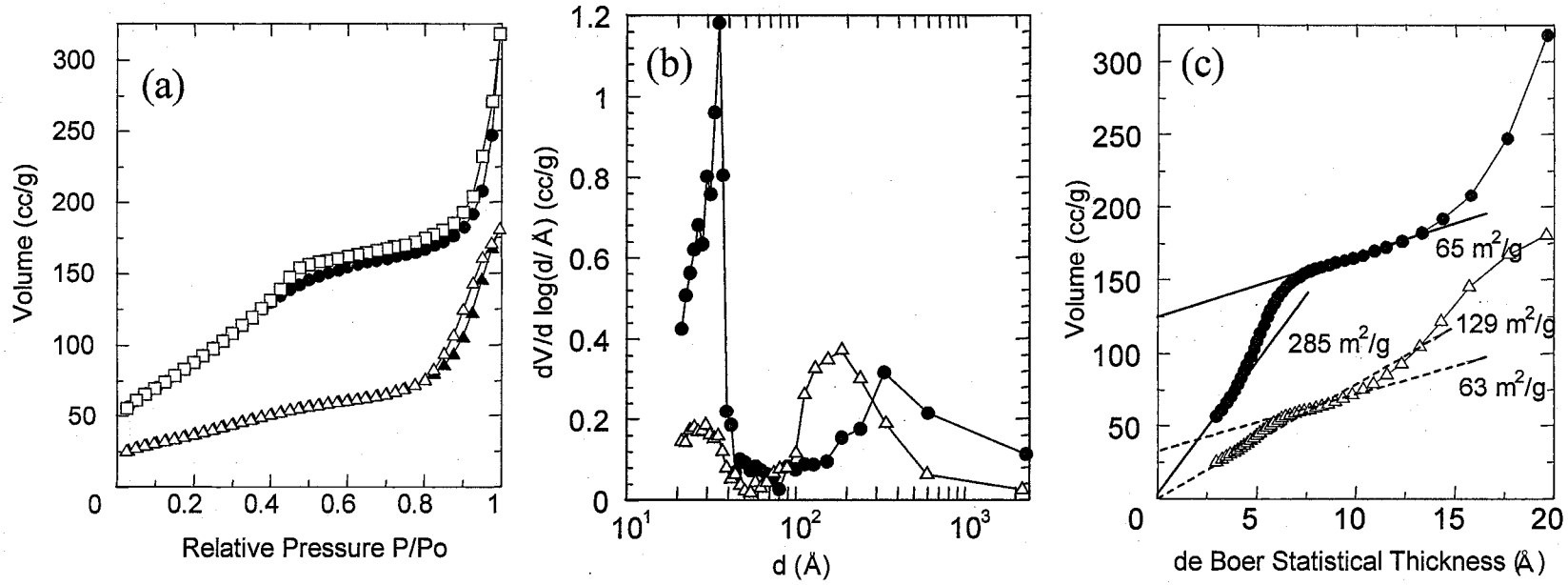

Fig. 3-6. Nitrogen adsorption isotherm (a), pore size distribution (b), and V-t plot (c) of: (○), Y_2O_3(400); (△), Y_2O_3(500).

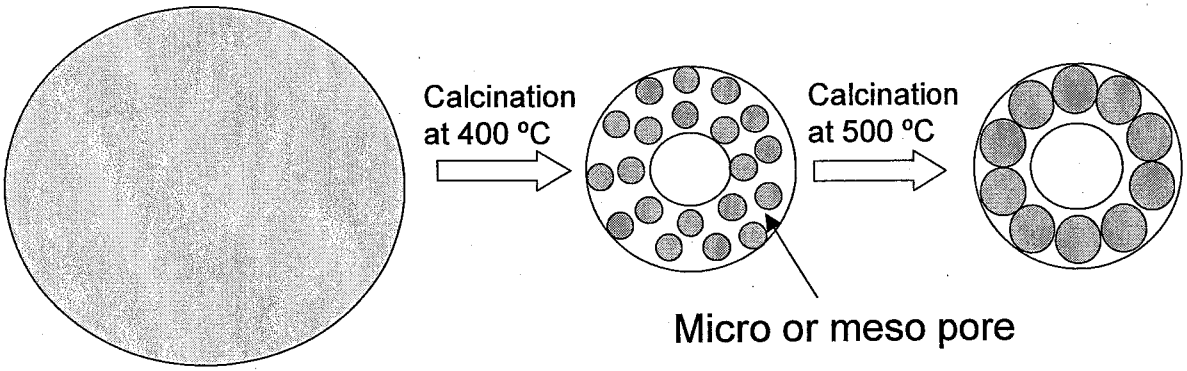

Fig. 3-7. Cartoon for the change in morphology and pore structure by calcination.

internal pressure in the particle. When the as-synthesized product was transformed into Y_2O_3 with the progress of combustion, internal pressure causes the formation of the hollow shape of aggregates of the Y_2O_3 crystals. The nano hollow sphere of Y_2O_3(400) had many pores generated between primary particles. Although the Y_2O_3 sample maintained the nano hollow shape even after calcination at 500 °C, the surface area of Y_2O_3(500) decreased by disappearance of the mesopores, which is due to crystal growth of Y_2O_3 from 2 to 4 nm.

3.3.2. Physical properties of RE_2O_3 obtained by glycothermal treatment of RE acetates and subsequent calcination

The XRD patterns of the as-synthesized products obtained for Gd, Dy, Er and Yb are shown in Fig. 3-8. The as-synthesized products had the layer structure essentially identical with the product obtained from yttrium acetate. The morphologies of the as-synthesized products are shown in Fig. 3-9. The as-synthesized product of Gd was composed of plate-shaped particles and the Dy product was comprised of a mixture of plate-shaped particles and spherical particles with about 25 nm diameter. The morphologies of the as-synthesized products of Er and Yb were spherical with the average diameters of 21.6 and 11.4 nm, respectively. The plate-shaped particles were formed in RE element with larger ionic size. The size of the spherical particle decreased with the decrease of ionic size of the RE element.

The thermal decomposition behavior of the as-synthesized products of Gd, Dy, Er and Yb was essentially identical with that of the Y product. As shown in Fig. 3-10, the products were transformed into RE oxides by calcination at 400 °C. The crystallite size and BET surface area are shown in Table 3-2. RE_2O_3(400) had high surface areas (> 100 m^2/g) and small crystallite sizes (< 3 nm). Although the crystallite size increased with the decrease of ionic size, the difference in BET surface area was not significant. The

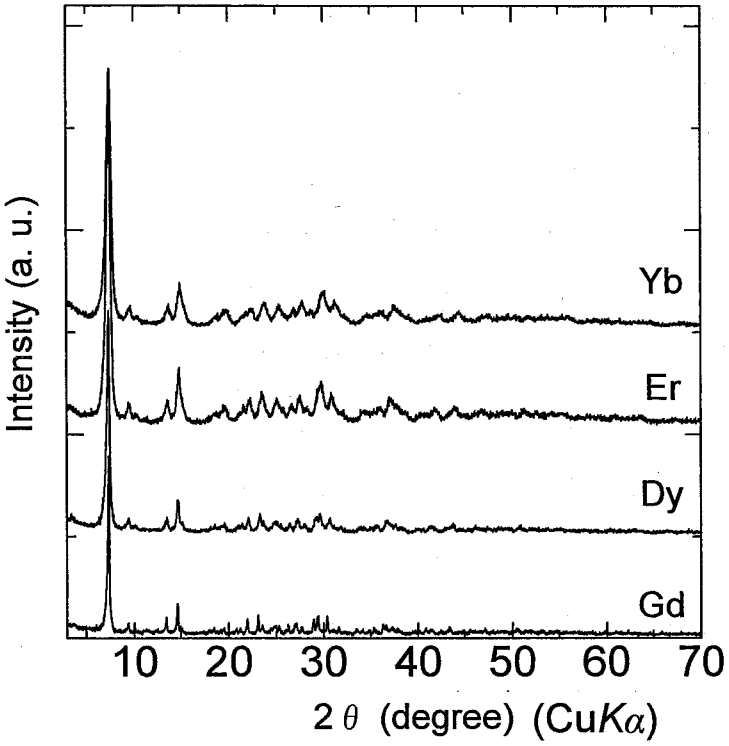

Fig. 3-8. XRD patterns of the as-synthesized products obtained by the reaction of RE acetate hydrates in 1,2-PG at 300 °C for 2 h.

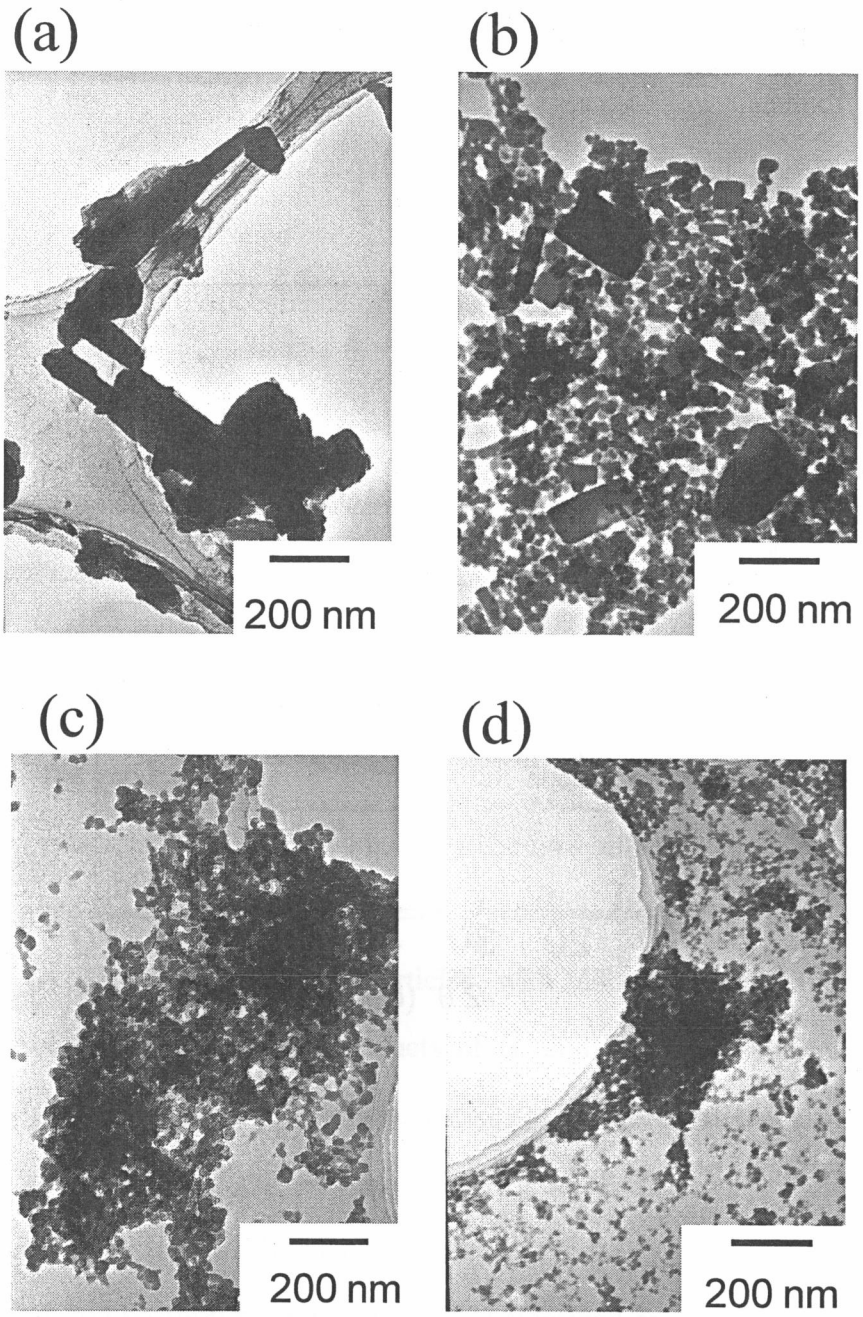

Fig. 3-9. TEM images of the as-synthesized products obtained by the reaction of RE acetate hydrate in 1,2-PG at 300 °C for 2 h: (a), Gd; (b), Dy; (c), Er; and (d), Yb.

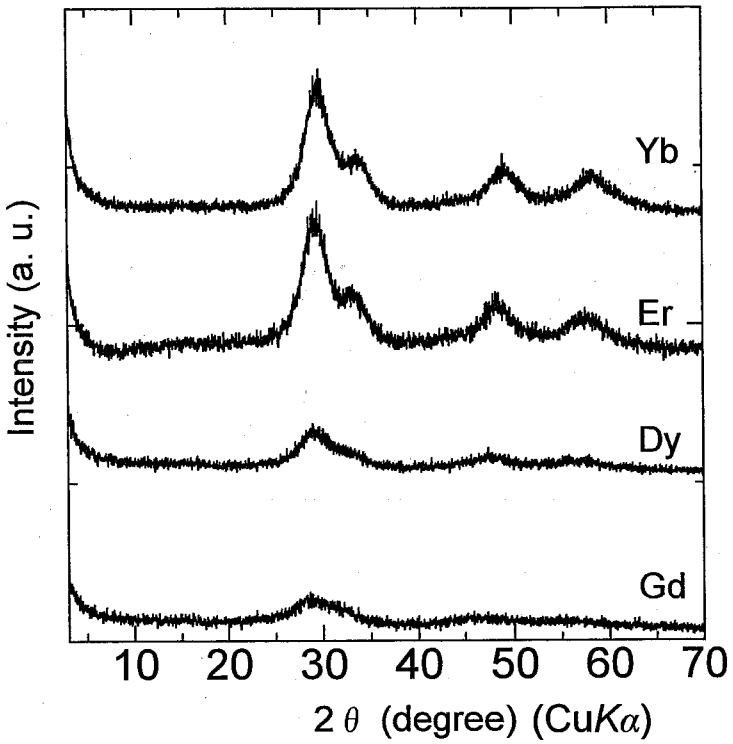

Fig. 3-10. XRD patterns of $RE_2O_3(400)$.

Table 3-2 Crystallite size and surface area of RE oxides obtained by calcination of the products formed in 1,2-PG.

Sample	Crystallite size (nm)[a)]	BET surface area (m^2/g)[b)]
Gd_2O_3	1.6	122 (25)[c)]
Dy_2O_3	1.9	136 (42)
Er_2O_3	2.5	132 (39)
Yb_2O_3	2.8	128 (35)

a) Calculated from half-height width of 222 diffraction peak (29.1° 2θ) by using the Scherrer equation.
b) Calculated using BET single-point method.
c) Data in parentheses are the BET surface areas of the samples after calcintion at 600 °C.

surface area was drastically decreased by calcination at 600 °C.

The morphologies of $RE_2O_3(400)$ are shown in Fig. 3-11. $Gd_2O_3(400)$ was composed of porous solids having a plate-shaped outline, and $Dy_2O_3(400)$ was a mixture of porous plate-shaped particles and nano hollow spheres with an outer diameter of about 10 nm and inner diameter of about 3 nm. The morphologies of $Er_2O_3(400)$ and $Yb_2O_3(400)$ were nano hollow spheres with the outer diameters of about 9 and 8 nm and the inner diameters of about 4 and 3 nm, respectively. When the as-synthesized product was composed of spherical particles, nano hollow shaped particles were formed. Therefore, the formation mechanism of the nano hollow shaped RE_2O_3 was essentially identical with that of $Y_2O_3(400)$.

The results for the nitrogen adsorption isotherm are shown in Fig. 3-12. A large amount of nitrogen was adsorbed at low P/P_0 (< 0.03) on all the samples, suggesting that the samples had micro or meso pores formed between primary particles. All of the samples exhibited the hysteresis loop, which were identified as E type according to de Boer classification, indicating the presence of ink-bottle shaped voids. $Gd_2O_3(400)$ and $Dy_2O_3(400)$ adsorbed more nitrogen molecules at higher P/P_0 than $Er_2O_3(400)$ and $Yb_2O_3(400)$. This indicates the difference in aggregation of the porous solids or nano hollow shaped particles.

3.4 Conclusions

The products obtained by the reaction of yttrium acetate hydrate in 1,2-PG at 300 °C contained both the acetate group and the glycol moieties, and were decomposed to yttrium oxide by calcination at 400 °C. $Y_2O_3(400)$ was composed of nano hollow spheres with the outer diameter of 7-18 nm and inner diameter of 2-8 nm. The nano hollow spheres had many pores generated between Y_2O_3 crystallites. The Y_2O_3 sample maintained the nano hollow shape even after calcination at 500 °C, but the mesopores

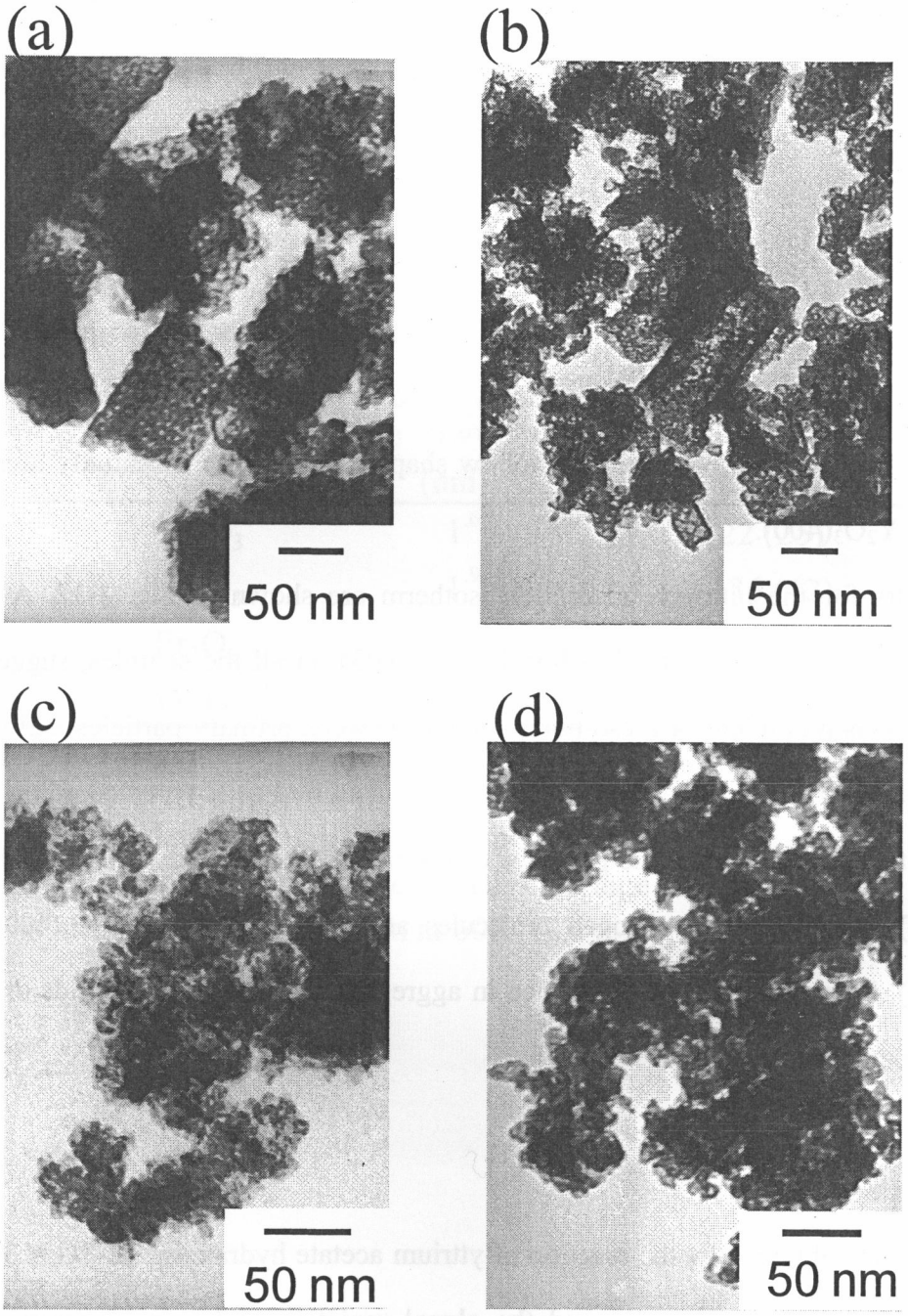

Fig. 3-11. TEM images of $RE_2O_3(400)$: (a), Gd; (b), Dy; (c), Er; and (d), Yb.

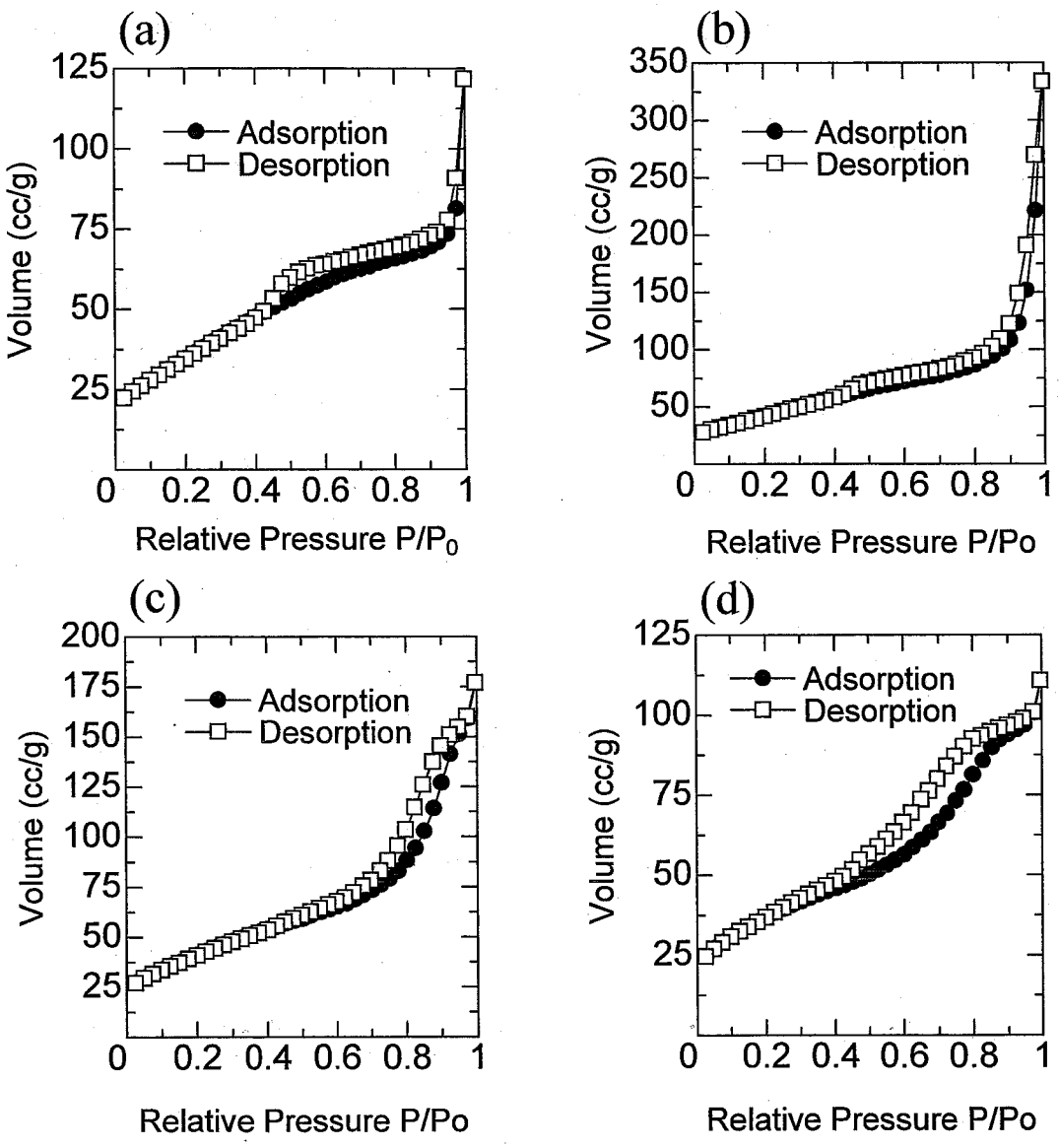

Fig. 3-12. Nitrogen adsorption isotherms of: (a), Gd_2O_3(400); (b), Dy_2O_3(400); (c), Er_2O_3(400); and (d), Yb_2O_3(400).

disappeared. Gd_2O_3(400) was composed of porous solids having a plate-shaped outline, and Dy_2O_3(400) was a mixture of porous plate-shaped particles and nano hollow spheres, while the morphologies of Er_2O_3(400) and Yb_2O_3(400) were nano hollow spheres.

References

[1] F. Caruso, R. A. Caruso, H. Möhwald, Science, 282 (1998) 1111.

[2] P. K. Sharma, M. H. Jilavi, R. Nass, H. Schmidt, J. Luminescence, 82 (1999) 187.

[3] T. Ye, Z. Guiwen, Z. Weiping, X. Shangda, Mater. Res. Bull., 32 (1997) 501.

[4] T. Hirai, Y. Asada, I. Komasawa, J. Colloid Interface Sci., 276 (2005) 339.

[5] Kh. M. Minachev, Y. S. Khodakov, V. S. Nakhshunov, J. Catal., 49 (1977) 207.

[6] Y. Fukuda, H. Hattori, K. Tanabe, Bull. Chem. Soc. Jpn., 51 (1978) 3150.

[7] B. H. Davis, Ind. Eng. Chem., Prod. Res. Dev., 21 (1982) 398.

[8] T. Yamaguchi, N. Ikeda, H. Hattori, K. Tanabe, J. Catal., 67 (1981) 324.

[9] K. Asami, K. Kusakabe, N. Ashi, Y. Ohtsuka, Appl. Catal. A: General, 156 (1997) 43.

[10] G. Tsuboi, M. Haneda, Y. Nagao, Y. Kintaichi, H. Hamada, J. Jpn. Petrol. Inst., 48 (2005) 53.

[11] J. Guzman, A. Corma, Chem. Commum., (2005) 743.

[12] X. Sun, J. Liu, Y. Li, Chem. Eur. J.,12 (2006) 2039.

[13] C. Han, X. Wu, Y. Lin, G. Gu, X. Fu, Z. Hi, J. Mater. Sci., 41 (2006) 3679.

[14] H. Wang, R. Wang, X. Sun, R. Yan, Y. Li, Mater. Res. Bull., 40 (2005) 911.

[15] M. A. Lim, Y. C. Kang, H. D. Park, J. Electrochem. Soc., 148 (2001) H171.

[16] H. S. Roh, Y. C. Kang, H. D. Park, S. B. Park, Appl. Phys. A ,76 (2003) 241.

[17] J. R. Sohn, Y. C. Kang, H. D. Park, Jpn. J. Appl. Phys., 41 (2002) 3006.

[18] T. Tani, N. Watanabe, K. Takatori, S. E. Pratsinis, J. Am. Ceram. Soc., 86 (2003) 898.

[19] M. Kawashita, Y. Takayama, T. Kokubo, H. Takaoka, N. Araki, M. Hiraoka, J. Am. Ceram. Soc., 89 (2006) 1347.

[20] S. Bernal. F. J. Botana, R. Garcia, J. M. RodriGuez-Izquierdo, React. Solids, 4 (1987) 23.

[21] A. Ozaki ed. in Shokubai Chosei Kagaku: Chemistry of catalyst preparation, Kodansha Scientific, Tokyo, 1980, p. 189.

[22] J. M. Thomas and W. J. Rhomas in Principles and Practice of Heterogeneous Catalysis, VCH Publisher Inc., New York, USA, 1997, p. 282.

Chapter 4

Solvothermal treatment of rare earth chloride hydrates

4.1 Introduction

Metals, metal acetates, metal alkoxides or metal acetylacetonates are generally used as starting materials for solvothermal reactions [1]. Inoue et al. found that various mixed oxides were directly crystallized in solvothermal reaction in 1,4-butanediol (1,4-BG) at 200-300 °C [2-5]. The use of 1,4-BG is, in the most cases, essential for formation of crystalline products under the solvothermal conditions.

The use of metal chlorides has been scarcely examined, because hydrochloric acid, generated during the reaction, is corrosive to impair the metal such as wall of an autoclave. To avoid this, following methods are devised: (1) hydrolysis of a metal chloride, followed by the solvothermal reaction of thus-obtained hydroxide, (2) solvothermal reaction in the presence of amines to neutralize the librated acid. In the former method the resultant precursor hydroxide is generally gelatinous, so it is difficult to control the water content in the gel. When a hydroxide gel containing a large amount of water is allowed to react under the solvothemal conditions, the essential nature of the reaction is not different from that of hydrothermal reaction.

In this chapter, the author treats the solvothermal reaction of rare earth (RE) chloride hydrates in 1,4-BG in the presence of amine bases to neutralize the liberated acid. The crystalline structure of the products obtained by the reaction is clarified, and the relationship between the crystalline structure and ionic size of RE element is suggested.

4.2. Experimental

RE chloride hydrates were purchased from Wako Pure Chemical Industry. Guaranteed 1,4-BG (nacalai tesque) was used without further purification.

Yttrium chloride hexahydrate (7.58 g, 25 mmol) was suspended in 100 ml of 1,4-BG in a test tube serving as autoclave liner and hexylamine (20 ml) and 1,6-hexanediamine (16 ml) were added to the tube (N/Cl ≈ 5). Hexylamine was added to neutralize the liberated acid in the gas phase and 1,6-hexanadiamine, in the liquid phase. The tube was placed in a 300-ml autoclave. Additional 1,4-BG (30 ml) and hexylamine (10 ml) were placed in the gap between the autoclave wall and the test tube. The autoclave was completely purged with nitrogen, heated to 300 °C at a rate of 2.3 °C/min, and kept at that temperature for 2 h. After the assembly was cooled to room temperature, the resulting product was collected by centrifuging. The product was washed with methanol and deionized water repeatedly by vigorous mixing and centrifuging, and then air-dried.

X-ray powder diffraction (XRD: Model XD-D1 Shimadzu, Kyoto, Japan) was recorded using Cu K_α radiation and a carbon monochromator. For Rietveld analysis, the XRD pattern was measured on another diffractometer (Model Rint 2500, Rigaku, Tokyo, Japan) and analyzed by RIETAN-2000 program [6].

Diffuse reflectance FT-IR spectra of the products were recorded in the range 4000-700 cm^{-1} on a Nicolet spectrophotometer (Model Magna-IR 560, Madison, USA) and the back ground spectrum employed was that of KBr.

Simultaneous thermogravimetric and differential thermal analyses were performed on a thermal analyzer (Model DTG-50, Shimadzu, Kyoto, Japan) at a rate of 5 °C/min in a 40 ml/min flow of dried air.

The morphology of the products was observed with a scanning electron microscope (SEM), Hitachi S-2500CX.

4.3 Results and Discussion

4.3.1. XRD patterns and IR spectra of the products

The XRD patterns of the products obtained by the reaction in 1,4-BG at 300 °C are

shown in Fig. 4-1. Two types of products were detected, one for La-Dy (Group A) and the other for Ho-Yb and Y (Group B). The XRD pattern of the product obtained from lanthanum chloride hydrate essentially agreed with that reported for $La(OH)_2Cl$ (JCPDS: No. 85-0839) [7] albeit with large difference in the relative intensities. In the XRD pattern of the product from yttrium chloride hydrate (Fig. 4-1), the peaks specified by closed circles are attributed to $Y(OH)_2Cl$ (JCPDS: No. 19-1445) [8] but the other peaks could not be identified from JCPDS cards. However, when the reaction of yttrium chloride hydrate was carried out at 250 °C, only $Y(OH)_2Cl$ was formed without the contamination of the unknown phase. Therefore, the reaction of $RECl_3$ with smaller ionic size yielded a mixture of $RE(OH)_2Cl$ and an unknown compound, and the latter compound seems to be derived from $RE(OH)_2Cl$.

Rietveld refinement was carried out to identify the crystal structure of $La(OH)_2Cl$. $La(OH)_2Cl$ could not be refined with the space group, $P2/m$ [No.10], as the JCPDS card noted, but had a space group of $P2_1/m$ [No.11] (Fig. 4-2). The products from Nd, Gd, Sm and Dy chloride hydrates could also be refined with the same space group.

IR spectra of the products are shown in Fig. 4-3. Both the spectra of the products did not show characteristic bands due to the organic residue, but showed two sharp bands around 3600 cm^{-1} due to the stretching vibration modes of structural OH groups. Klevstov et al. reported that the interaction between OH group and Cl in hydroxychloride contributed to these peaks [9]. A broad band at around 3400 cm^{-1} observed in the Group B products seems to be due to the water molecules, suggesting that the unknown phase in the Group B products contained a larger amount of structural water molecules. The IR spectra of the Group B products also indicate the presence of the $RE(OH)_2Cl$ phase in the products.

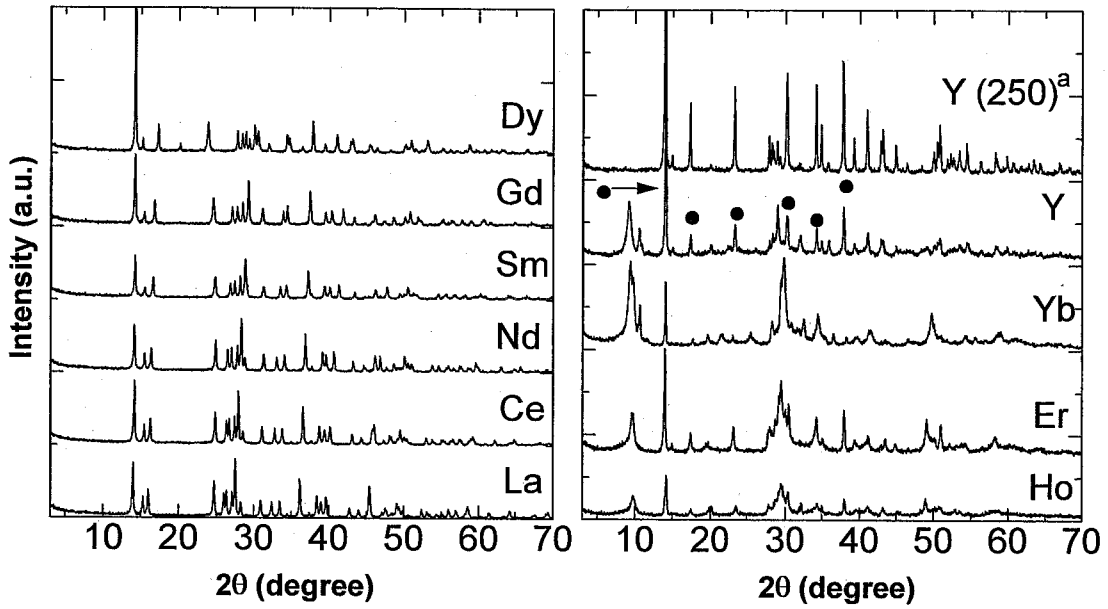

Fig. 4-1. XRD patterns of the products obtained by the reactions of RE chloride hydrates in 1,4-BG at 300 °C for 2 h. a: Product obtained at 250 °C for 2 h, ● $Y(OH)_2Cl$

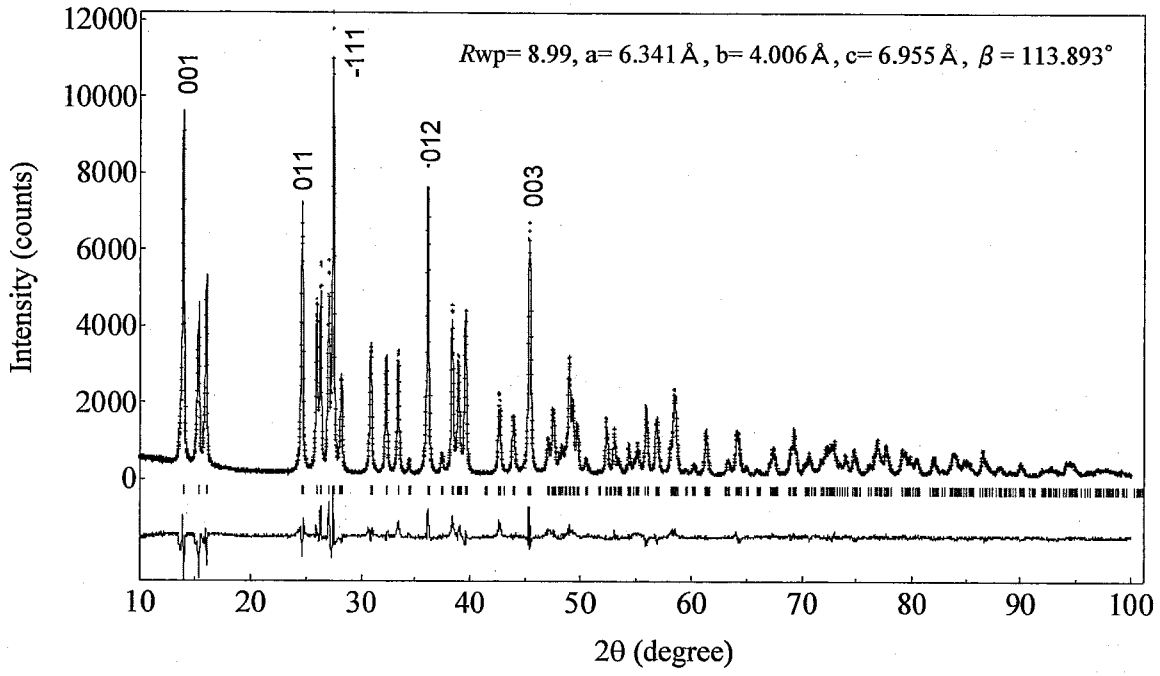

Fig. 4-2. Examined and simulated XRD patterns of $La(OH)_2Cl$.

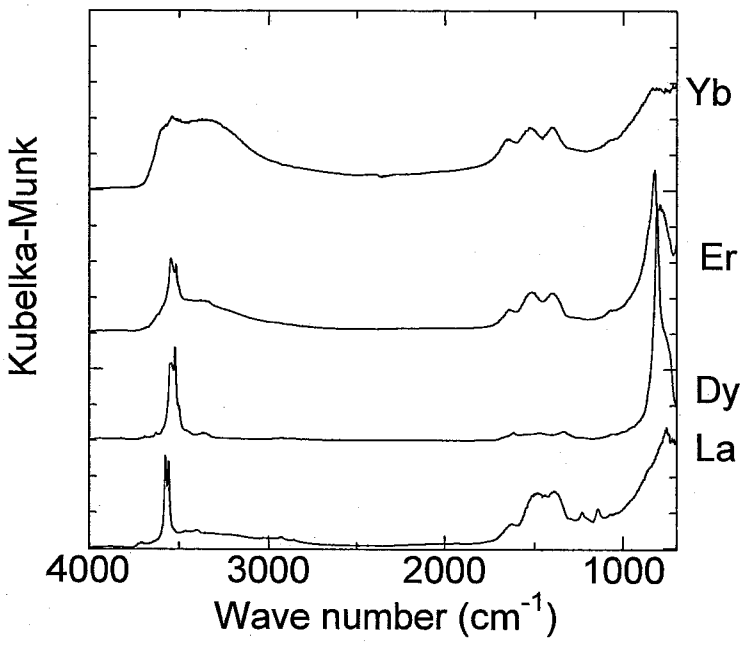

Fig. 4-3. IR spectra of the products obtained by the reactions of RE chloride hydrates in 1,4-BG at 300 ℃ for 2 h.

4.3.2. Thermal decomposition behaviour

The TG-DTA data are summarized in Table 4-1 and typical profiles are shown in Fig. 4-4. For the Group A products, a very sharp endothermic peak was observed at around 350 °C and the weight loss at this temperature range agreed with the theoretical weight loss from $RE(OH)_2Cl$ to REOCl. The XRD patterns of the products just after the weight loss were identified as REOCl (tetragonal). However, $Ce(OH)_2Cl$ was decomposed at 350 °C yielding CeO_2 without formation of CeOCl.

For the Group B products, the weight loss was observed at < 250 °C and XRD pattern of the product calcined at 200 °C was different from that of the as-synthesized product (Fig. 4-5), indicating that the water molecules are incorporated in the crystal structure of the unknown product. Therefore, it was tentatively assigned as $RE_2O_3 \cdot xH_2O$ with an unidentified crystal structure. The weight loss at the temperature range from 250 °C to 450 °C was smaller than the theoretical weight loss due to dehydration of $RE(OH)_2Cl$ to REOCl because of the contamination of the unknown compound. The contents of $RE(OH)_2Cl$ in the Group B products were estimated from the weight loss, and the results (Table 4-1) indicate that $RE(OH)_2Cl$ was the predominant phase in the Group B products. The XRD pattern of the product just after the weight loss was identified as a mixture of REOCl (hexagonal) and RE_2O_3. This result is in accord with the previous assignment of the unknown product as $RE_2O_3 \cdot xH_2O$, since all of the REOOH phases are known to be dehydrated into RE_2O_3 at the temperatures below 500 °C.

It was reported that REOCl with larger RE elements (La-Ho) exists in the tetragonal structure while REOCl with smaller RE elements (Tm-Lu) has the hexagonal structure, erbium being the crossover point [10, 11]. In the present work, however, hexagonal HoOCl and YOCl were formed (Table 4-1), in spite of the fact that the hexagonal polymorph is thermodynamically unstable for Ho and Y.

Regardless of Groups A and B, moderate weight loss was observed at 450–1000 °C

Table 4-1 Thermal analysis of the products.

Solvothermal product	Endotherm (°C)	Weight loss[a] (%)	$RE(OH)_2Cl$ Content[b] (%)	Phase after calcination at 400-450 °C[c]	Weight loss[d] (%)	Phase after calcination at 1000 °C[c, e]
$La(OH)_2Cl$	370	8.4 (8.6)[f]	-	*t*-LaOCl	0.3	LaOCl + La_2O_3 (LaOCl)
$Ce(OH)_2Cl$	—	15 (8.6)	-	CeO_2	2.5	CeO_2
$Nd(OH)_2Cl$	346	8.5 (8.4)	-	*t*-NdOCl	1.6	NdOCl + Nd_2O_3 (NdOCl)
$Sm(OH)_2Cl$	356	8.1 (8.2)	-	*t*-SmOCl	2.2	Sm_2O_3 (SmOCl+Sm_2O_3)
$Gd(OH)_2Cl$	387	8.0 (7.9)	-	*t*-GdOCl	6.2	Gd_2O_3 (GdOCl+Gd_2O_3)
$Dy(OH)_2Cl$	378	8.1 (7.8)	-	*t*-DyOCl	9.6	Dy_2O_3 (Dy_2O_3)
$Ho(OH)_2Cl$ + UKW[g]	387	6.1(7.7)	79	Ho_2O_3 + *h*-HoOCl	9.7	Ho_2O_3
$Er(OH)_2Cl$ + UKW	380	6.6 (7.6)	87	Er_2O_3 + *h*-ErOCl	10.1	Er_2O_3
$Yb(OH)_2Cl$ + UKW	389	3.9 (7.4)	53	Yb_2O_3 + *h*-YbOCl	7.4	Yb_2O_3
$Y(OH)_2Cl$ + UKW	392	10.2 (11.4)	89	Y_2O_3 + *h*-YOCl	15	Y_2O_3

a: Weight loss at the temperature range of 250-450 °C. b: Estimated from the weight loss between 250-450 °C. c: Phase identified by XRD pattern. d: Weight loss at the temperature range of 450-1000 °C. e: Phase identified after calcination of the product at 1000 °C for 30 min; the phases detected in the sample quenched just after the temperature reached 1000 °C are shown in parenthesis. f: Theoretical weight loss due to formation of REOCl from $RE(OH)_2Cl$. g: Unknown product, tentatively assigned as $RE_2O_3 \cdot xH_2O$ having an unidentified crystal structure.

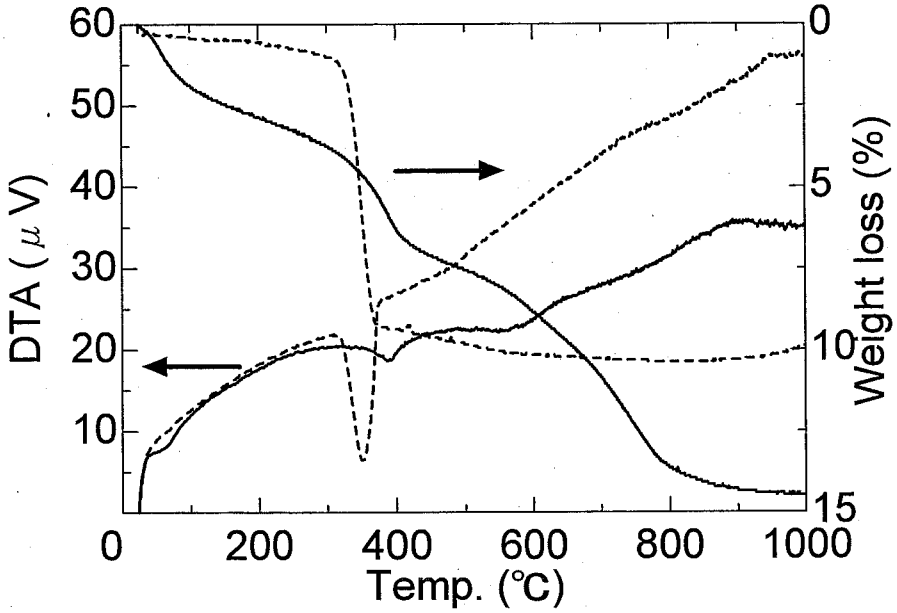

Fig. 4-4. TG-DTA profiles of the products (····, La; —, Yb).

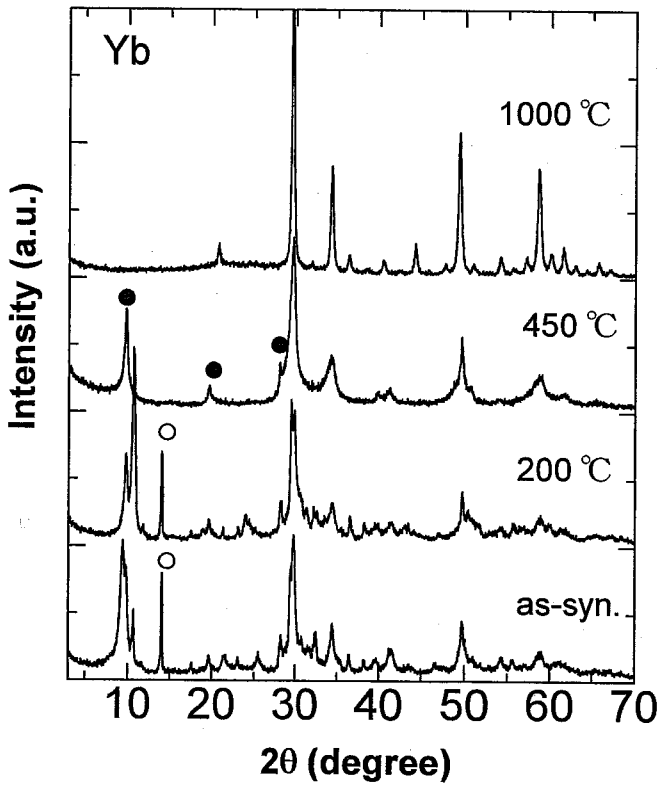

Fig. 4-5. XRD patterns of the product obtained from $YbCl_3 \cdot 6H_2O$ and samples obtained by calcination thereof at the temperature specified in the figure for 30 min:● *h*-YbOCl, ○ $Yb(OH)_2Cl$.

for the elements with smaller ionic size (<Gd), and REOCl was further decomposed into RE_2O_3. REOCl with larger ionic size was stable up to 1000 °C; however, it slowly decomposed at 1000 °C and small amounts of RE_2O_3 were detected when the products were calcined at 1000 °C for 30 min. Sokolova et al. [10] examined the thermal decomposition behavior of lanthanide chloride hydrates and reported that the temperature for the formation of REOCl had a tendency to decrease with the decrease in ionic size of RE element. They also reported that thermal stability of REOCl decreased in the same direction. These reported results suggest that chloride ions in the coordination sites of RE elements with smaller ionic size are more easily substituted with oxide anion. The present results are consistent with this tendency.

4.3.3. Reaction mechanism

Forced hydrolysis (180 °C, 120 h) of lanthanide chloride hydrate (6 mmol) in water (25 ml) was also examined using an autoclave made of teflon. No precipitates were formed, and pH of the solution was not varied by the reaction, indicating that hydrolysis of lanthanide chloride scarcely occurred at low temperatures. The morphology of the $Y(OH)_2Cl$ particles obtained by solvothermal reaction at 250 °C was completely altered from that of the starting material (Fig. 4-6), indicating that $RE(OH)_2Cl$ were formed via a dissolution-crystallization mechanism; that is, RE chlorides were dissolved into the solvent and reacted with water originated from the crystallization water of the starting materials as depicted in the following equation:

$$RECl_3 + 2H_2O \rightarrow RE(OH)_2Cl + 2HCl$$

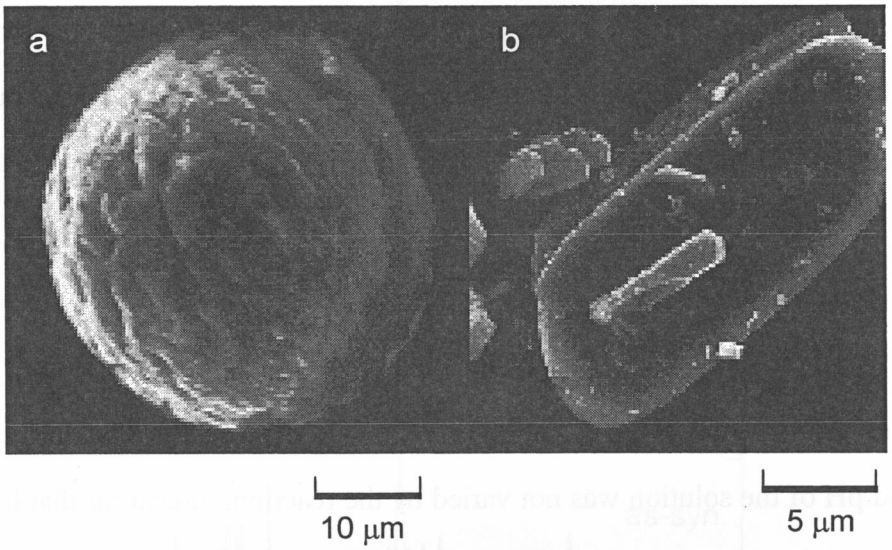

Fig. 4-6. SEM images of: (a), YCl_3 (dried at 250 ºC) and (b), $Y(OH)_2Cl$ obtained in 1,4-BG at 250 ºC.

References

[1] M. Inoue, "Solvothermal Synthesis," in Chemical Processing of Ceramics, 2nd Ed., Chap. 2, Ed. by B. Lee, S. Komarneni, Taylor & Francis, Boca Raton. FL. (2005).

[2] M. Inoue, T. Nishikawa, T. Nakamura, T. Inui, J. Am. Ceram. Soc., 80 (1997) 2157.

[3] M. Inoue, T. Nishikawa, H. Otsu, H. Kominami, T. Inui, J. Am. Ceram. Soc., 81 (1998) 1173.

[4] M. Inoue, H. Otsu, H. Kominami, T. Inui, J. Am. Ceram. Soc., 74 (1991) 1452.

[5] M. Inoue, J. Phys. Condens. Matter, 16 (2004) S1219.

[6] F. Izumi and T. Ikeda, Mater. Sci. Forum, 321-324 (2000) 198.

[7] T. N. Tarkhova, I. A. Grishin, N. N. Mironov, Russ. J. Inorg. Chem., 15 (1970) 1340.

[8] R. F. Klevtsova, P. V. Klevstov, Zhur. Strukt. Khim., 7 (1966) 556.

[9] P. V. Klevstov, V. M. Bembel', Z. A. Grankina, Zhur. Strukt. Khim., 10 (1969) 638.

[10] L. G. Sokolova, A. V. Lapitskaya, A. F. Bol'shakov, S. B. Pirkes, B. V. Abalduev, Russ. J. Inorg. Chem., 26 (1981) 936.

[11] E. Garcia, J. D. Corbett, J. E. Ford, W. J. Vary, Inorg. Chem. 24 (1985) 494.

Chapter 5

Synthesis of mesoporous needle-shaped ytterbium oxide by solvothermal treatment of ytterbium chloride

5.1 Introduction

One dimensional crystals such as carbon nanotubes have unique physical and chemical properties, suggested a wide range of their application [1]. Rare earth (RE) oxides have been used in high performance luminescent devices, magnets, catalysts and so on [2,3]. It has been reported that RE oxides with one dimensional crystals are prepared by means of template, sol-gel, and hydrothermal methods, etc [4-9].

Chapter 4 clarified that the reaction of RE chloride hydrates in 1,4-butanediol (1,4-BG) at 300 °C for 2 h in the presence of a small amounts of *n*-hexylamine (HA) and 1,6-hexanediamine (1,6-HDA) yielded phase-pure $RE(OH)_2Cl$ for La–Dy, but the products obtained from Ho–Yb and Y were mixtures of $RE_2O_3 \cdot xH_2O$ and $RE(OH)_2Cl$.

In this chapter, morphological discussion is carried out for the one dimensional crystal obtained by the solvothermal reaction of RE chlorides hydrate in the presence of amines was investigated.

5.2 Experimental procedure

5.2.1 Solvothermal treatment

Commercial RE chloride hydrates (Wako Pure Chemical Industry, Osaka, Japan) were used without further purification. Ytterbium chloride hexahydrate (9.45 g, 25 mmol) was suspended in 100 mL of 1,4-BG in a test tube serving as an autoclave liner and HA (20 mL) and 1,6-HDA (16 mL) were added to the tube (N/Cl ≈ 5). HA was added to neutralize the liberated acid in the gas phase and 1,6-HDA in the liquid phase. The test tube was placed in a 300-mL autoclave. An additional 30 mL of 1,4-BG and 10

mL of HA were placed in the gap between the autoclave wall and the test tube. The autoclave was completely purged with nitrogen, heated to 300 °C at a rate of 2.3 °C/min, and maintained at that temperature for the prescribed time. After the assembly was cooled to room temperature, the resulting product was collected by centrifugation. The product was washed with methanol and distilled water repeatedly by vigorous mixing and centrifuging, and it was then air-dried.

5.2.2 Characterization

X-ray powder diffraction (XRD, Model XD-D1, Shimadzu, Kyoto, Japan) profiles were recorded using Cu*K*α radiation and a carbon monochromator. Simultaneous thermogravimetric and differential thermal analyses (TG-DTA) were performed using a thermal analyzer (Model DTG-50, Shimadzu, Kyoto, Japan) at a rate of 5 °C/min in a 40 mL/min flow of dried air. The morphology of the products was observed with a scanning electron microscope (SEM, Model S-2500CX, Hitachi, Tokyo, Japan) or a transmission electron microscope (TEM, Model H-800, Hitachi, Tokyo, Japan), operated at 200 kV. The nitrogen adsorption isotherm was measured using a volumetric gas-sorption system (Model Autosorb-1, Quantachrome, Boynton Beach, FL).

5.3 Results and Discussion

5.3.1 Structure and morphology of the as-synthesized products

The XRD patterns of the as-synthesized products obtained by the reaction of RE (Y, Er, and Yb) chloride hydrates in 1,4-BG at 300 °C for 2 and 10 h are shown in Fig. 5-1. As shown in chapter 4, Two phases of $RE(OH)_2Cl$ and $RE_2O_3 \cdot xH_2O$ were detected in the products obtained by the reaction for 2 h. By prolonging the reaction (10 h), phase-pure $RE_2O_3 \cdot xH_2O$ was obtained for Yb, although the mixtures of $RE(OH)_2Cl$ and $RE_2O_3 \cdot xH_2O$ were still obtained for Er and Y.

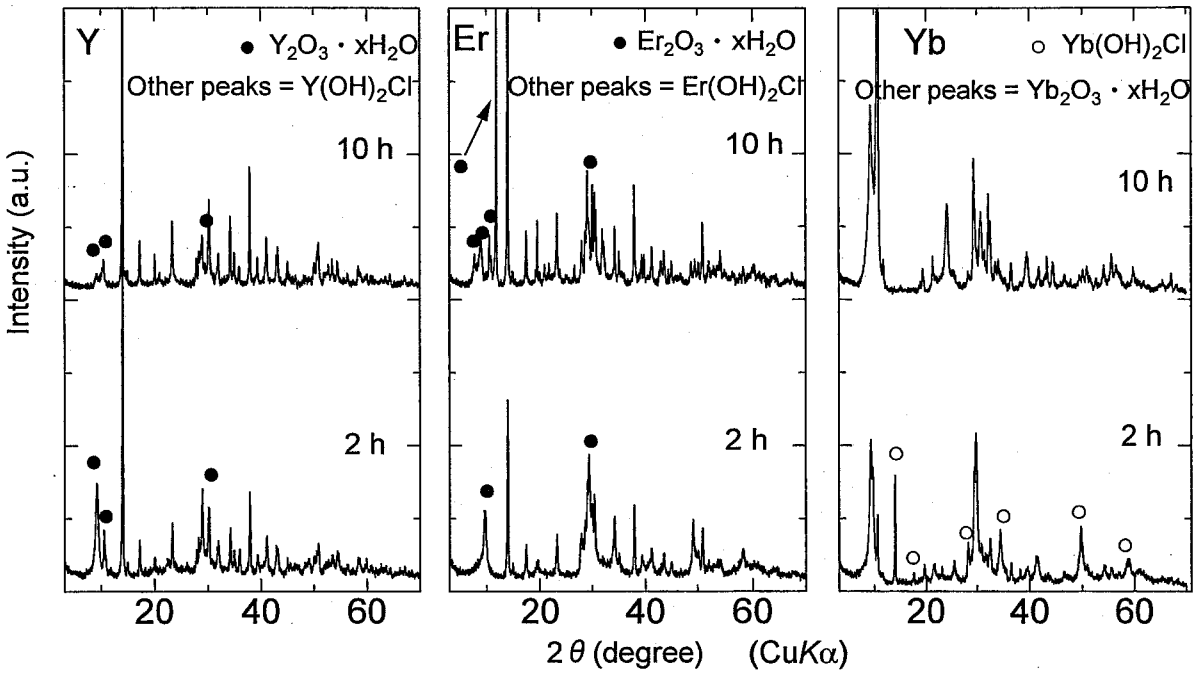

Fig. 5-1. XRD patterns of the as-synthesized products obtained by the reaction of RE (Y, Er, and Yb) chloride hydrates in 1,4-BG in the presence of HA and 1,6-HDA at 300 °C for 2 and 10 h.

The SEM images of the products obtained by the reaction in 1,4-BG for 2 h showed the formation of irregularly shaped particles (Fig. 5-2). By prolonging the reaction time, the morphology of the products for Y or Er was partly changed and needle-shaped crystals were formed; however, the majority of the products was irregularly shaped. On the other hand, the $Yb_2O_3 \cdot xH_2O$ product obtained for a prolonged reaction time (10 h) was composed of needle-shaped crystals with a width of 0.2–0.6 μm and a length of 5–15 μm.

Forced hydrolysis (180 °C, 120 h) of RE chloride hydrate (6 mmol) in water (25 mL) was also examined using an autoclave made of teflon. No precipitates were formed, and the pH of the solution was not varied by the reaction, indicating that the hydrolysis of RE chlorides barely occurred at low temperatures.

The morphology of the $RE(OH)_2Cl$ and $RE_2O_3 \cdot xH_2O$ particles obtained by the solvothermal reaction was completely altered from that of the starting material. This result indicates that $RE_2O_3 \cdot xH_2O$ was formed via a dissolution-crystallization mechanism; in other words, RE chlorides dissolved in the solvent and reacted with water originating from the crystallization water of the starting materials as depicted by the following equations:

$$RECl_3 + 2H_2O \rightarrow RE(OH)_2Cl + 2HCl$$

$$2RECl_3 + aH_2O \rightarrow RE_2O_3 \cdot (a-3)H_2O + 6HCl \ (a \geqq 3)$$

5.3.2 Effect of amines on the synthesis of the needle-shaped $Yb_2O_3 \cdot xH_2O$

Hexylamine (HA), dipropylamine (DPA), trietylamine (TEA), and 1,6-hexanediamine (1,6-HDA) were used as the amines to neutralize the liberated acid. The products obtained by the reaction of ytterbium chloride hydrates in 1,4-BG in the presence of various amines (N/Cl ≈ 5) at 300 °C for 10 h are denoted by P1(abbreviation of the amine). For example, P1(HA) means the product obtained by the reaction in 1,4-BG in

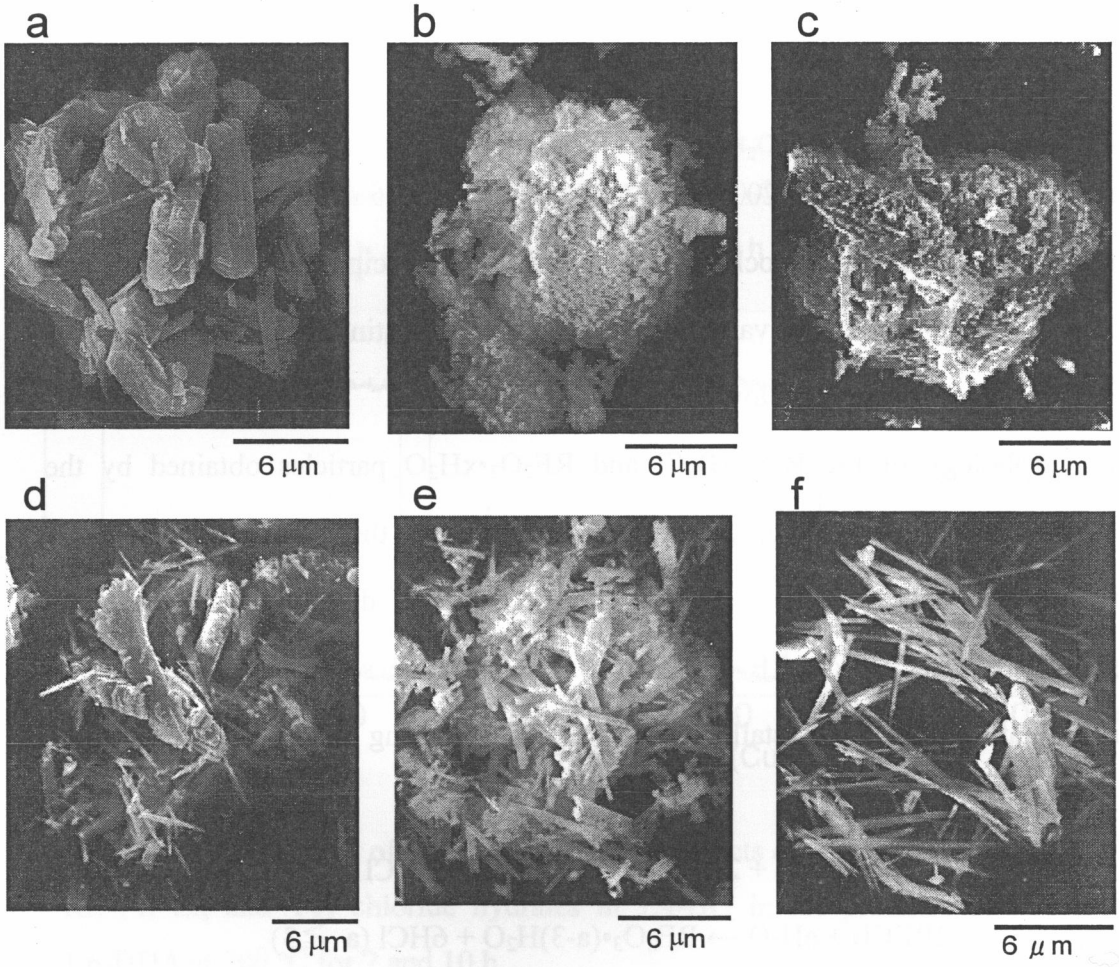

Fig. 5-2. SEM images of the products obtained by the reaction of hydrated chlorides of (a, d) Y, (b and e) Er, (c and f) Yb in 1,4-BG in the presence of HA and 1,6-HDA at 300 °C for (a, b, c) 2 h and (d, e, f) 10 h.

the presence of HA. The XRD patterns of the as-synthesized products are shown in Fig. 5-3. Phase-pure $Yb_2O_3 \cdot xH_2O$ was obtained for P1(HA), P1(1,6-HDA), and P1(HA–1,6-HDA), but P1(DPA) and P1(TEA) were mixtures of $Yb_2O_3 \cdot xH_2O$ and $Yb(OH)_2Cl$. The $Yb(OH)_2Cl$ content increased in the following order: HA < DPA < TEA. The basicity of the amines to proton increases with the number of alkyl substituents, while the basicity toward RE ions is expected to decrease because of the steric bulkiness. Therefore, the role of the amines is not only to neutralize the liberated acid but also to facilitate the transformation of $Yb(OH)_2Cl$ into $Yb_2O_3 \cdot xH_2O$ by coordination to the Yb^{3+} ions. To verify these arguments, the reaction of $YbCl_3 \cdot 6H_2O$ in the presence of tripropylamine, which was considered as a bulky amine, was examined. As expected, the product was contaminated with a fairly large amount of $Yb(OH)_2Cl$. The coordination ability of the tertiary amine to Yb^{3+} is lower than that of secondary or primary amines because of steric hindrance. In other words, $Yb_2O_3 \cdot xH_2O$ was formed with the aid of an amine having high coordinating ability.

The morphologies of P1(HA), P1(DPA), and P1(1,6-HDA) were essentially identical with that of P1(HA–1,6-HDA) (Fig. 5-4), while irregularly shaped particles were observed in P1(TEA). When HA alone was used as the solvent, i.e., the reaction was carried out without 1,4-BG, phase-pure $Yb_2O_3 \cdot xH_2O$ was obtained and the product was composed of irregularly shaped agglomerates. However, the TEM image clearly showed that small needle-shaped particles were formed even though the aspect ratio was relatively small. This result suggests that a large number of needle-shaped crystals were formed in the presence of a large quantity of HA.

5.3.3 Effect of solvent on the synthesis of the needle-shaped $Yb_2O_3 \cdot xH_2O$

1-Octanol (1-OcOH), toluene (Tol), and deionized water (H_2O) were used in place of 1,4-BG and the mixture of HA and 1,6-HDA was used to neutralize the liberated acid.

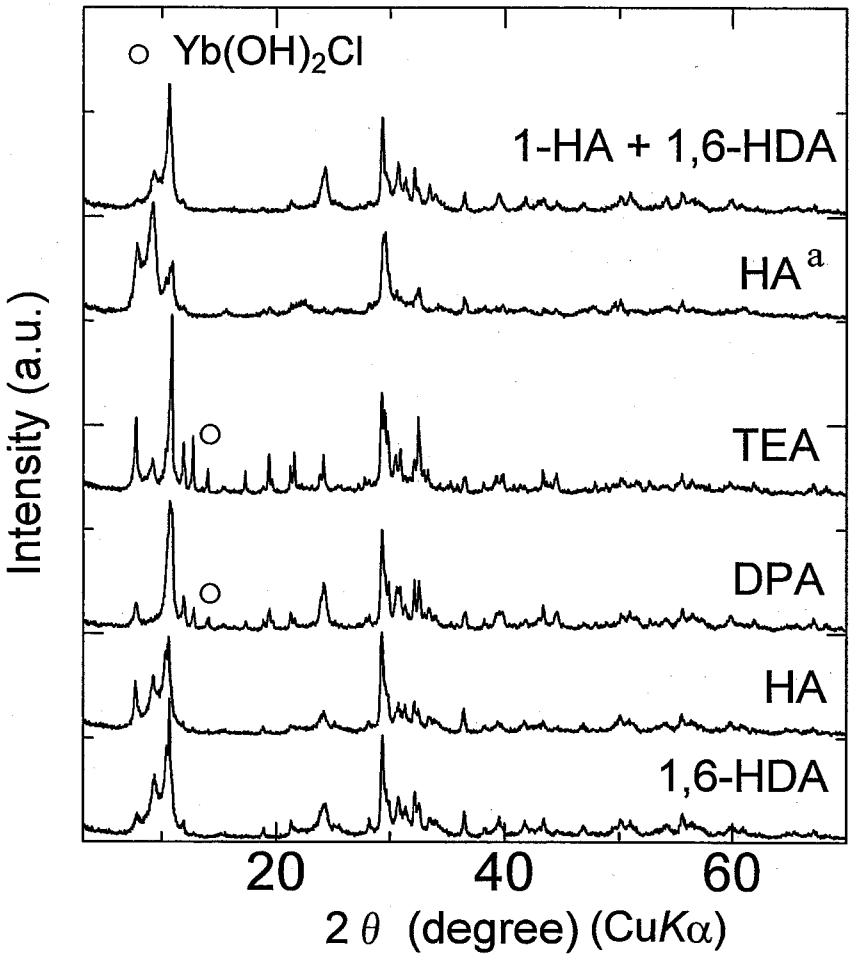

Fig. 5-3. XRD patterns of the products obtained by the reaction of ytterbium chloride hydrate in 1,4-BG in the presence of various amines (N/Cl ≈ 5) at 300 °C for 10 h.

a) HA alone was used as the medium for the solvothermal reaction.

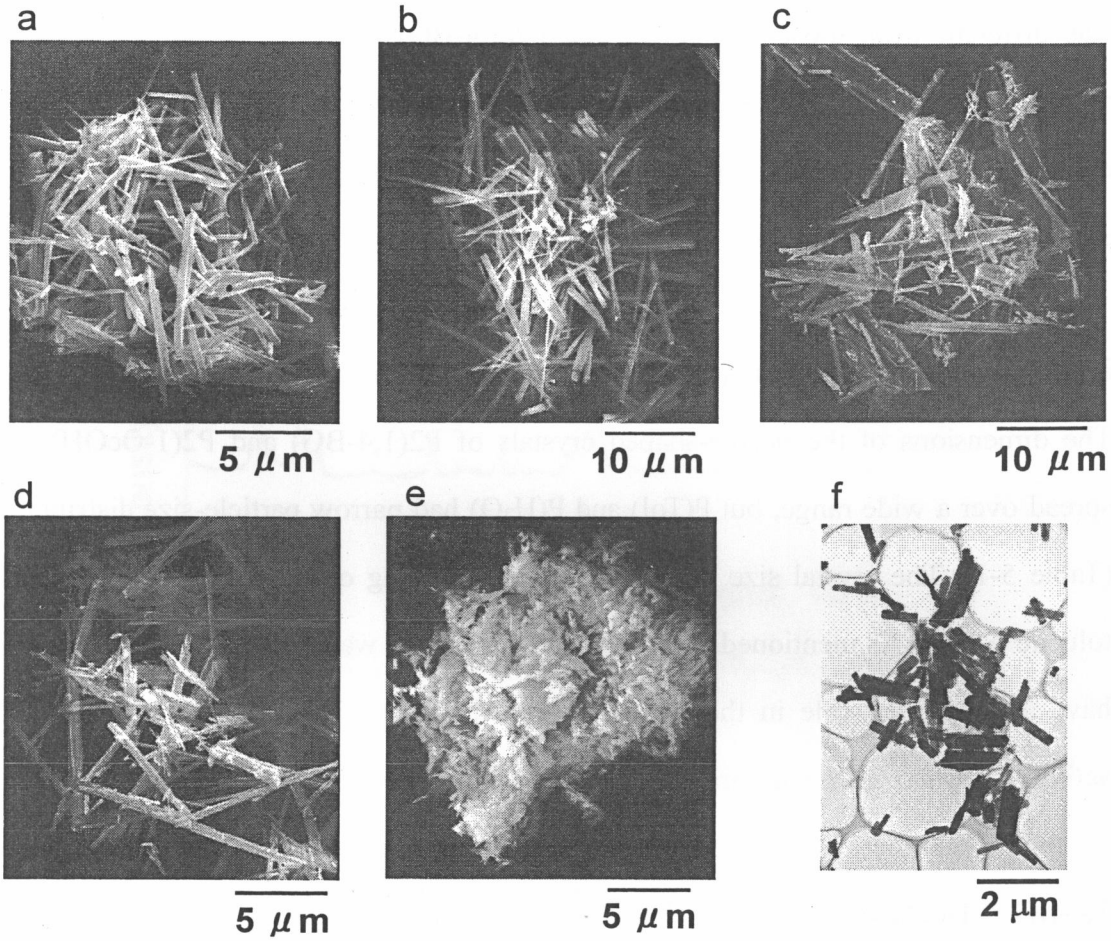

Fig. 5-4. SEM and TEM images of the products obtained by the reaction of ytterbium chloride hydrate at 300 °C for 10 h in 1,4-BG in the presence of (a) HA, (b) DPA, (c) TEA, (d) 1,6-HDA, and in (e, f) HA alone as the solvothermal medium.

These products are denoted by P2(abbreviation of the solvent). For example, P2(1,4-BG) means the product obtained by the reaction in 1,4-BG in the presence of HA and 1,6-HDA (N/Cl ≈ 5). The $Yb(OH)_2Cl$ phase was detected in P2(1-OcOH), but was not detected in P2(Tol) and P(H_2O) (Fig. 5-5). Although the XRD pattern of P(H_2O) was different from those of P2(Tol) and P2(1,4-BG), it does not coincide with the reported patterns for $Yb(OH)_3$ or YbO(OH). Therefore, the pattern was tentatively assigned as the $Yb_2O_3 \cdot xH_2O$ phase with a different degree of hydration because of the similarities in the morphology and thermal dehydration behavior (vide infra).

The morphologies of P2 are shown in Fig. 5-6. For P2(1-OcOH), a small number of irregularly shaped particles were observed because it contained the $Yb(OH)_2Cl$ phase. The dimensions of the needle-shaped crystals of P2(1,4-BG) and P2(1-OcOH) were spread over a wide range, but P(Tol) and P(H_2O) had narrow particle-size distributions (Table 5-1). The crystal size decreases in the following order: 1,4-BG > 1-octanol > toluene > H_2O. As mentioned above, the crystallization water of $YbCl_3 \cdot 6H_2O$ seems to have an important role in the crystallization of $Yb_2O_3 \cdot xH_2O$ in organic media. The activity of water in organic media increases with a decrease in the affinity of water to the media, and therefore the activity of water increases according to the following order: 1,4-BG < 1-octanol < toluene; when the same amount of water is liberated in each of these media. Therefore, smaller needle-shaped crystals were formed by the higher activity of water in organic media and the size of the crystals synthesized in H_2O was the smallest. Since a smaller crystal dimension means a higher nucleation frequency for the system where Ostwald ripening does not take place, the higher activity of water facilitates the nucleation of the crystals.

5.3.4 Thermal decomposition of needle-shaped crystals of $Yb_2O_3 \cdot xH_2O$

The thermal decomposition behavior of the needle-shaped crystals obtained in 1,4-BG

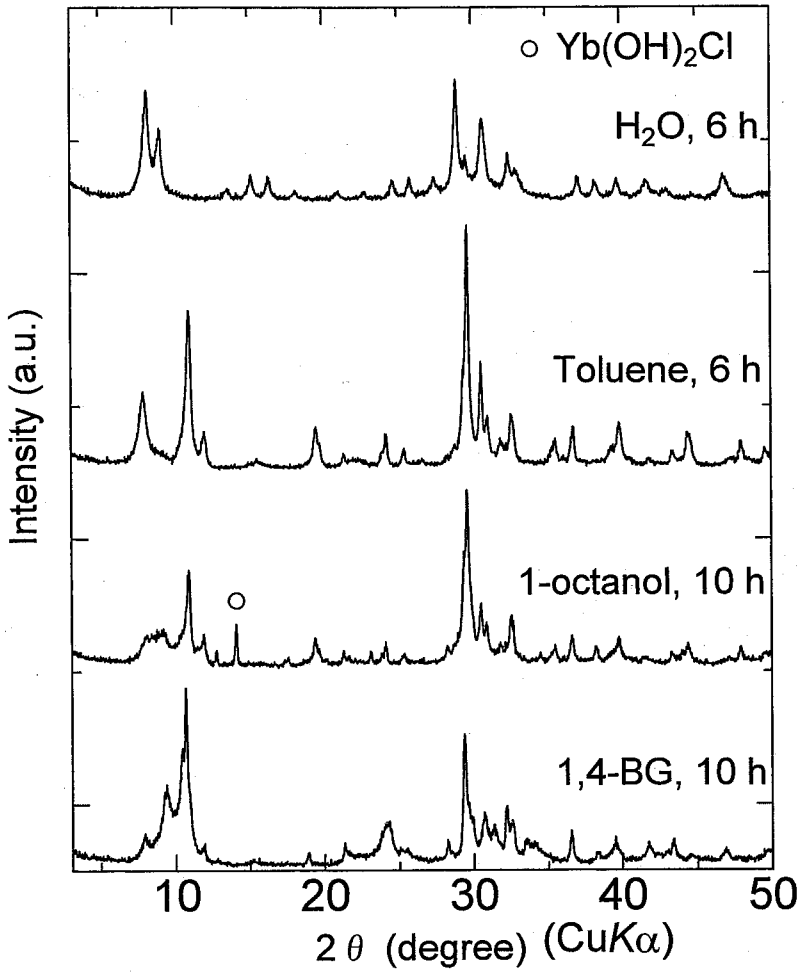

Fig. 5-5. XRD patterns of the products obtained by the reaction of ytterbium chloride hydrate in various solvents in the presence of HA and 1,6-HAD at 300 °C for the period specified in the figure.

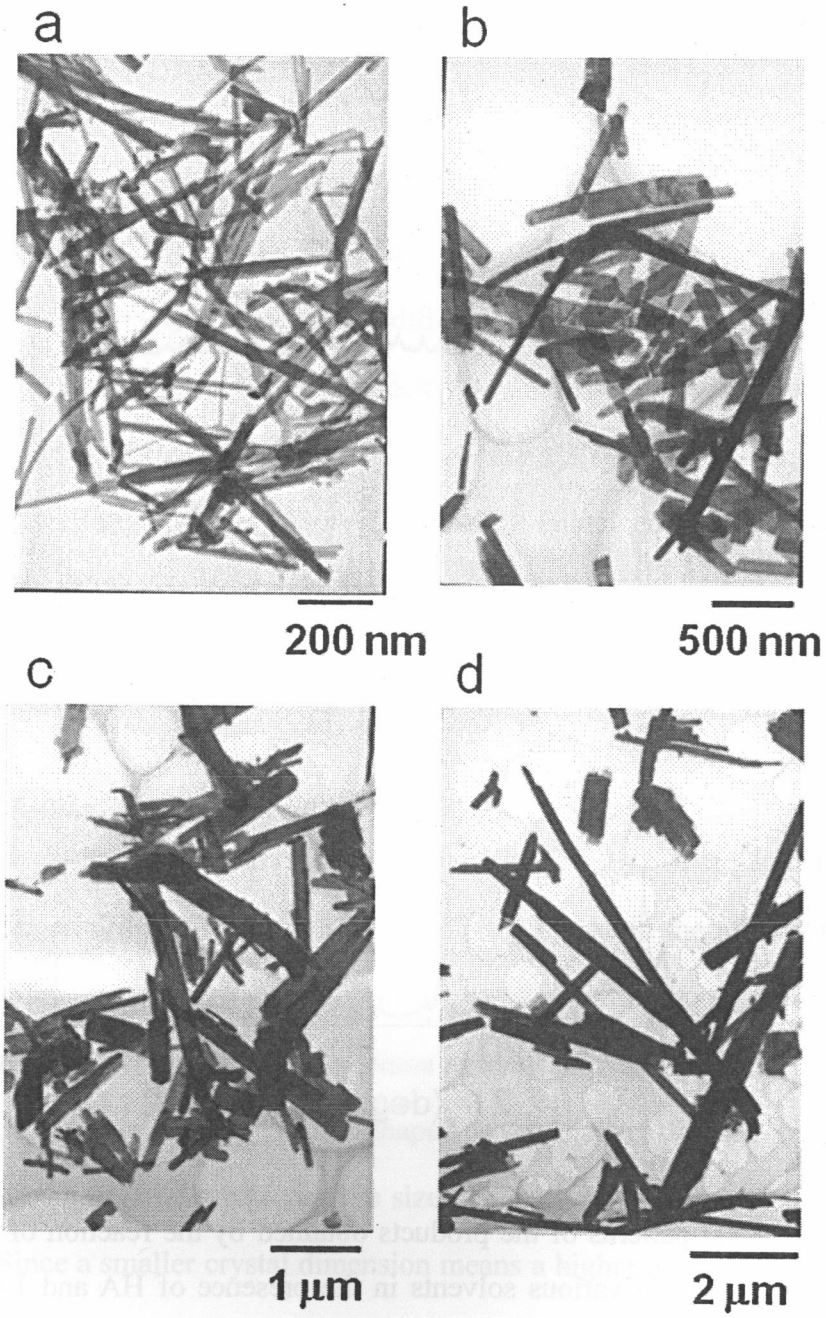

Fig. 5-6. TEM images of the as-synthesized products obtained by reaction of ytterbium chloride hydrate in (a) H_2O, (b) toluene, (c) 1-octanol, (d) 1,4-BG, in the presence of HA and 1,6-HAD at 300 °C for 6 and 10 h.

Table5-1 Dimension of the Needle-shaped $Yb_2O_3 \cdot xH_2O$

Solvent	Width (nm)	Length (mm)
1,4-BG	200-600	5-15
1-Octanol	100-300	0.5-2.5
Toluene	80-200	0.5-1.0
H_2O	15-30	0.2-0.6

in the presence of HA and 1,6-HDA was investigated by using the TG-DTA and XRD patterns of the products calcined at various temperatures. The TG profile of the needle-shaped $Yb_2O_3 \cdot xH_2O$ exhibited a weight loss at 350–500 °C, which is associated with an endothermic peak in DTA, and another weight loss was observed at around 700 °C (Fig. 5-7). The XRD patterns of the sample calcined at 500 °C indicated the formation of Yb_2O_3 (Fig. 5-8), suggesting that the weight loss at 350–500 °C is due to the dehydration of $Yb_2O_3 \cdot xH_2O$. Since the decrease in weight at around 700 °C was not accompanied by a change in the XRD pattern, the exhaust gas generated during calcination was analyzed as follows: $Yb_2O_3 \cdot xH_2O$ was heated in a 20% O_2/He flow at a rate of 10°C/min and the exhaust gas was bubbled in a 0.1 N-$AgNO_3$ solution. The clear solution of $AgNO_3$ turned turbid at 800 °C. Since the solution was not turned turbid by the bubbling of pure CO_2 gas, the particles in the turbid solution were not Ag_2CO_3 but AgCl. Therefore, the weight loss at around 700 °C is attributed to the desorption of hydrogen chloride from the surface of the Yb_2O_3 particles.

The SEM images of the samples calcined at various temperatures revealed that the needle shape of the crystals was maintained even after calcination at 1100 °C (Fig. 5-9). The TEM images of the samples (Fig. 5-9) showed that the as-synthesized products obtained in 1,4-BG were needle-shaped. Selected area electron diffraction (SAED) clearly revealed that each needle-shaped particle of $Yb_2O_3 \cdot xH_2O$ was a single crystal. The contrast in the TEM image of the sample calcined at 500 °C indicated that the needle-shaped crystals had very small voids and that calcination at 800 and 1100 °C enlarged these voids. These voids appear to be formed by the dehydration of $Yb_2O_3 \cdot xH_2O$ and were enlarged by calcination at higher temperatures. It is interesting to note that the SAED analysis clearly showed that the essentially single-crystalline nature of the needle-shaped particle was preserved even after transformation to Yb_2O_3, although each diffraction spot of Yb_2O_3 was composed of several subspots. It is to be

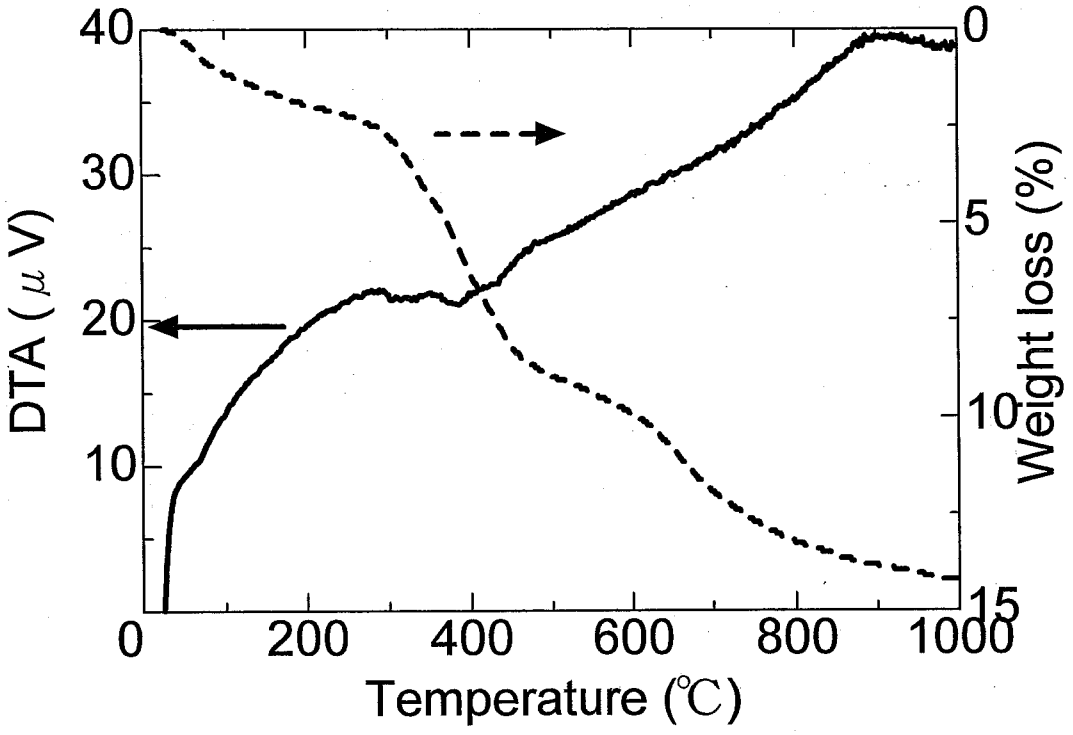

Fig. 5-7. TG-DTA profiles of $Yb_2O_3 \cdot xH_2O$ (needle-shaped crystals) obtained by the reaction of $YbCl_3 \cdot 6H_2O$ in 1,4-BG in the presence of HA and 1,6-HDA at 300 ℃ for 10 h.

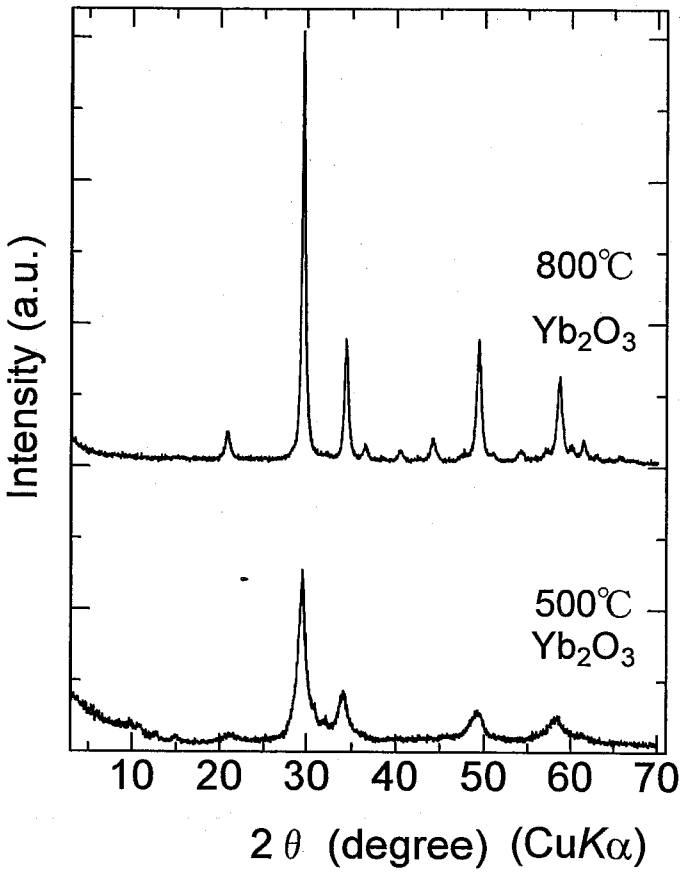

Fig. 5-8. XRD patterns of the samples obtained by calcination of the $Yb_2O_3 \cdot xH_2O$ product at the temperature specified in the figure for 30 min.
Solvothermal conditions were described in the caption of Fig.1.

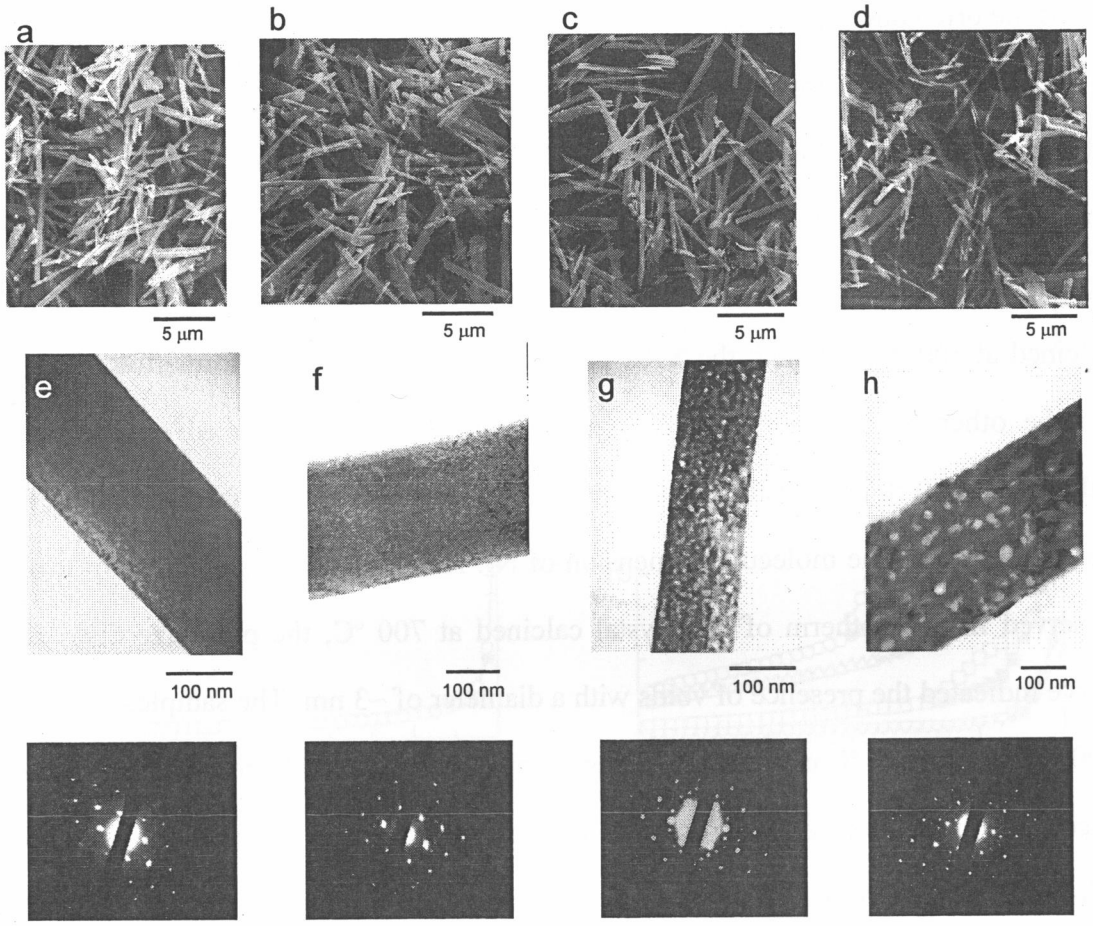

Fig. 5-9. (a, b, c, d) SEM and (e, f, g, h) TEM images of (a, e) the as-synthesized $Yb_2O_3 \cdot xH_2O$ crystals obtained by the reaction of $YbCl_3 \cdot 6H_2O$ in 1,4-BG in the presence of HA and 1,6-HDA at 300 °C for 10 h; and samples obtained by calcination thereafter at (b, f) 500 °C, (c, g) 800 °C, and (d, h) 1100 °C.

noted that these SAED patterns were not obtained by using a converged beam, but with the image of the major part of a needle-shaped crystal in a selected area aperture. This result can be explained by topotactic transformation from $Yb_2O_3 \cdot xH_2O$ to Yb_2O_3 that aligns the orientation of crystallites of Yb_2O_3 in exactly the same direction.

The voids in the samples calcined at various temperatures were assessed by the N_2 adsorption technique. Figures 5-10 and 5-11, respectively, show the isotherms and pore size distributions calculated by the BJH method from the desorption branch of the isotherms. Nitrogen was hardly adsorbed in the region with low P/P_0 for the sample calcined at 500 °C, although the XRD pattern clearly indicates the formation of Yb_2O_3. On the other hand, fairly large amounts of nitrogen were adsorbed on the sample calcined at 600 °C, suggesting that the needle-shaped crystals calcined at 600 °C have pores larger than the molecular dimension of N_2. Although the hysteresis loop was not observed in the isotherm of the crystal calcined at 700 °C, the pore size distribution curve indicated the presence of voids with a diameter of ~3 nm. The samples calcined at 800, 900, and 1000 °C exhibited hysteresis loops, which were identified as E-type loops according to the de Boer classification. The E-type hysteresis indicates the presence of ink-bottle-shaped voids. The hysteresis loop shifted to a region of higher P/P_0, which agrees with the enlargement of the pore size from 3 to 10 nm for a higher calcination temperature. The pore volume at larger diameters (> 10 nm) can be attributed to the space between the needle-shaped particles, and the distribution curve at larger pore diameters was hardly altered by the calcination. This result agrees with that obtained by the SEM observations, i.e., the morphology of the particles was not altered by calcination. The hysteresis loop was not observed for the sample calcined at 1100 °C, and the sample exhibited both the adsorption isotherm and pore size distribution curve essentially identical with those observed for the sample calcined at 500 °C. These results indicate that the pore system disappeared by calcination at higher temperature.

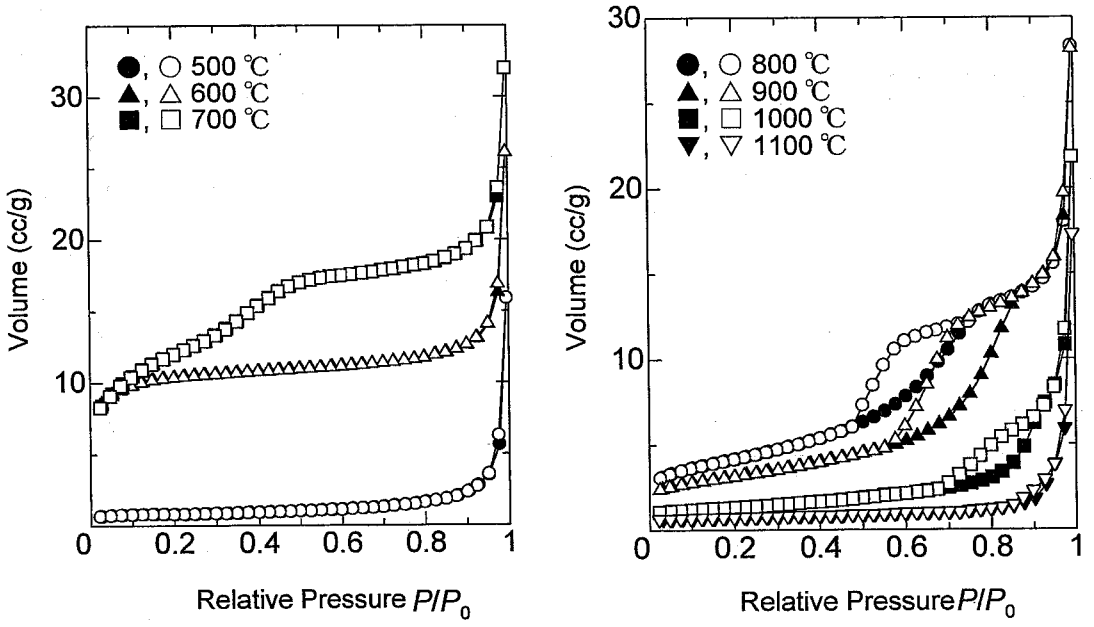

Fig. 5-10. N_2 adsorption isotherm of the samples obtained by calcination of $Yb_2O_3 \cdot xH_2O$ at various temperatures; closed symbols represent adsorption, while open symbols denote desorption.

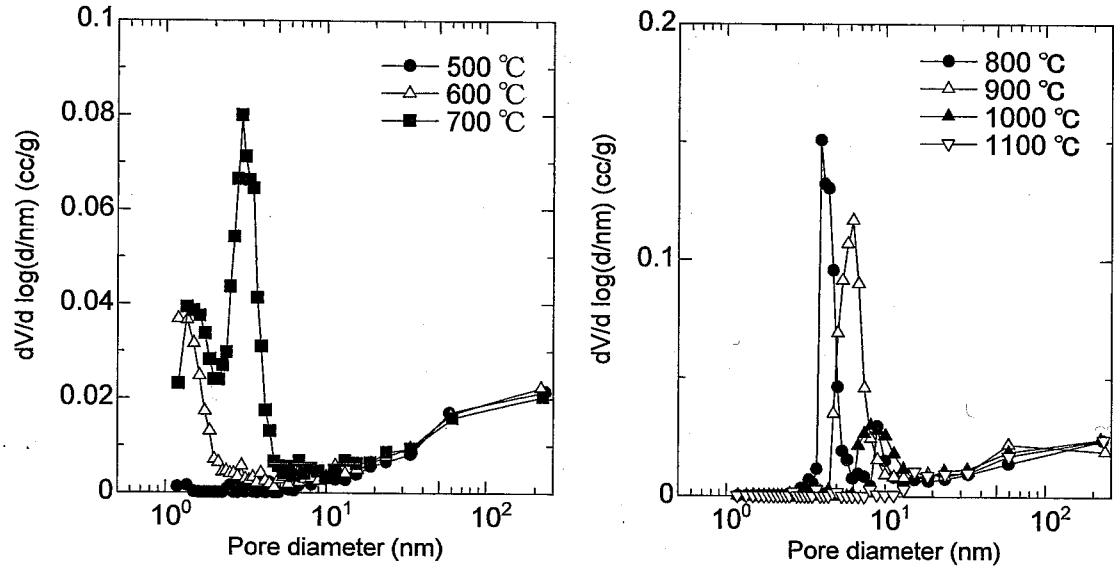

Fig. 5-11. Pore-size distribution calculated by the BJH method from the desorption branch of the N_2 adsorption isotherm for the samples obtained by calcination of $Yb_2O_3 \cdot xH_2O$ at various temperatures.

Figure 5-12 shows the BET surface area and the crystallite size of the samples calcined at various temperatures. The surface area drastically increased by calcination at 600 °C and the sample calcined at 700 °C had the highest BET surface area of 41 m^2/g. Calcination at higher temperatures resulted in a gradual decrease in the surface area, and the BET surface area of the sample calcined at 1100 °C was essentially identical with that calcined at 500 °C (2 m^2/g). On the other hand, the crystallite size gradually increased by calcination at higher temperatures and the crystallite size of the sample calcined at 1100 °C was ~61 nm.

The sample obtained by calcination at 500 °C exhibited an XRD pattern resulting from Yb_2O_3, but the dimension of the needle-shaped particles was not altered by the calcination. Therefore, the particle must have voids because of the difference in true densities between the $Yb_2O_3 \cdot xH_2O$ phase and the Yb_2O_3 phase. Since these voids were not detected by the N_2 adsorption method, they were closed or were smaller than the molecular dimension of N_2. Calcination of the product at higher temperatures enlarged the crystallite size of Yb_2O_3, which was accompanied by the enlargement of intraparticle pores. The enlargement of the BET surface area from 2 m^2/g for the sample calcined at 500 °C to 32 m^2/g for the sample calcined at 600 °C suggests that intraparticle pores having a size larger than the molecular size of N_2 were formed by the calcination above 600 °C.

Figure 5-13 shows the TEM images of the needle-shaped Yb_2O_3 crystals obtained by the solvothermal reaction in toluene or H_2O in the presence of HA and 1,6-HDA and the subsequent calcination at 800 °C. The voids formed by the dehydration of $Yb_2O_3 \cdot xH_2O$ were observed in each crystal.

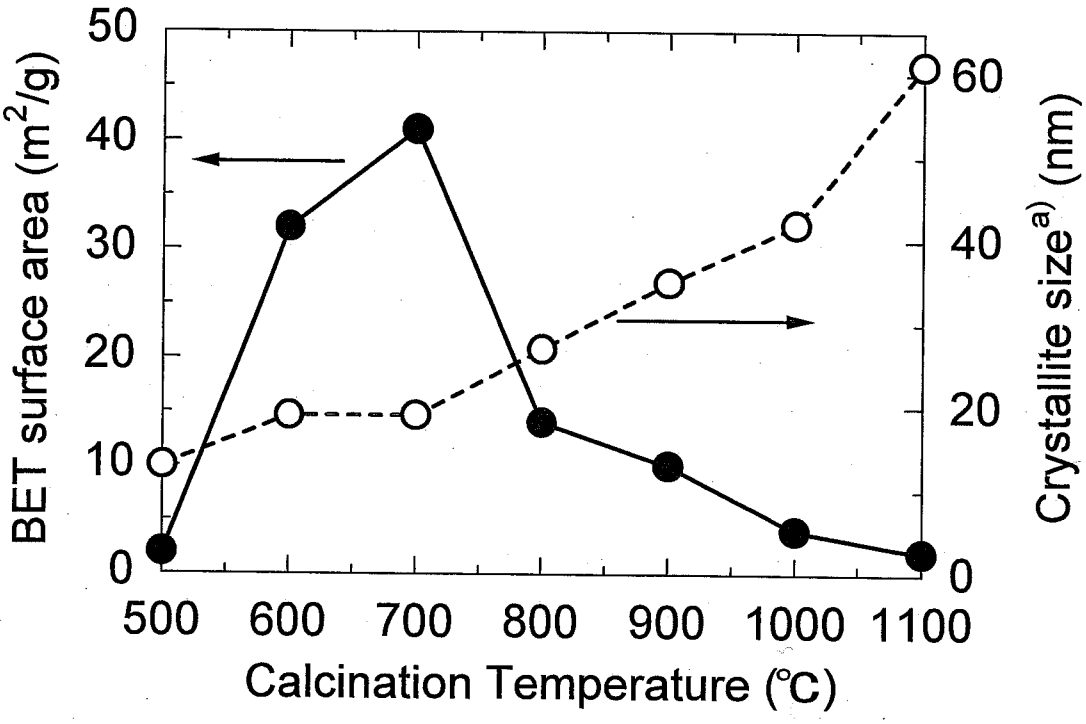

Fig. 5-12. BET surface area and the crystallite size of the samples obtained by calcination of $Yb_2O_3 \cdot xH_2O$ at various temperatures. $Yb_2O_3 \cdot xH_2O$ was prepared by the reaction of $YbCl_3 \cdot 6H_2O$ in the presence of HA and 1,6-HAD at 300 °C for 10 h.

[a] Crystalline size calculated from the half-height width of the 222 diffraction peak (29.6° 2θ) by using the Scherrer equation.

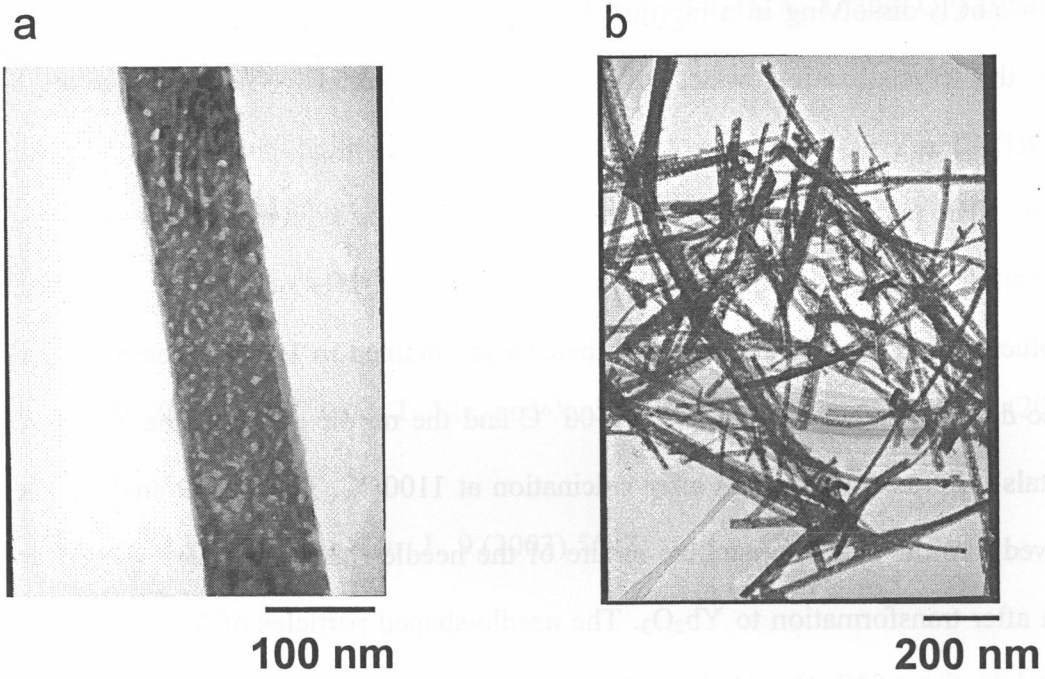

Fig. 5-13. TEM images of needle-shaped Yb_2O_3 crystals obtained by the solvothermal reaction in (a) toluene and (b) H_2O in the presence of HA and 1,6-HDA at 300 °C for 6 h and subsequent calcination at 800 °C.

5.4 Conclusions

The irregularly shaped large crystals of $Yb(OH)_2Cl$ were formed by the solvothermal reaction of $YbCl_3 \cdot 6H_2O$ in 1,4-BG in the presence of HA and 1,6-HAD at 300 °C for 2 h, while the needle-shaped crystals of $Yb_2O_3 \cdot xH_2O$ were obtained by a prolonged reaction (10 h). These products were formed via a dissolution-crystallization mechanism in which $YbCl_3$ dissolving in a mixture of organic solvents and water, which originated from the crystallization water of the starting materials. The transformation of $Yb(OH)_2Cl$ to $Yb_2O_3 \cdot xH_2O$ was facilitated by amines having higher coordination ability to Yb^{3+}. The particle size of $Yb_2O_3 \cdot xH_2O$ decreased due to higher activity of water in the organic media; the needle-shaped crystals of $Yb_2O_3 \cdot xH_2O$ obtained by the reaction in toluene were considerably smaller than those obtained in 1,4-BG. The $Yb_2O_3 \cdot xH_2O$ phase decomposed to Yb_2O_3 at 350–500 °C and the needle shape of the $Yb_2O_3 \cdot xH_2O$ crystals was maintained even after calcination at 1100 °C. The SAED analysis clearly showed that the single-crystalline nature of the needle-shaped particles was preserved even after transformation to Yb_2O_3. The needle-shaped particles of Yb_2O_3 obtained by the calcination of $Yb_2O_3 \cdot xH_2O$ at 600 °C had a micropore system and the pore size was enlarged by the calcination. Finally, the pore size was enlarged beyond detection by the N_2 adsorption method by calcination at 1100 °C.

References

[1] C. Liu and Y. Y. Fan, Science, 286 [5442] (1999) 1127.

[2] G. Adachi and N. Imanaka, Chem. Rev., 98 (1998) 1479.

[3] S. Hosokawa, H. Kanai, K. Utani, Y. Taniguchi, Y. Saito, and S. Imamura, Appl. Catal. A: General, 45 (2003) 181.

[4] Y. P. Fang, A. W. Xu, L. P. You, R. Q. Song, J. C. Yu, H. X. Zhang, Q. Li, and H. Q. Liu, Adv. Funct. Mater., 13 (2003) 955.

[5] Y. C. Cao, J. Am. Chem. Soc., 126 (2004) 7456.

[6] Y. Murata and M. Adachi, Chem. Lett., 33 (2004) 488.

[7] M. Yada, M. Mihara, S. Mouri, M. Kuroki, and T. Kijima, Adv. Mater., 14 (2002) 309.

[8] G. Wu, L. Zhang, B. Cheng, T. Xie, and X. Yuan, J. Am. Chem. Soc., 126 (2004) 5976.

[9] X. Wang and Y. Li, Chem. Eur. J., 9 (2003) 5627.

Chapter 6

Synthesis of rare earth borate ($REBO_3$) by glycothermal method

6.1 Introduction

A large number of luminescent materials based on rare earth (RE) ions or RE host lattices have been invented [1]. Modified RE borates with vaterite structure, in particular (Gd,Y)BO_3:Eu, represent the important material for plasma display panels. The luminescent property of phosphor materials is strongly affected by the particle size and morphology. Surface-perfect and spherical-shaped phosphors always have high packing density, good slurry property, and smooth light intensity distribution [2].

Various techniques have been developed to prepare high-quality $REBO_3$:Eu phosphors. These technique are solid-state reaction [3], coprecipitation [3,4], combustion method [5], ultrasonic spray pyrolysis [6], sol-gel technique [7,8] and sol-gel pyrolysis [9,10], and so on. Much work has been devoted on the hydrothermal synthesis of $REBO_3$, and nanoparticles of $REBO_3$ or $REBO_3$ with specific morphology were obtained by this method [2,11-15]. For example, Yan et al. prepared YBO_3:Eu nanoparticles (particle size; 20 nm) by a hydrothermal method in the presence of urea [13]. They also reported the formation of donut-like assembly of YBO_3:Eu crystals by the hydrothermal method under an alkaline condition [14]. Lin et al. have reported that YBO_3:Eu crystals with flower and hedgehog fungus-like structures were synthesized by a hydrothermal method under acidic conditions [15].

This chapter discussed the glycothermal reaction of RE acetates with trimethoxyborane in 1,4-butanediol and the morphology or crystal structure of the obtained $REBO_3$.

6.2 Experimental

Trimethoxyborane (1.29 g, 12.5 mmol) and yttrium acetate tetrahydrate (4.24g, 12.5 mmol) were suspended in 120 ml of 1,4-butanediol (1,4-BG) in a test tube, serving as autoclave linear, and the test tube was placed in a 300-ml autoclave. An additional 40 ml of 1,4-BG was placed in the gap between the autoclave wall and the test tube. The autoclave was purged with nitrogen, heated to 315 °C at a rate of 2.3 °C/min, and kept at that temperature for 2 h. After the assembly was cooled to room temperature, the resulting products were centrifuged. For calcination, the products were heated at a rate of 10 °C/min and held at a prescribed temperature for 30 min in a box furnace.

X-ray powder diffraction (XRD: Model XD-D1 Shimadzu, Kyoto, Japan) was recorded using Cu *Kα* radiation. For Rietveld analysis, the XRD pattern was measured on another diffractometer (Model Rint 2500, Rigaku, Tokyo, Japan) and analyzed by RIETAN-2000 program [16]. The morphology of the products was observed with a scanning electron microscope (SEM), Hitachi S-2500CX, and a transmission electron microscope (TEM), Hitachi H-800. Specific surface area was calculated using the BET single-point method on the basis of N_2 uptake measured at 77 K using a Micrometritics Flowsorb II 2300 sorptionmeter. Nitrogen adsorption isotherm was measured using a volumetric gas-sorption system (Model Autosorb-1, Quantachrome, USA). Simultaneous thermogravimetric and differential thermal analyses were performed on a thermal analyzer (Model DTG-50, Shimadzu, Kyoto, Japan) at a rate of 5 °C/min in a 40 ml/min flow of dried air. The particle size distribution was measured on an electrophoretic light scattering spectrometer, Osluka Electronics, ELS-800. A portion of the product (25 mg) was suspended in 250 ml of deionized water. The measurement was carried out after ultrasonic treatment of the suspension for 10 min, followed by standing for 10 min.

6.3. Results and discussion

6.3.1 Synthesis of YBO_3 by the glycothermal method

Figure 6-1 shows the XRD patterns of the as-synthesized products obtained by the reaction with various ratios of yttrium acetates to trimethoxyborane at 315 °C for 2 h. A clear solution was obtained by the reaction of trimethoxyborane alone. YBO_3 was obtained by the reaction of Y/B = 1 and 1/3. Y(OAc)O was formed in the product with Y/B = 3/1, but the phase due to boron species was not detected [17]. The yield of YBO_3 was almost 100 % for the reaction with Y/B = 1 but was low for the reaction with Y/B of 1/3. Another yttrium borate phase, Y_3BO_6, has been reported [18,19], but only YBO_3 was obtained in the glycothermal reaction of yttrium acetate and trimethoxyborane.

Figure 6-2 and Table 6-1 show the results for Rietveld analysis of the as-synthesized YBO_3 product obtained by the reaction of yttrium acetate and trimethoxyborane with Y/B = 1. The refinement led to residual values of Rwp = 7.48 %, Rp = 5.49 %, Re = 2.97 % and S = 2.52. The space group of YBO_3 was $P6_3/m$ [20]. The unit cell parameters of a and c axes were 3.796 and 8.815 Å, respectively, which were slightly larger than the reported values (a, 3.776 Å; b, 8.806 Å) [20]. Enlargement of unit cell is usually observed for the glycothermal products and is attributed to the alkoxyl (or hydroxyl) groups anchored on the surface of the product particles.

The as-synthesized YBO_3 was composed of spheroidal particles with hexagonal-pyramidal craters at the both sides of the particles. The largest diameter was 1 μm (Fig. 6-3), which was distributed in a extremely narrow range, and agglomerates were not observed, indicating mono-dispersed particles were formed. The particle size distribution was also assessed by the dynamic light scattering method (Fig. 6-4). The particle size was distributed in a range of 0.4 - 1.0 μm, slightly smaller than that observed by SEM, which is, however, reasonable because the product particles were not truly spherical. The distribution curve also indicates that the product particles were well

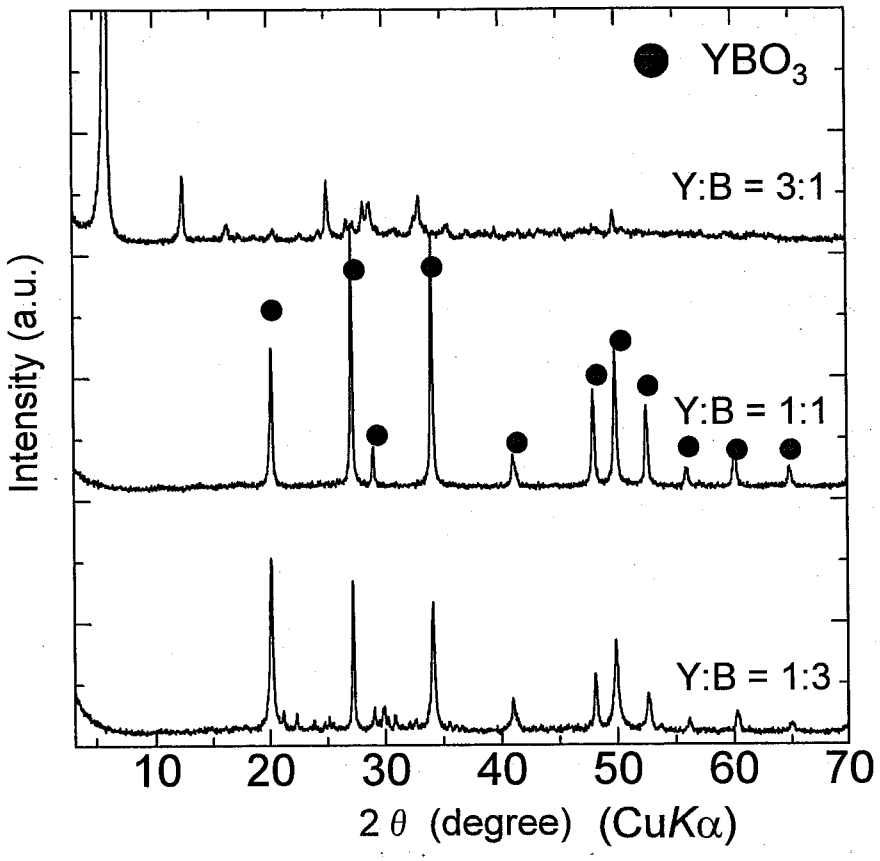

Fig. 6-1. XRD patterns of the products as-synthesized by the glycothermal reaction of yttrium acetates and trimethoxyborane with various ratios in 1,4-BG at 315 °C for 2 h.

Table 6-1 Crystallographic data of YBO_3 obtained by glycothermal method

Element	Site	g[a)]	x	y	z	B[b)]
Oa	4f	1	0.667	0.333	0.104	1.0
Ob	6h	1/3	0.783	-0.132	0.250	1.0
B	6h	1/3	0.593	0.438	0.250	1.0
Y	2b	1	0	0	0	0.5

Space group $P6_3/m$ (No. 176).

a) Site Occupacy.

b) Isotropic displacement parameter.

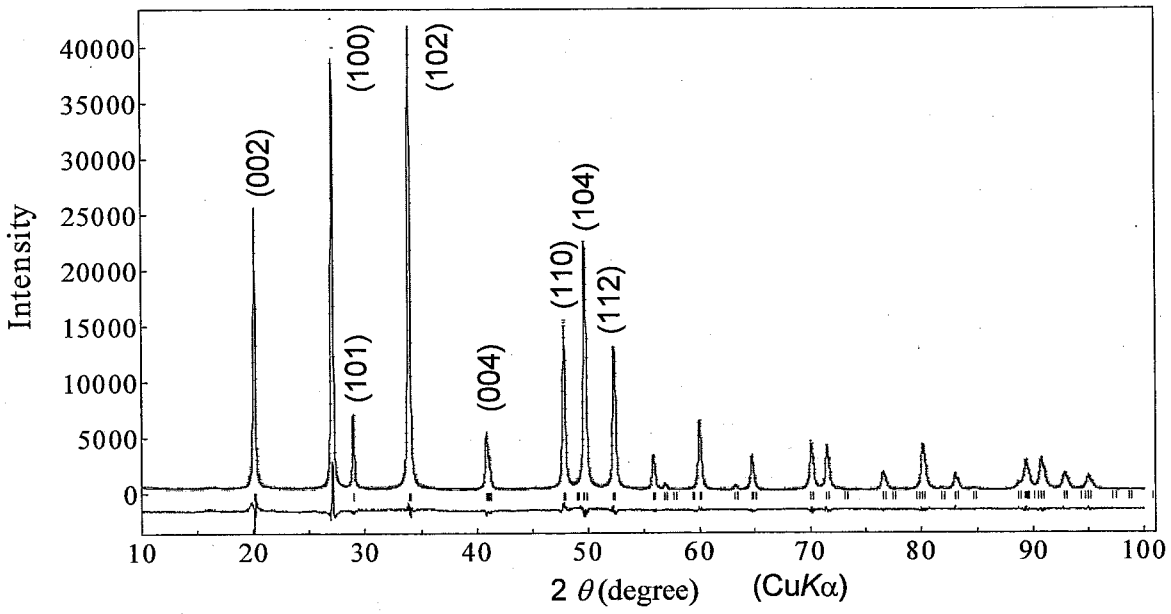

Fig. 6-2. Observed, calculated, and difference patterns obtained by Rietveld analysis of YBO_3 as synthesized by glycothermal method at 315 °C for 2 h.

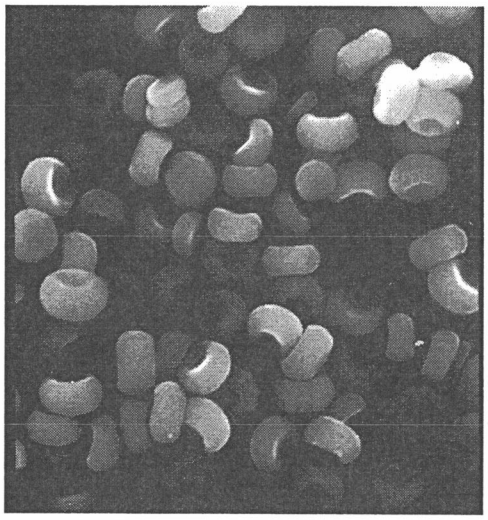

Fig. 6-3. SEM image of YBO_3 as synthesized by glycothermal reaction of yttrium acetate and trimethoxyborane at 315 °C for 2 h.

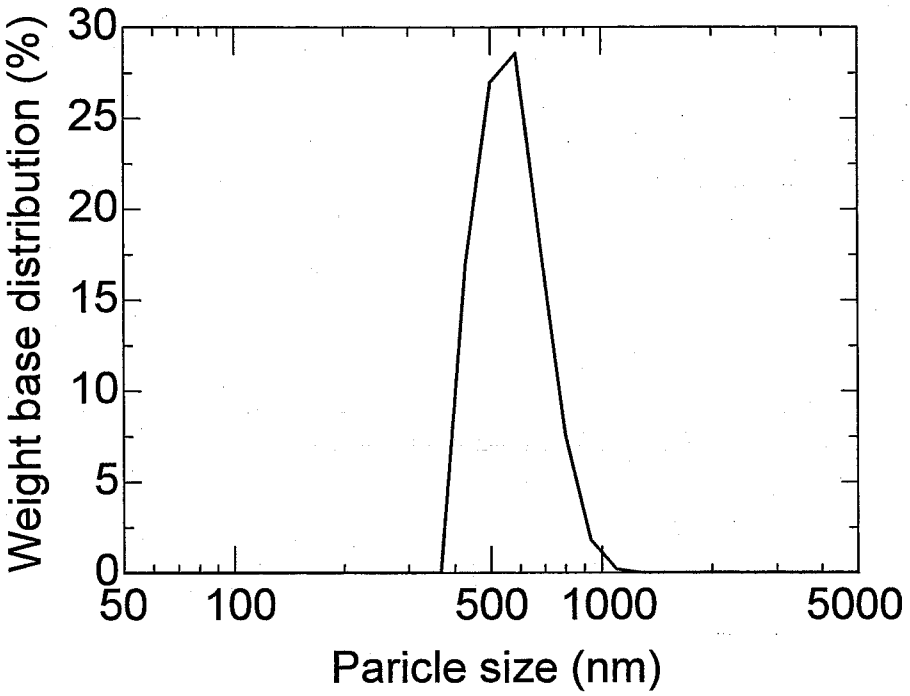

Fig. 6-4. Particle size distribution of as-synthesized YBO_3 measured by dynamic light scattering method.

dispersed and free from agglomerates.

The TEM images of the as-synthesized YBO_3 particles are shown in Fig. 6-5. As shown in Figs. 6-5a and 6-5b, the crushed particles were frequently observed. All of them appeared to have originally been from the spheroidal particles, which were crushed through the center of the spheroid while preparing specimens for TEM observation. Detailed examination of the TEM images of the crushed particles indicated that the particles contained a number of deep crevices, which can explain the reason why the spheroidal particles easily break down. The selected area electron diffraction of a whole particle exhibited a single crystal pattern with the c axis of the YBO_3 crystal parallel to the electron beam. These results suggest that each particle was grown from one nucleus, but was divided into smaller crystallites by the crevices. Figure 6-5d shows a high magnification image of the edge of the YBO_3 crystals whose ab planes are parallel to the electron beam. Thin plates of the YBO_3 crystals were preferentially grown along with the ab plane and stacking of the plates formed the spheroidal particles. However, the plates were not parallel but with slight angles, resulting in formation of the spheroidal particle with the crater as shown in the SEM image. Detailed mechanisms for the formation of the unique morphology of the product particles will be discussed in a separate paper.

Differential thermal analysis (DTA) of the as-synthesized YBO_3 product obtained by the reaction at 315 °C showed a slight exotherm at around 350 °C, which was associated with about 2.0 % weight decrease between 200 and 400 °C (Fig. 6-6). This weight decrease is due to the combustion of the organic residue remaining on the product particles. No sharp peak due to the crystallization of the amorphous phase was observed in DTA up to 1200 °C, but a weight loss was detected between 1100 and 1200 °C. The XRD pattern of the product calcined at 1100 °C exhibited low intensity peaks at 22.0, 32.8 and 31.1°, which are presumably due to Y_3BO_6 [18,19]. This result indicates that

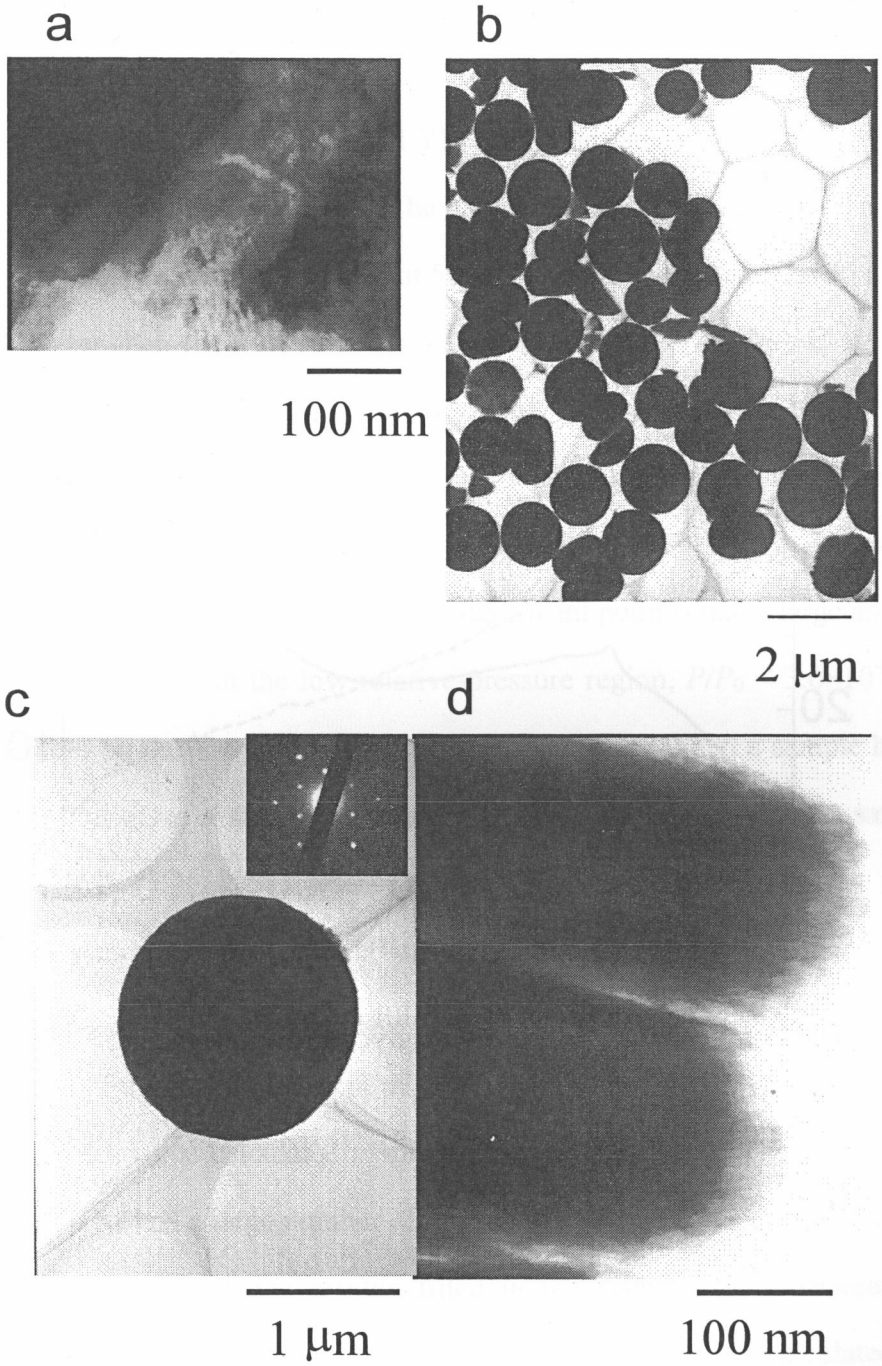

Fig. 6-5. TEM images of YBO_3 as synthesized by glycothermal method at 315 °C for 2 h.

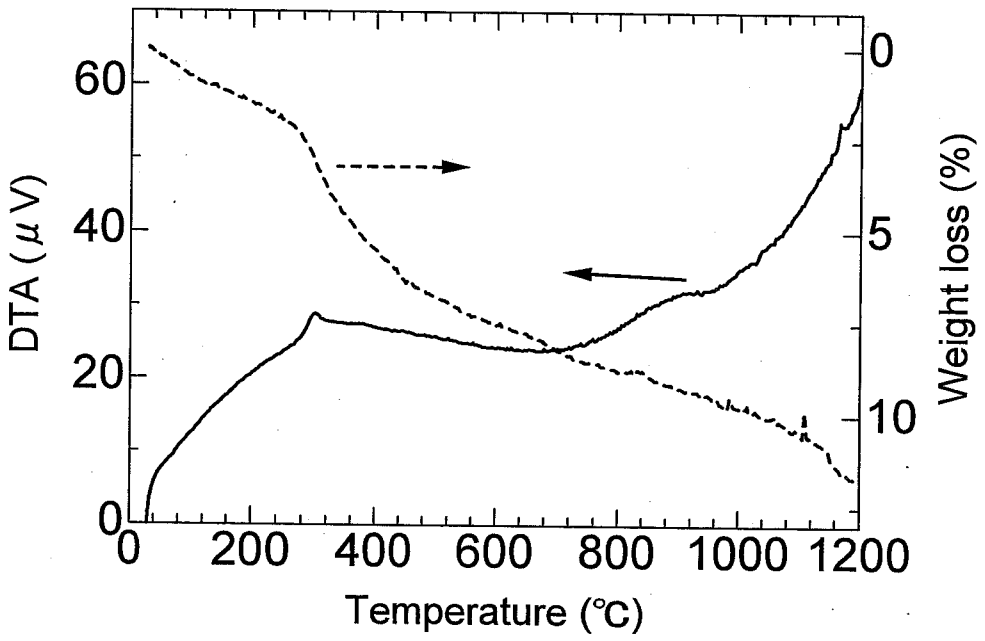

Fig. 6-6. TG-DTA of YBO_3 as synthesized by glycothermal method at 315 °C for 2 h.

segregation of YBO_3 into Y_3BO_6 and B_2O_3 occurred followed by evaporation of B_2O_3 since boron oxide is known as a highly volatile material with the boiling point of 1800 °C and the vapor pressure of 1.16×10^{-6} Pa at 800 °C [21].

Some properties of the as-synthesized YBO_3 and the samples obtained by calcination thereof are summarized in Table 6-2. The as-synthesized YBO_3 product had a surface area of 7 m^2/g, and the sample calcined at 500 °C had the surface area of 39 m^2/g, which was much larger than the hypothetical surface area (3 m^2/g) calculated assuming that each YBO_3 particle is spherical with a diameter of 1 μm (particle size), indicating that a pore system was developed in the particles by calcination. The N_2 adsorption isotherm of the sample calcined at 500 °C is shown in Fig. 6-7. A slight hysteresis was observed at a high relative-pressure region. The most significant point is that a large amount of N_2 molecules was adsorbed at the low relative-pressure region, $P/P_0 < 3.0\times10^{-2}$. This can be clearly seem by the V-t plot derived from the isotherm. When a sample has no pore systems, the plot gives a straight line going through the origin. When a sample has a micropore system, an abrupt decrease in the slope is observed. The V-t plot of the product clearly indicates the presence of micropores. The external surface area, that is the surface area after micropores are filled with the adsobate molecules, was calculated from the slope of the second segment of the V-t plot to be 5 m^2/g, which was essentially identical with the value calculated assuming spherical particles. Therefore, the sample calcined at 500 °C had a large number of micropores. These pores seem to be originated by the combustion of organic residue filled in the deep crevices between the plate crystals. The BET surface area drastically decreased to the value calculated assuming spherical particles by calcination at 800°C, indicating that the micropores of the sample calcined at 500 °C were closed by sintering of the crystallite.

The crystallite size of samples determined by the XRD line broadening technique was approximately the same up to 800 °C. The crystallite size was different from the particle

Table 6-2 Some properties of the as-synthesized product and the samples obtained by calcination thereof

Sample	Phase	Crystallite size (nm)			BET surface area
		(002)	(110)	(104)	(m^2/g)
as-syn.	YBO_3	49	116	74	7
500 °C	YBO_3	49	88	74	39
800 °C	YBO_3	44	88	61	3
1100 °C	YBO_3(87.5)[a)]+Y_3BO_6(12.5)	52	35	30	3

a) Mass fractions (%) of YBO_3 and Y_3BO_6 phases calculated by Rietveld analysis; the refiment led to residual values of Rwp = 7.43 %, Rp = 5.44 %, Re = 4.73 % and S = 1.57.

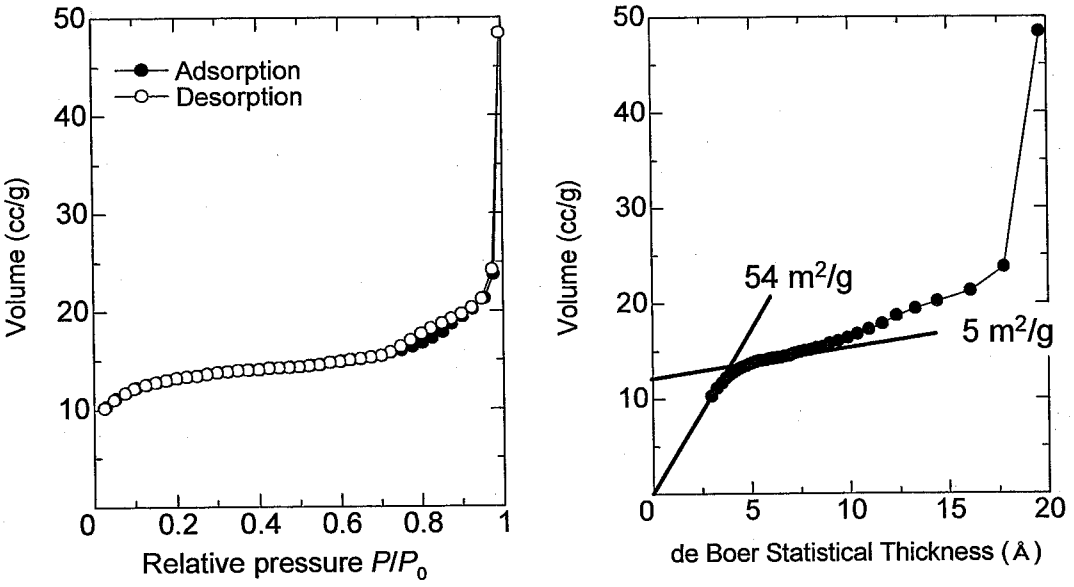

Fig. 6-7. N_2 adsorption isotherm (left) and V-t plot (right) derived from the adsorption branch of the isotherm of the sample obtained by 500 °C calcination of YBO_3.

size because of the presence of the deep crevices in the particles. However, calcination at 1100 °C drastically decrease the crystallite sizes determined with (110) and (104) planes. This result is explained by the segregation of YBO_3 into B_2O_3 and Y_3BO_6, which was facilitated by evaporation of B_2O_3.

6.3.2 Synthesis of $REBO_3$ by the glycothermal reaction

The phases formed by the reaction of RE acetates and trimethoxyborane with RE/B = 1 for 2 h are summarized in Table 6-3. The $REBO_3$ phase was not obtained in the reaction of RE acetate with large RE ionic size: Only $RE(OAc)_2(OH)$ [17] was obtained for La. Mixtures of RE(OAc)O, $REBO_3$ and the amorphous phase were obtained for Sm and Eu. Mixtures of $REBO_3$ and the amorphous phase were obtained for Gd-Er, while $REBO_3$ was formed as the sole product for Tm, Yb and Y (Fig. 6-8 and Table 6-3). Figure 6-9 and Tables 6-4 and 6-5 show the results for Rietveld analysis of the as-synthesized product obtained by the reaction of ytterbium acetate and trimethoxyborane. The product was comprised of two $YbBO_3$ phases with the $P6_3/m$ and $R\bar{3}c$ space groups [22]. The refinement led to residual values of Rwp = 12.26 %, Rp = 8.95 %, Re = 2.45 % and S = 5.01. The mass fractions of the $P6_3/m$ and $R\bar{3}c$ phases were 77 and 23 %, respectively. The unit cell parameters of a and c axes of the $P6_3/m$ phase were 3.751 and 8.790 Å and those of a and c axes of the $R\bar{3}c$ phase were 4.933 and 16.371 Å, respectively. The calculated densities of the $P6_3/m$ and $R\bar{3}c$ phases were 7.19 and 6.69 g/cm^3, respectively, suggesting that the $P6_3/m$ phase has higher thermodynamical stability than the $R\bar{3}c$ phase. The $P6_3/m$ phase was obtained for Sm-Er and Y, while mixtures of the $P6_3/m$ and $R\bar{3}c$ phases were obtained for Tm and Yb.

The morphology of the product is shown in Fig. 6-10. The product obtained for Eu was composed of yarn-ball-like particles, but irregularly-shaped particles were also observed. In the product for Ho, a large number of hexagonal plate particles was

Table 6-3 Phase formed by reaction of rare earth acetate and trimethoxyborane at 315 °C[a, b)]

Reaction time	La	Nd	Sm	Eu	Gd	Tb	Dy, Ho	Er	Tm	Yb	Y
2 h	$La(OAc)_2(OH)$	-	P, A, Ac	P, A, Ac	P, A	A	P, A	P, A	P, R, U	P, R	P
6 h	$La(OAc)_2(OH)$	P, A, Ac	P, A	P	P	P	P	P, R	P, R, U	P, U	P

a) Phase determined by XRD.

b) P, $REBO_3$ with $P6_3/m$ space group; R, $REBO_3$ with $R\bar{3}c$ space group; A, amorphous; Ac, RE(OAc)O; U, unknown phase.

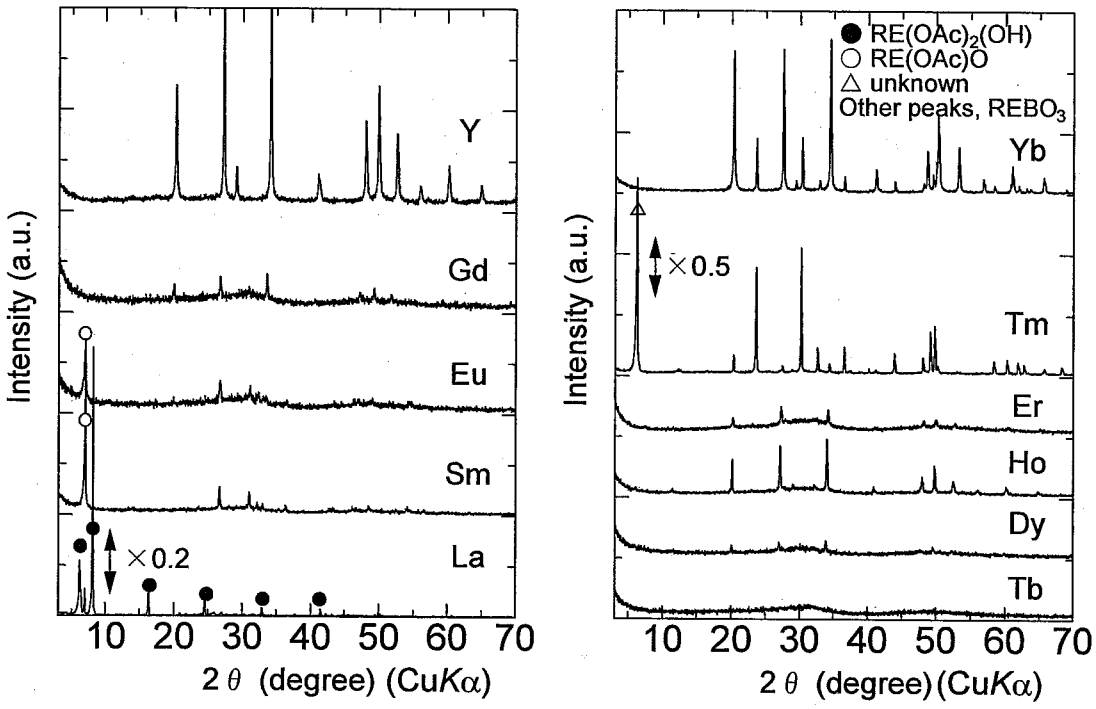

Fig. 6-8. XRD patterns of the products as-synthesized by the glycothermal reaction of RE acetates and trimethoxyborane with RE/B = 1 in 1,4-BG at 315 °C for 2 h.

Table 6-4 Crystallographic data of $YbBO_3$ obtained by glycothermal method

Element	Site	g[a)]	x	y	z	B[b)]
Oa	4f	1	0.667	0.333	0.095	1.0
Ob	6h	1/3	0.850	-0.214	0.250	1.0
B	6h	1/3	0.584	0.417	0.250	1.5
Yb	2b	1	0	0	0	0.4

Space group $P\,6_3/m$ (No. 176).

a) Site Occupacy.

b) Isotropic displacement parameter.

Table 6-5 Crystallographic data of $YbBO_3$ obtained by glycothermal method

Element	Site	g[a)]	x	y	z	B[b)]
O	18e	1	0.698	0	0.250	1.0
B	6a	1	0	0	0.250	1.5
Yb	6b	1	0	0	0	0.4

Space group $R\bar{3}c$ (No. 167).

a) Site Occupacy.

b) Isotropic displacement parameter.

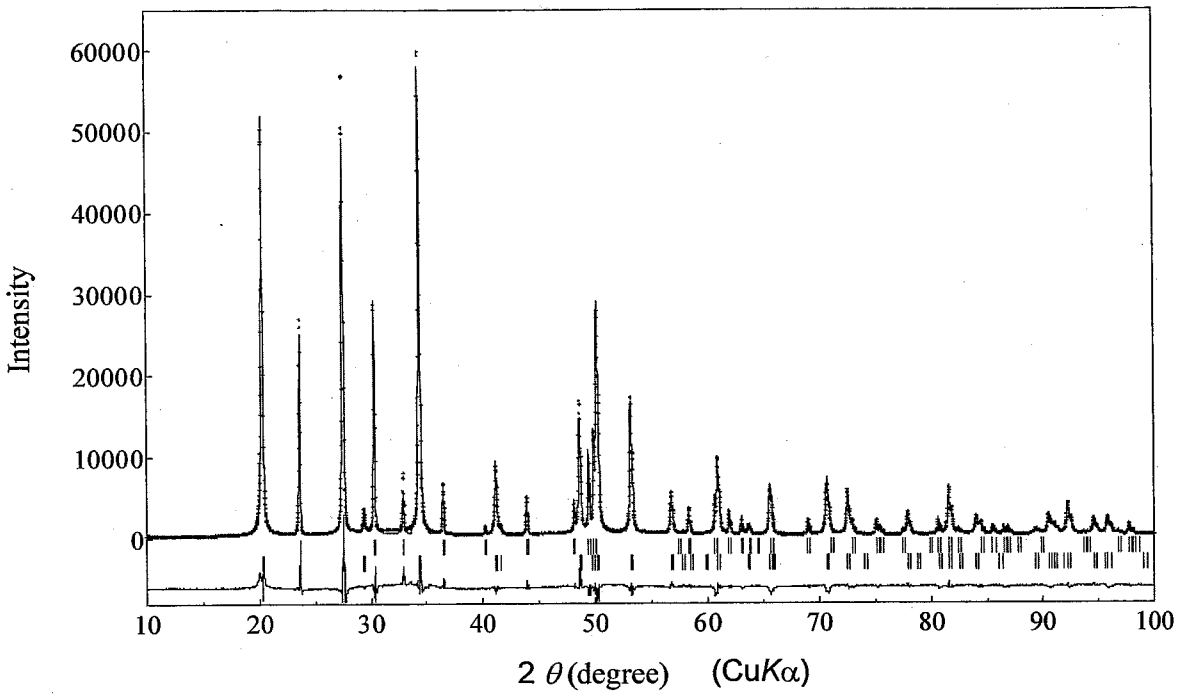

Fig. 6-9. Observed, calculated, and difference patterns obtained by Rietveld analysis of $YbBO_3$ as synthesized by glycothermal method at 315 °C for 2 h.

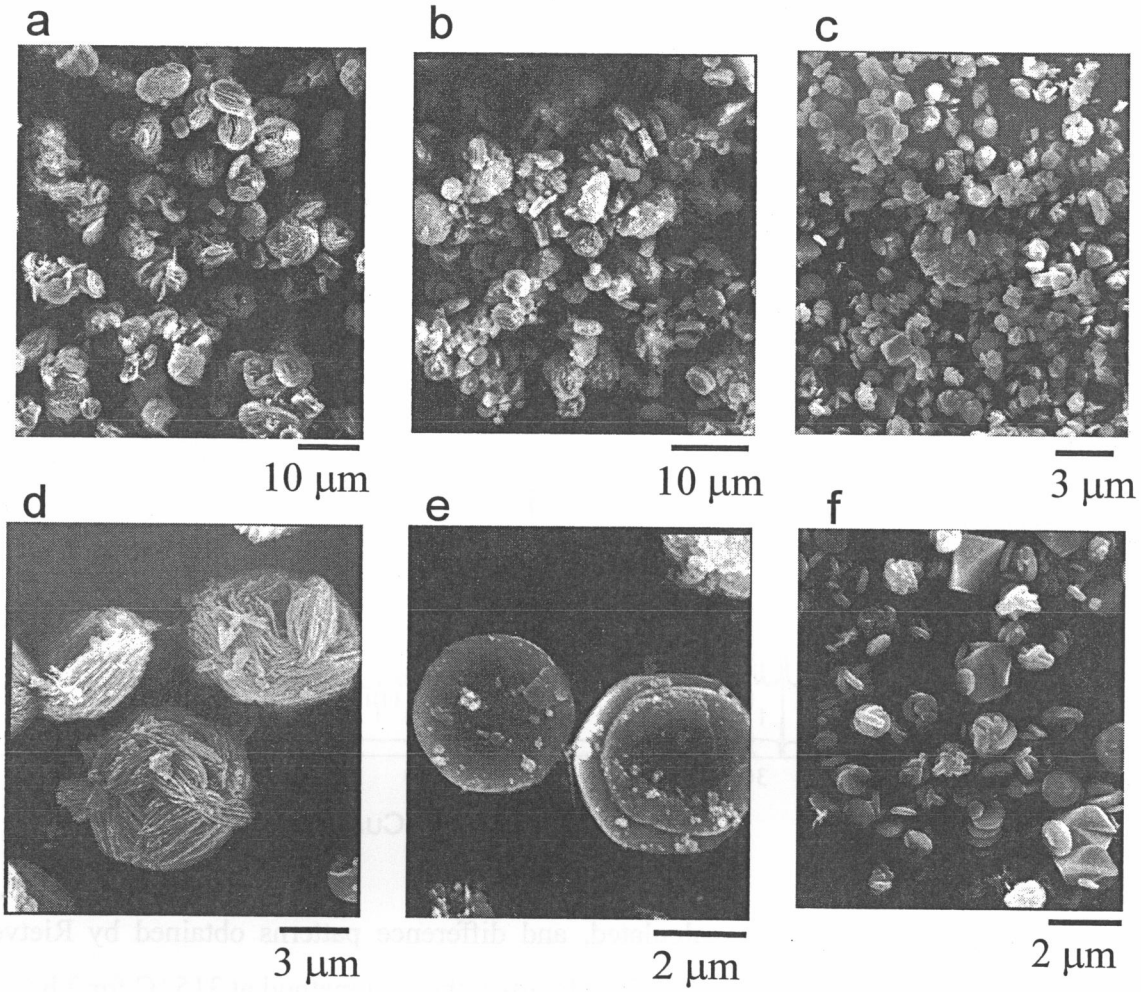

Fig. 6-10. SEM image of $REBO_3$ as synthesized by glycothermal method at 315 °C for 2 h: (a, d), Eu; (b, e), Ho; (c, f), Yb.

observed. The product obtained for Yb was composed of aggregates of disks and irregularly-shaped polyhedrons, the latter of which seems to be due to the $R\bar{3}c$ $REBO_3$ phase.

Prolonged reaction time increased the yield of $REBO_3$ with the $P6_3/m$ space group. The reaction of RE acetate and trimethoxyborane with RE/B = 1 for 6 h yielded $RE(OAc)_2(OH)$ without $REBO_3$ for La; Nd(OAc)O, $REBO_3$, and the amorphous phase for Nd; $REBO_3$ and the amorphous phase for Sm; and $REBO_3$ for Eu-Yb and Y (Fig. 6-11 and Table 6-3). The space group of $REBO_3$ was $P6_3/m$ for Nd-Ho, Yb and Y, and the mixture of $P6_3/m$ and $R\bar{3}c$ were detected for Er and Tm. For the Yb product, the peaks due to the $R\bar{3}c$ phase disappeared by prolonged reaction time, indicating that the phase transformed into the more stable $P6_3/m$ phase.

The morphologies of the products are shown in Fig. 6-12. The product obtained for Eu was composed of spheroidal particles with hexagonal-pyramidal crater and small irregularly-shaped particles were also observed. In the Ho product, hexagonal plates and spheroidal particles with the crater were observed. The Yb product was composed of aggregates of hexagonal plate particles. The Y product was composed of spheroidal particles (particle size; 3 μm) with the hexagonal-pyramidal crater. Enlargement of the particle size with the prolonged reaction indicates that Ostwald ripening took place during the glycothermal treatment.

In a previous paper, the mechanisms for the crystallization of RE gallium garnet [23] in glycothermal reaction were discussed. Based on the arguments, the following scheme is proposed for the formation of $REBO_3$: The important step for the glycothermal reaction is the heterolytic cleavage of the C-O bond of $HO(CH_2)_n$-O-B< formed by the alkoxyl exchange reaction between trimethoxyborane and glycol; when 1,4-BG (n = 4) was used, the cleavage of the C-O bond in $HO(CH_2)_n$-O-B< was facilitated by participation of the intramolecular hydroxyl group. The O^- anion formed by the

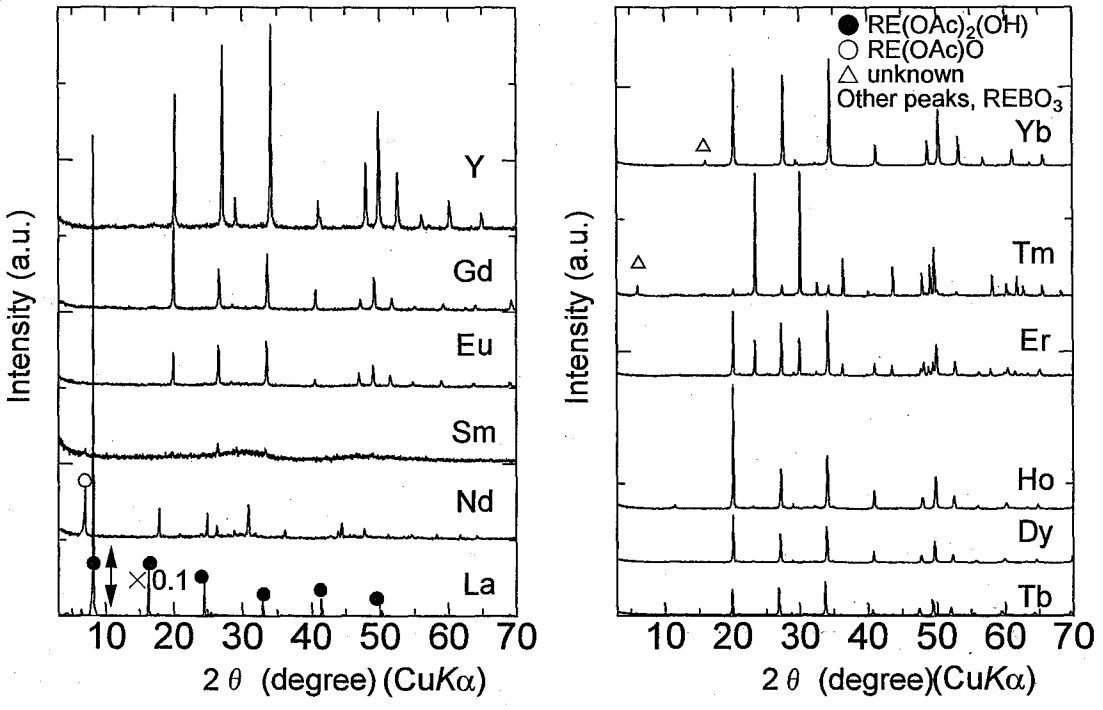

Fig. 6-11. XRD patterns of the products as synthesized by the glycothermal reaction of RE acetates and trimethoxyborane with RE/B = 1 in 1,4-BG at 315 °C for 6 h.

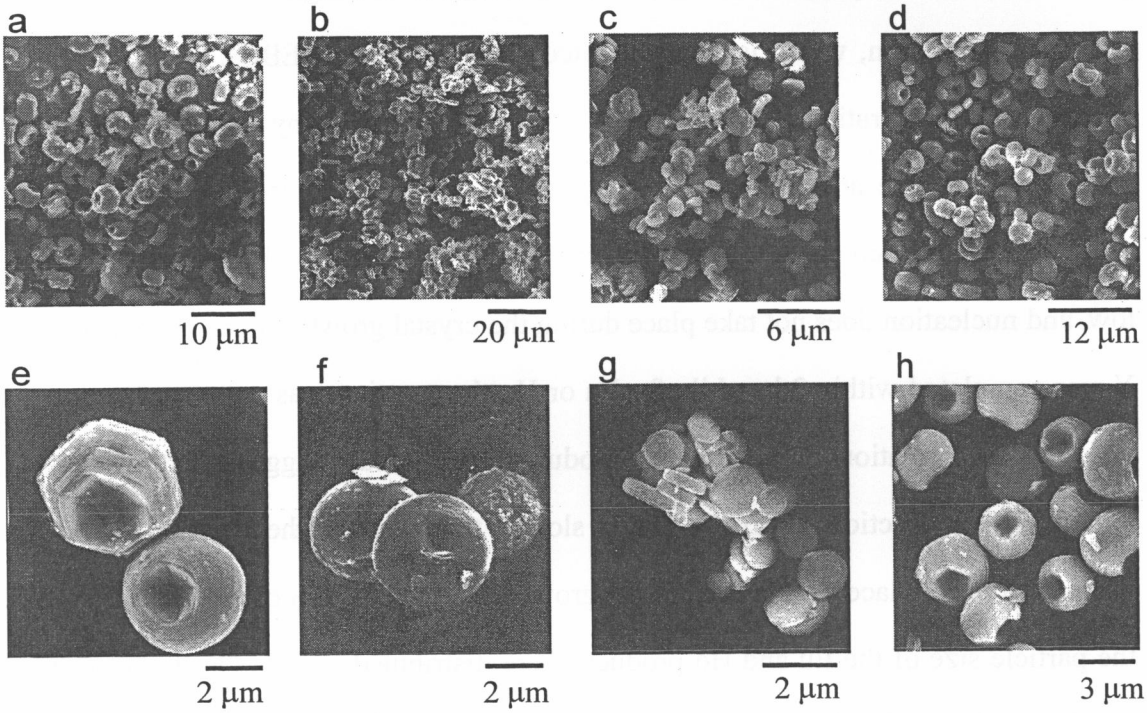

Fig. 6-12. SEM image of $REBO_3$ as synthesized by glycothermal method at 315 °C for 6 h: (a, e), Eu; (b, f), Ho; (c, g), Yb; (d, h), Y.

heterolytic cleavage of the C-O bond reacts with RE^{3+} ion, and the RE-O-B bond is formed. In the present reaction, RE-O-B was not formed for larger RE ions with lower Coulomb force.

Mono-dispersed particles can be prepared if a burst of nucleation takes place at the early stage of the reaction and if nucleation does not take place during the crystal growth stage. In the present reaction, nucleation occurs at a high concentration level of reactants in solution, which is supersaturated with respect to $REBO_3$. Once nucleation occurs, the concentration level decreases, which is determined by the balance between the dissolution rate and the rate consumption of the reactants in the solution by the crystal growth. When crystals grow rapidly, the concentration of the reactants becomes low, and nucleation does not take place during the crystal growth stage. The reaction for Y was completed within 2 h, while for Eu or Ho the reaction was not completed in 2 h resulting in formation of amorphous products. This result suggests that the crystal growth in the reaction of Eu or Ho is slower than that in the reaction of Y. The nucleation takes place during the crystal growth stage of $EuBO_3$ or $HoBO_3$. Therefore, the particle size of the Eu and Ho products were distributed widely. On the other hand, rapid crystal growth of YBO_3 decreases the concentration of the reactant in the solution, thus facilitating the formation of mono-dispersed particles.

6.4 Conclusions

The glycothermal reaction of the RE acetates with trimethoxyborane (RE/B = 1) at 315 °C for 2 h yielded phase-pure $REBO_3$ for Tm, Yb and Y. For Gd-Er, $REBO_3$ was contaminated with amorphous product. Mixtures of RE(OAc)O, $REBO_3$ and amorphous products were obtained for Sm and Eu, while only $RE(OAc)_2(OH)$ was obtained for La. The space group of the $REBO_3$ crystal obtained from Sm-Er and Y was $P6_3/m$, and mixture of $REBO_3$ crystals with $P6_3/m$ and $R\bar{3}c$ were obtained for Tm and Yb.

Prolonged reaction time (6 h) yielded $REBO_3$ without contamination of the amorphous product or RE(OAc)O for Eu-Yb, Y. For the reaction of yttrium acetate and trimethoxyborane with Y/B ratio of 1/3-3/1 for 2 h, YBO_3 was only the binary oxide detected. The YBO_3 particles were spheroidal with a diameter of 1 μm. The selected area electron diffraction of a whole particle indicated that the each particle is a "single crystal" of YBO_3 grown from one nucleus.

References

[1] C. R. Ronda, T. Jüstel and H. Nikol, J. Alloys Compd., 275-277 (1998) 669.

[2] Z. Li, J.Zeng, C. Chen and Y. Li, J. Cryst. Growth, 286 (2006) 487.

[3] S. Lemanceau, G. Bertrand-Chadeyron, R. Mahiou, M. El-Ghozzi, J. C. Cousseins, P. Conflsnt and R. N. Vannier, J. Solid State Chem., 148 (1999) 229.

[4] K. N. Kim, H.-K. Jung, H. D. Park and D. Kim, J. Mater. Res., 17 (2002) 907.

[5] M. Tukia, J. Hölsä, M. Lastusaari and J. Niittykoski, Opt. Mater., 27 (2005) 1516.

[6] D.-S. Kim and R.-Y. Lee, J. Mater. Sci., 35 (2000) 4777.

[7] D. Boyer, G. Bertrand-Chadeyron, R. Mahiou, L. Lou, A. Brioude and J. Mugnier, Opt. Mater., 16 (2001) 21.

[8] D. Boyer, G. Bertrand-Chadeyron, R. Mahiou, C. Caperaa and J.-C. Cousseins, J. Mater. Chem., 9 (1999) 211.

[9] Z. Wei, L. Sun, C. Liao, J. Yin, X. Jiang, C. Yan and S. Lü, J. Phys. Chem. B 106 (2002) 10610.

[10] Z.-G. Wei, L.-D. Sun, C.-S. Liao, X.-C. Jiang and C.-H. Yan, J. Mater. Chem., 12 (2002) 3665.

[11] X.-C. Jiang, L.-D. Sun, W. Feng and C.-H. Yan, Cryst. Growth Des., 4 (2004) 517.

[12] T. Kim and S. Kang, Mater. Res. Bull., 40 (2005) 1945.

[13] X.-C. Jiang, C.-H. Yan, L.-D. Sun, Z.-G. Wei and C.-S. Liao, J. Solid State Chem., 175 (2003) 245.

[14] X.-C. Jiang, L.-D. Sun and C.-H Yan, J. Phys. Chem. B 108 (2004) 3387.

[15] J. Zhang and J. Lin, J. Cryst. Growth 271 (2004) 207.

[16] F. Izumi and T. Ikeda, Mater. Sci. Forum, 321-324 (2000) 198.

[17] M. Inoue, T. Nishikawa, H. Kominami and T. Inui, J. Mater. Sci., 35 (2000) 1541.

[18] D. Boyer, G. Bertrand-Chadeyron, R. Mahiou, A. Brioude and J. Mugnier, Opt. Mater., 24 (2003) 35.

[19] J. H. Lin, S. Zhou, L. Q. Yang, G. Q. Yao and M. Z. Su, J. Solid State Chem., 134 (1997) 158.

[20] G. Chadeyron, M. El-Ghozzi, R. Mahiou, A. Arbus and J. C. CousseinsS, J. Solid State Chem., 128 (1997) 261.

[21] A. Nakamura, N. Namba and H. Saitoh, Sci. Technol. Adv. Mater., 6 (2005) 210.

[22] J. R. Cox and D. A. Keszler, Acta Cryst., C50 (1994) 1857.

[23] M. Inoue, T. Nishikawa, H. Otsu, H. Kominami and T. Inui, J. Am. Ceram. Soc., 81 (1998) 1173.

Chapter 7

Defect structure and morphology of rare earth aluminium garnet obtained by glycothermal reaction

7.1 Introduction

The unit cell of rare earth aluminium garnet (REAG, $RE_3Al_5O_{12}$) consists of Al atoms in 16a and 24d sites, RE atoms in 24c sites, and O atoms in 96h sites. The stability of the garnet phase depends on the ionic size of the RE element, and garnets were reported to be thermodynamically stable for the RE elements from Tb to Lu and Y. Among REAGs, yttrium aluminium garnet (YAG) has been extensively studied because it is now widely used in lasers or phosphors [1,2].

Hydrothermal synthesis of YAG powder usually requires severe conditions (350-600 °C and 30-100 MPa) [3,4]. Inoue et al. have found that the glycothermal reaction in 1,4-butanediol directly yielded nanocrystalline REAG (RE = Gd-Lu, Y) at moderate reaction conditions (300 °C and 5 MPa) [5]. Recently, optical-telecommunication-band fluorescence properties of YAG:Er^{3+} [6] and photoluminescence properties of YAG:Ce^{3+} [7,8] nanocrystals prepared by the glycothermal method have been reported.

In this chapter, the author deals with the defect structure and the morphology of REAG synthesized by the glycothermal reaction.

7.2 Experimental

Aluminium isopropoxide (AIP, 4.27 g, 20.8 mmol) and yttrium acetate tetrahydrate (YAc, 4.24 g, 12.5 mmol) were suspended in 90 ml of 1,4-butanediol (1,4-BG) in a test tube, serving as autoclave liner, and the mixture was placed in a 200-ml autoclave. An additional 25 ml of 1,4-BG was placed in the gap between the autoclave wall and the test tube. The autoclave was purged with nitrogen, heated to 300 °C at a rate of 2.3

°C/min, and kept at that temperature for 2 h. After the assembly was cooled to room temperature, the resulting products were centrifuged. The sedimented part of the product was washed repeatedly with methanol by vigorous mixing and centrifuging, and then dried in air. This product was designated as P(Y-a). The supernatant (milky white suspension) and all the washings were gathered together, and a concentrated ammonium hydroxide solution was added to sediment the particles. This product was repeatedly washed with methanol and dried in air (designated as P(Y-b)). For calcination, the products were heated at a rate of 5 °C/min and held at 1000 °C for 30 min in a box furnace. The calcined product was designated as P(RE-a-cal). In the reaction of gadolinium acetate and AIP, 10 ml of the supernatant (YAG; about 0.1 g) obtained by the glycothermal reaction of yttrium acetate and AIP was added to test tube as seed crystals.

X-ray powder diffraction (XRD: Shimadzu XD-D1) was recorded using Cu*K*α radiation. The crystallite sizes of REAG were calculated from the half-height width of the 211 diffraction peak at 18° by Scherrer equation. For Rietveld analysis, the XRD pattern was measured on another diffractometer (Rigaku Rint 2500) and analyzed by RIETAN-2000 program [9]. The morphology of the products was observed with a transmission electron microscope (TEM), Hitachi H-800, operated at 200 kV.

7.3 Results and discussion

The XRD patterns of the as-synthesized products in the sedimented and supernatant parts are shown in Figs. 7-1a and 1b, respectively. Phase-pure REAGs were detected for P(Y-b) and P(Yb-b), but P(Y-a) and P(Yb-a) were contaminated with the glycol derivative of boehmite ($AlO(OH)_x(O(CH_2)_4OH)_{1-x}$) and RE(OAc)O [10,11]. An amorphous product was obtained for Gd, when the reaction was carried out without the seed crystals. This result can be attributed to the fact that GdAG does not appear in the

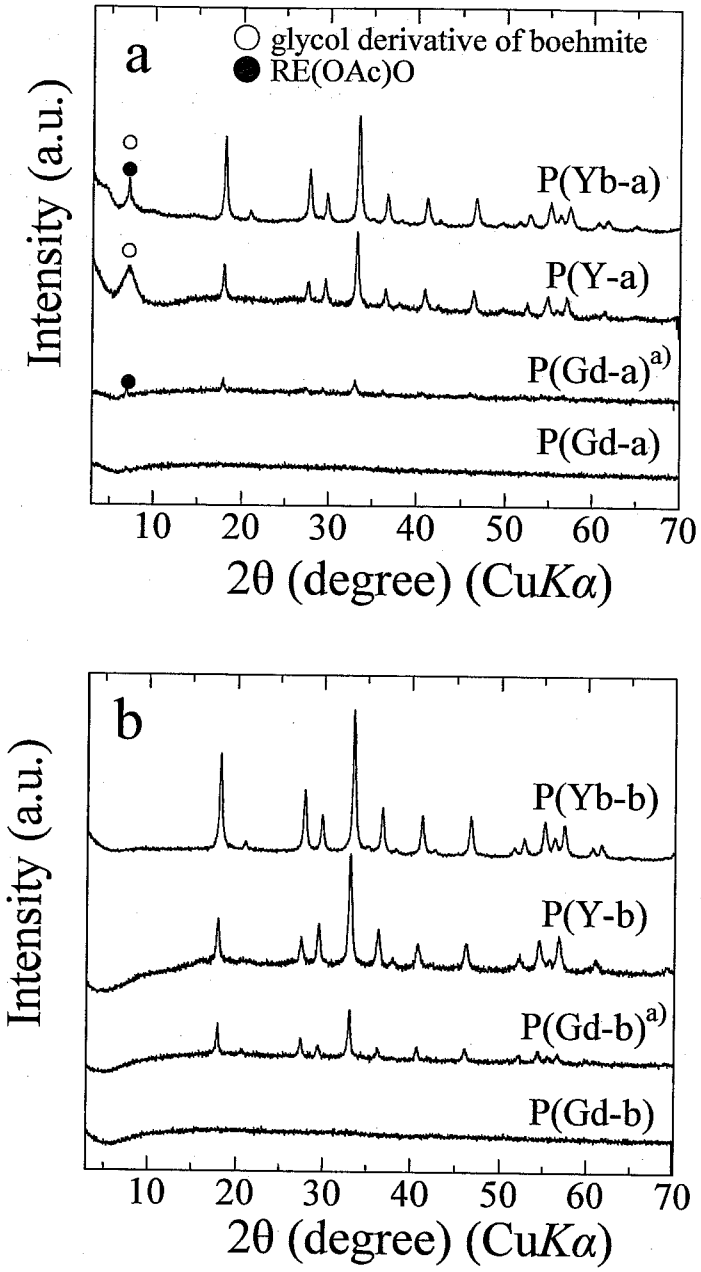

Fig. 7-1. XRD patterns of the as-synthesized products: a, sedimented part of the product; b, product in the suparnant.

a) The product was synthesized in the presence of seed crytals of YAG.

Gd_2O_3-Al_2O_3 phase diagrams [13]. However, GdAG was crystallized together with Gd(OAc)O when the reaction was carried out in the presence of the seed crystals of YAG. This result indicates that the nucleation step is difficult process while crystal growth takes place much easily under the glycothermal conditions.

Table 7-1 summarized the phases detected by XRD analysis of the as-synthesized and calcined products. The amorphous phase and Gd(OAc)O in P(Gd-a) transformed into $Gd_4Al_2O_9$ and $GdAlO_3$ by calcination. P(Gd-b-cal) was composed of GdAG and small amounts of YAG (seed crystals) and $Gd_4Al_2O_9$. The glycol derivative of boehmite and Yb(OAc)O were decomposed into γ-Al_2O_3 and Yb_2O_3, respectively, by calcination. P(Y-b-cal) and P(Yb-b-cal) were phase pure garnets and no other phases were detected.

Since P(RE-a) and P(RE-a-cal) were contaminated with the phases other than garnet, TEM observation and Rietveld analysis were carried out for P(RE-b) and P(RE-b-cal). The TEM images of these products are shown in Fig. 7-2. The observed particle sizes (P(Gd-b), 50–100 nm; P(Y-b), 20–50 nm; P(Yb-b), 20–50 nm) were slightly larger than the crystallite sizes (43, 28, and 30 nm, respectively). The higher magnification images of the REAG particles indicated that many voids were presented in the particle. For crystal growth in the glycothermal reaction in 1,4-BG, the following scheme was proposed [12]: crystal growth takes place by stepwise decomposition of surface ω-hydroxybutyl groups into protonated tetrahydrofuran remaining O-anion on the growing surface. Coulomb interaction between O-anion and RE^{3+} ion in the glycol solution creates a new RE-O-Al bond and the crystal grows. Because the decomposition of the ω-hydroxybutyl group occurs statistically irrespective of the location of the group, some glycol moieties remain and form defects. Once such defects form, they are apt to form voids and crevices. Therefore, BET surface area (80 m^2/g) of P(Y-b) was much larger than the value (47 m^2/g) calculated assuming that each YAG particle is spherical with a diameter of 28 nm (crystallite size).

Table 7-1 Phases detected by XRD analysis

Sample	Phases	Sample	Phases
P(Gd-a)[a)]	amrphous, GdAG, Gd(OAc)O	P(Gd-a-cal)[a), b)]	GdAG, $Gd_4Al_2O_9$, $GdAlO_3$
P(Gd-b)[a)]	GdAG, YAG	P(Gd-b-cal)[a), b)]	GdAG, YAG, $Gd_4Al_2O_9$
P(Y-a)	YAG, boehmite[c)]	P(Y-a-cal)	YAG, γ-Al_2O_3
P(Y-b)	YAG	P(Y-b-cal)	YAG
P(Yb-a)	YbAG, Yb(OAc)O, boehmite[c)]	P(Yb-a-cal)	YbAG, γ-Al_2O_3, Yb_2O_3
P(Yb-b)	YbAG	P(Yb-b-cal)	YbAG

a) The product was synthesized in the presence of seed crytals of YAG.

b) The product was calcined at 1200 °C for 30 min.

c) Glycol derivative of boehmite

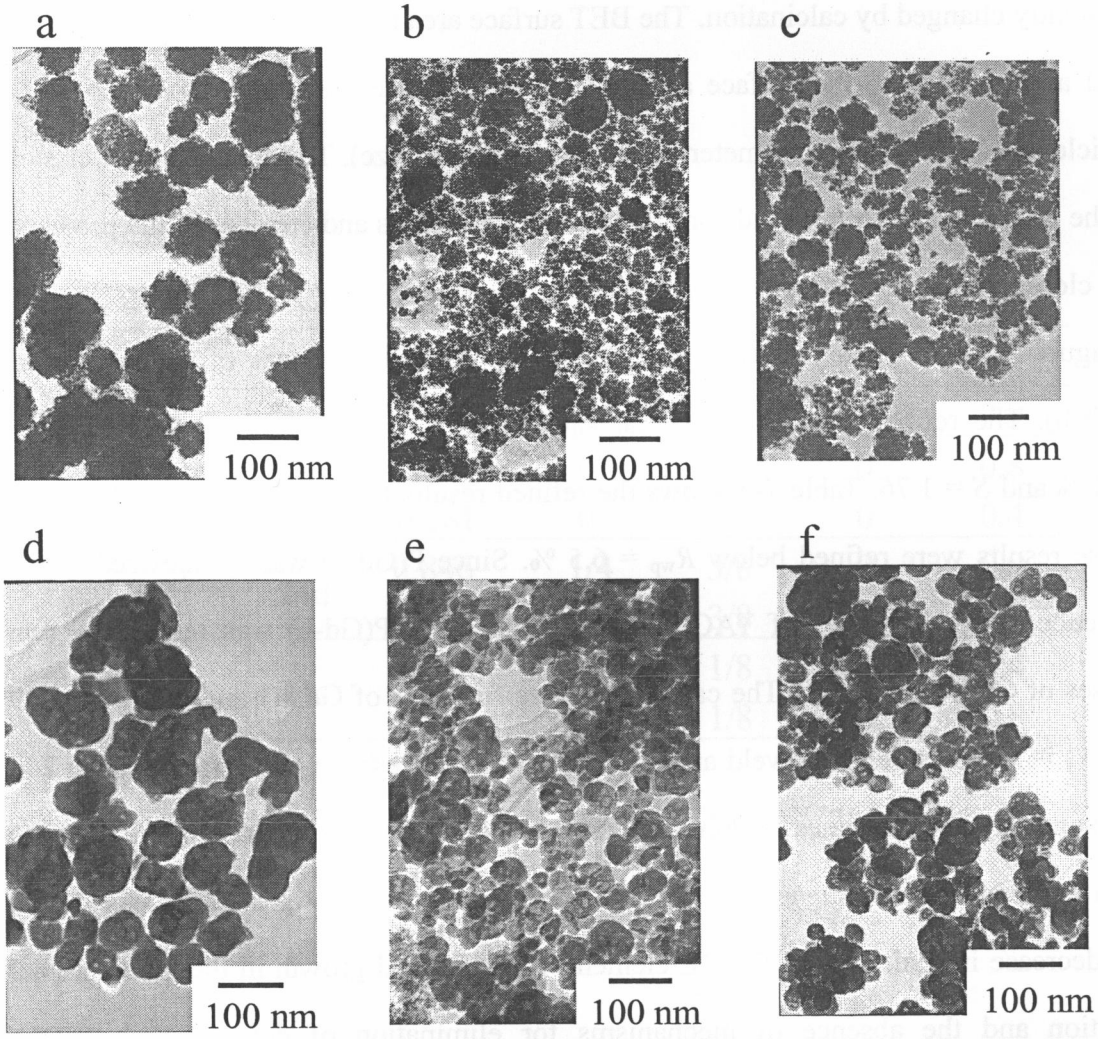

Fig. 7-2. TEM images of the products: a, P(Gd-b) synthesized in the presence of seed crystals of YAG; b, P(Y-b); c, P(Yb-b); d, P(Gd-b-cal); e, P(Y-b-cal); and f, P(Yb-b-cal).

P(Gd-b-cal), P(Y-b-cal) and P(Yb-b-cal) were composed of spherical particles of REAGs with the diameters of 45–100, 30–50 and 30–50 nm, respectively. The crystallite sizes of REAGs (GdAG; 46 nm, YAG; 31 nm, YbAG; 36 nm) were not apparently changed by calcination. The BET surface area (35 m^2/g) of P(Y-b-cal) was in good agreement with the surface area (43 m^2/g) calculated assuming that each YAG particle is spherical with a diameter of 31 nm (crystallite size). The spherical particles of all the products had closed voids originating from the voids and crevices in the products. The closed voids were enlarged by calcination.

Figure 7-3 and Table 7-2 show the results for Rietveld analysis of as-synthesized P(Yb-b). The refinement led to residual values of R_{wp} = 4.71 %, R_p = 3.71 %, R_e = 2.68 % and S = 1.76. Table 7-3 shows the refined results for P(RE-b) and P(RE-b-cal). These results were refined below R_{wp} = 6.5 %. Since P(Gd-b) was synthesized in the presence of seed crystals of YAG, the XRD pattern of P(Gd-b) was refined by two phases of GdAG and YAG. The calculated mass fractions of GdAG and YAG were 69 and 31 %, respectively. Rietveld analysis indicated the presence of Al vacancies in 24d sites and oxygen vacancies in 96h sites, and partial substitution of Al ions in 16a sites with RE ions was also suggested. The occupancy of RE ions in 16a sites increased with the decrease in ionic size of the RE element. Rapid crystal growth in the glycothermal reaction and the absence of mechanisms for elimination of defects, such as the dissolution-crystallization mechanism operating in hydrothermal reactions, are the reasons for a number of defects in REAG crystals synthesized in 1,4-BG (P(RE-b)).

The unit cell parameters of as-synthesized REAGs were much larger than the values (GdAG, 12.11 Å; YAG, 12.01 Å; YbAG, 11.93 Å) reported in the JCPDS cards. The enlargement of the unit cell parameter can be attributed to the substitution of Al ions in 16a sites with RE ions. Another factor is presumably the presence of many voids in REAGs. Lattice expansion has been reported for various nonmetallic fine particle

Table 7-2 Crystallographic data of P(Yb-b)

Element	Site	g[a)]	x	y	z	B[b)]
O	96h	0.942	0.0322	0.0528	0.6499	0.9
Al	16a	0.819	0	0	0	0.8
Yb		0.181	0	0	0	0.4
Al	24d	0.846	1/4	3/8	0	0.9
Yb		0	1/4	3/8	0	0.8
Yb	24c	1	1/4	1/8	0	0.4
Al		0	1/4	1/8	0	0.8

Space group $Ia\bar{3}d$ (No. 230)

a) Site occupacy

b) Isotropic displacement parameter

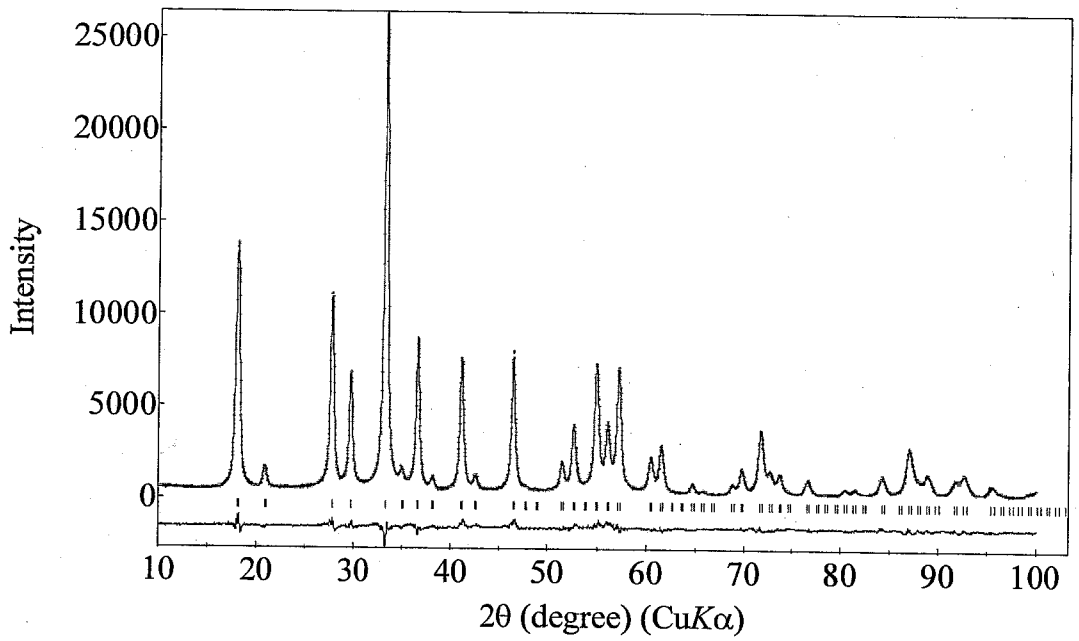

Fig. 7-3. Observed, calculated, and difference patterns obtained by Rietveld analysis of P(Yb-b).

Table 7-3 Results for Rietveld analysis of REAGs obtained by the glycothermal method with/without subsequent calcination.

Sample	Ionic size of RE^{3+} (Å)	Site occupacy							Unit cell parameter (Å)	RE/Al	R_{wp}
		96h	16a		24d		24c				
		O	Al	RE	Al	RE	RE	Al			
P(Gd-b)[a)]	0.938	0.906	0.979	0.021	0.748	0	0.971	0.029	12.141	3/4.36	6.30
P(Y-b)	0.900	0.888	0.940	0.060	0.701	0	0.810	0.190	12.144	3/5.36	4.39
P(Yb-b)	0.868	0.942	0.819	0.181	0.846	0	1	0	12.106	3/3.73	4.71
P(Gd-b-cal)[a)]	0.938	1	0.872	0.128	1	0	1	0	12.144	3/4.37	5.85
P(Y-b-cal)	0.900	1	0.773	0.227	1	0	1	0	12.110	3/3.95	6.27
P(Yb-b-cal)	0.868	1	0.750	0.250	1	0	1	0	12.075	3/3.86	6.03

a) The product was synthesized in the presence of seed crytals of YAG.

systems, and is explained by surface hydroxyl groups [18]. In the present case, many voids with the surface alkoxyl groups in the as-synthesized P(RE-b) may also contribute to the large unit cell parameter.

P(Gd-b-cal) was refined by three phases of GdAG, $Gd_4Al_2O_9$ and YAG. The mass fractions of GdAG, YAG and $Gd_4Al_2O_9$ were 75, 14, and 11 %, respectively. In P(RE-b-cal), Al vacancies in 24d sites and oxygen vacancies disappeared, while the ratio of substitution of Al ions in 16a sites with RE ions became higher than that in as-synthesized P(RE-b). The population of RE ions in 16a sites increased with the decrease of RE ionic size. The unit cell parameters of P(RE-b-cal) were much larger than the value (12.01 Å) reported in the JCPDS cards.

Effects of charged RE/Al ratios on the RE population in 16a sites were investigated by Rietveld analysis of the calcined samples (Fig. 7-4). Although some products were contaminated with small amounts of the monoclinic and oxide phases and YAG used as the seed crystals, the multi phase analysis was carried out for these samples. The RE population in 16a sites increased with the increase in the RE/Al ratio charged for the glycothermal reaction and with the decrease in ionic size of RE element, and the highest population, 47 %, was observed for P(Yb/Al = 45/55-b-cal). Although the population decreased with the decrease in the charged RE/Al ratio, the substitution of Al ions with RE ions was also observed for the products with Al rich composition, P(RE/Al = 30/70-b-cal). The unit cell parameter increased with the increase in the RE population in 16a sites. However, the substitutions of Al ions in 24d sites with RE ions and RE ions in 24c sites with Al ions and oxygen vacancies were not detected for these calcined samples.

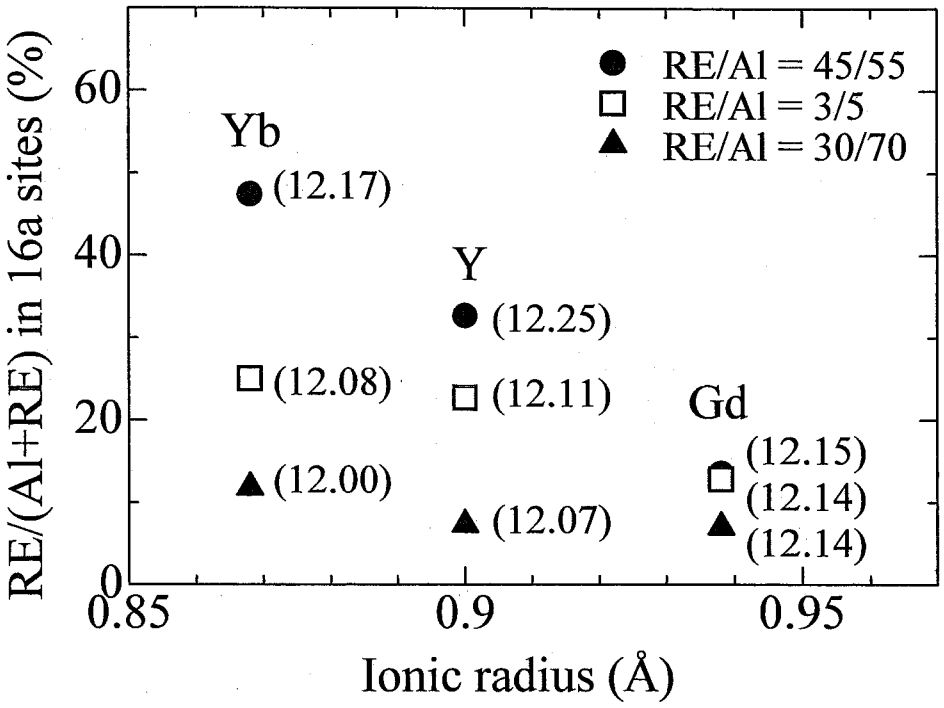

Fig. 7-4. Substitution ratio of Al ions in 16a sites with RE ions in P(RE-b-cal) synthesized with various charged RE/Al ratios and calcined at 1000 °C. Unit cell parameter of the product was given in parentheses (Å). P(Gd-b-cal) was synthesized in the presence of seed crystals of YAG.

7.4 Conclusions

$Gd_3Al_5O_9$, $Y_3Al_5O_{12}$ and $Yb_3Al_5O_{12}$, having the particle size of 50-120, 30-50 and 30-50 nm, respectively, were prepared by glycothermal reaction. Rietveld analysis indicated the presence of Al vacancies in 24d sites and oxygen vacancies in 96h sites, and partial substitution of Al ions in 16a sites with RE ions was also suggested. The occupancy of RE ions in 16a sites increased with the decrease in ionic size of the RE element. The unit cell parameters of REAGs were larger than the values reported in JCPDS cards. REAG with small RE ionic size obtained by glycothermal reaction and subsequent calcination had a large population of RE ions in 16a sites, which caused an enlargement of the unit cell parameter.

References

[1] G. Xia, S. Zhou, J. Zhang, S. Wang, Y. Liu, J. Xu, J. Cryst. Growth, 283 (2005) 257.

[2] Y. Hakuta, K. Seino, H. Ura, T. Adschiri, H. Takizawa, K. Arai, J. Mater. Chem., 9 (1999) 2671.

[3] T. Takamori and L. D. David: Am. Ceram. Soc. Bull. Vol. 65 (1986), p. 1282

[4] Y. Hakuta, K. Seino, H. Ura, T. Adschiri, H. Takizawa and K. Arai: J. Mater. Chem. Vol. 9 (1999), p. 2671

[5] M. Inoue, H. Otsu, H. Kominami, T. Inui, J. Alloys Compd., 226 (1995) 146.

[6] M. Nishi, S. Tanabe, M. Inoue, M. Takahashi, K. Fujita, K. Hirao, Opt. Mater., 27 (2005) 655.

[7] R. Kasuya, T. Isobe, H. Kuma, J. Katano, J. Phys. Chem. B, 109 (2005) 22126.

[8] R. Kasuya, T. Isobe, H. Kuma, J. Alloys Compd., 408-412 (2006) 820.

[9] F. Izumi, T. Ikeda, Mater. Sci. Forum, 321-324 (2000) 198.

[10] M. Inoue, H. Kominami, T. Inui, Nippon Kagaku Kaishi, (1991) 3331.

[11] H. Kominami, M. Inoue, T. Inui, Nippon Kagaku Kaishi, (1993) 605.

[12] M. Inoue, T. Nishikawa, H. Otsu, H. Kominami, T. Inui, J. Am. Ceram. Soc., 81 (1998) 1173.

[13] M. Mizuno, T. Yamada, T. Noguchi, Yogyo Kyokaishi, 85 (1977) 543.

General Conclusion

The author investigated and discussed the syntheses and physical properties of rare earth (RE) oxides and mixed oxides obtained by solvothermal reactions in organic media (e.g., 2-methoxyethanol, 2-aminoehanol, or various glycols).

Chapter 1 deals with the reactions of RE metals in 2-methoxyethanol and 2-aminoethanol. The reactions of Ce, Sm, and Yb metals in 2-methoxyethanol and 2-aminoethanol yield colloidal solutions of CeO_2, Sm_2O_3, and Yb_2O_3 particles. Transparent colloidal solutions of Y, Eu, Gd, and Tb are obtained by the reaction in 2-methoxyethanol containing a small amount of acetic acid. The reaction mechanism is as follows. The RE metals are highly active, and they are flammable when fresh surfaces are exposed to moist air. In the present experiments, metal chips with oxide layers were used. The superficial layers must be removed before the reaction occurs. The addition of acetic acid or 2-aminoethanol whose polarity is higher than that of 2-methoxyethanol facilitates the dissolution of the superficial layers. The removal of these layers at high temperatures causes a very rapid reaction of the RE metal with the solvent alcohol.

$$2RE + 6ROH \rightarrow 2RE(OR)_3 + 3H_2.$$

The thermal decomposition of RE alkoxide yields RE oxide according to the following reaction:

$$2RE(OR)_3 \rightarrow RE_2O_3 + 3ROR$$

The resulting high concentration of the alkoxide causes the bust nucleation of RE oxides, thereby leading to the formation of colloidal particles.

Chapter 2 deals with the reactions of RE acetate hydrates in vic-glycols. The thermal decomposition behaviors of the resulting products were investigated. The reactions of yttrium acetate hydrate in ethylene glycol, 1,2-propanediol, and 1,2-butanediol at 300

°C yields products containing the acetate group and glycol moieties, while the reaction in 1,3-propanediol and 1,4-butanediol yields yttrium acetate oxide [Y(OAc)O]. The former products are directly decomposed into Y_2O_3below 400 °C, while the latter form Y_2O_3 via yttrium carbonate oxide after calcination at 600–700 °C. The reaction of other RE acetates in 1,2-propanediol yields products with two different crystal structures depending on the ionic size of the RE elements: one structure originates from La-Nd (group A) and the other originates from Sm-Yb and Y (group B). RE_2O_3 obtained from the group A products excluding Ce is produced by the formation of RE carbonate oxide, while that obtained from the group B products excluding Sm and Eu is directly crystallized at 400 °C without the formation of RE carbonate oxide . In this regard, the RE_2O_3 (RE = Gd-Yb, Y) samples have considerably large surface areas; they have a larger surface area and smaller crystallite size than those of any other comparable compounds reported thus far.

Chapter 3 discusses the morphologies of RE_2O_3 obtained by the calcination of certain products at 400 °C; these products were synthesized by the reaction of RE acetates in 1,2-propanediol. Y_2O_3 was composed of nano-hollow spheres with outer diameters of 7–18 nm and inner diameters of 2–8 nm. Each nano-hollow sphere contained many pores between Y_2O_3 crystallites. The Y_2O_3 sample maintained its nano-hollow shape even after calcination at 500 °C; however many of its pores disappeared. Gd_2O_3 was composed of porous solids with a plate-shaped outline, and Dy_2O_3 contained porous plate-shaped particles and nano hollow spheres. Er_2O_3 and Yb_2O_3 exhibited nano-hollow sphere morphologies with outer diameters of approximately 9 and 8 nm and inner diameters of approximately 4 and 3 nm, respectively.

Chapter 4 describes the reactions of RE chloride hydrates in 1,4-butanediol at 300 °C for 2 h in the presence of small amounts of *n*-hexylamine and 1,6-hexanediamine. Phase-pure $RE(OH)_2Cl$ was obtained for La-Dy, while $RE(OH)_2Cl$ obtained for Ho-Yb

and Y was contaminated with $RE_2O_3 \cdot xH_2O$. The space group of $RE(OH)_2Cl$ formed in this reaction was $P2_1/m$ [space group No. 11]. Thermal analysis of the products in an air flow indicated that the $RE(OH)_2Cl$ phases for all RE elements excluding Ce were dehydrated into REOCl, while $Ce(OH)_2Cl$ was decomposed at 350 °C to yield CeO_2 without the formation of CeOCl. In the case of RE elements with small ionic sizes (Dy-Yb, Y), REOCl was further decomposed into RE_2O_3 by heating up to 1000 °C, while REOCl in RE elements with large ionic sizes (La-Gd) did not decompose even after calcination at 1000 °C.

The morphologies of $RE(OH)_2Cl$ and $RE_2O_3 \cdot xH_2O$ synthesized by the reaction of RE chloride hydrates in 1,4-butanediol at 300 °C in the presence of small amounts of amines are discussed in chapter 5. The reaction of RE chloride hydrates (Y, Er, and Yb) in 1,4-butanediol at 300 °C for 2 h produced a mixture of $RE(OH)_2Cl$ and $RE_2O_3 \cdot xH_2O$, and they were composed of irregularly shaped particles. Even the prolonged reaction (10 h) yielded a mixture of $RE(OH)_2Cl$ and $RE_2O_3 \cdot xH_2O$ for Er or Y; however, phase-pure $RE_2O_3 \cdot xH_2O$ was obtained for Yb. The latter comprised needle-shaped single crystals of $Yb_2O_3 \cdot xH_2O$ with a width of 0.2–0.6 μm and length of 5–15 μm. The $Yb_2O_3 \cdot xH_2O$ phase decomposed into Yb_2O_3 at 350–500 °C while preserving the needle-shaped morphology, which was maintained even after calcination at 1100 °C. Single crystals of Yb_2O_3 obtained by the calcination of $Yb_2O_3 \cdot xH_2O$ at 500 °C contained very small voids that were enlarged to a diameter of 35 Å by calcination at 800 °C.

In Chapter 6, the author discusses the glycothermal reactions of the RE acetate hydrates with trimethoxyborane (RE/B = 1) in 1,4-butanediol at 315 °C for 2 h. Phase-pure $REBO_3$ was obtained for Tm, Yb, and Y, while $REBO_3$ obtained for Gd-Er was contaminated with an amorphous product. A mixture of RE(OAc)O, $REBO_3$, and the amorphous product was obtained for Sm and Eu, while only $RE(OAc)_2(OH)$ was

obtained for La. The space group of the $REBO_3$ crystals obtained for Sm-Er and Y was $P6_3/m$, and a mixture of $REBO_3$ crystals with $P6_3/m$ and $R\bar{3}c$ was obtained for Tm and Yb. For Eu-Yb and Y, a prolonged reaction time (6 h) yielded $REBO_3$ without contamination with amorphous products or RE(OAc)O. In the reaction of yttrium acetate hydrate and trimethoxyborane with Y/B ratios of 1/3–3/1 for 2 h, YBO_3 was the only binary oxide. The YBO_3 particles were spheroidal with a mean diameter of 1 μm. The selected area electron diffraction analysis of a whole particle indicated that each particle is a "single crystal" of YBO_3 developed from a single nucleus.

The detailed crystal structure of $RE_3Al_5O_{12}$ synthesized by a glycothermal reaction is discussed in Chapter 7. The reaction of a stoichiometric mixture of aluminum isopropoxide and RE acetate hydrate in 1,4-butanediol at 300 °C directly yielded crystalline $RE_3Al_5O_{12}$. The particle sizes of $Gd_3Al_5O_{12}$, $Y_3Al_5O_{12}$ and $Yb_3Al_5O_{12}$ were 50–120 nm, 30–50 nm and 30–50 nm, respectively. The unit cell parameters of these $RE_3Al_5O_{12}$ were larger than the values reported in the JCPDS cards. Rietveld analyses of $RE_3Al_5O_{12}$ indicated the presence of Al vacancies in 24d sites and oxygen vacancies in 96h sites, and a partial substitution of Al ions in 16a sites with RE ions was suggested. The occupancy of RE ions in 16a sites increased with a decrease in the ionic size of the RE elements. Rapid crystal growth in the glycothermal reaction and the absence of mechanisms for elimination of defects, such as the dissolution-crystallization mechanism operating in hydrothermal reactions, are the reasons for a number of defects in $RE_3Al_5O_{12}$ crystals synthesized in 1,4-butanediol.

In summary, the solvothermal reaction synthesizes RE oxides and mixed oxides with small particle sizes, high surface areas, unique morphologies, and peculiar crystal structures. The author believes that the RE oxides and mixed oxides obtained by the solvothermal reaction will be applied in various fields as high-performance inorganic materials.

List of Publications

Chapter 1

"Solvothermal Reaction of Rare-Earth Metals in 2-Methoxyethanol and 2-Aminoethanol,"

T. Kobayashi, S. Hosokawa, S. Iwamoto, M. Inoue,

Journal of the American Ceramic Society 89 (2006) 1205.

Chapter 2

"Synthesis of Nanocrystalline Rare Earth Oxides by Glycothermal Method,"

S. Hosokawa, S. Iwamoto, M. Inoue,

Materials Research Bulletin, *submitted.*

Chapter 3

"Synthesis of Nano-Hollow Shaped Rare Earth Oxide by Glycothermal Treatment of Rare Earth Acetate and Subsequent Calcination,"

S. Hosokawa, S. Iwamoto, M. Inoue,

Journal of Alloys and Compounds, *submitted.*

Chapter 4

"Solvothermal treatment of rare earth chloride hydrates,"

S. Hosokawa, S. Iwamoto, M. Inoue,

Journal of Alloys and Compounds 408-412 (2006) 529.

Chapter 5

"Synthesis of Needle-shaped Rare Earth Oxide by Solvothermal Treatment of Rare

Earth Chloride,"

S. Hosokawa, S. Iwamoto, M. Inoue,

Joint 20th AIRAPT-43th EHPRG Conference on Science and Technology of High Pressure, June 27-Julu 1 (2005), Karlsruhe in Germany, Proceedings, T13-P057.

"Synthesis of Mesoporous Needle-shaped Ytterbium Oxide by Solvothermal Treatment of Ytterbium Chloride,"

S. Hosokawa, S. Iwamoto, M. Inoue,

Journal of the American Ceramic Society *in press* .

Chapter 6

"Synthesis of Rare Earth Borate ($REBO_3$) by Glycothermal Method,"

S. Hosokawa, Y. Tanaka, S. Iwamoto, M. Inoue,

Journal of Materials and Science, *submitted.*

Chapter 7

"Structure of Yttrium Aluminium Garnet obtained by the Glycothermal Method,"

S. Hosokawa, Y. Tanaka, S. Iwamoto, M. Inoue,

Advances in Science and Technology, 45 (2006) 691.

"Defect Structure of Rare Earth Aluminium Garnet obtained by the Glycothermal Method,"

S. Hosokawa, Y. Tanaka, S. Iwamoto, M. Inoue,

Journal of Alloys and Compounds, *submitted.*

The author also published following papers that are not included in this thesis.

1. **"Reduction behaivior of Ru/CeO_2 catalysts and their activity for wet oxidation,"**

   S. Imamura, Y. Taniguchi, Y. Ikeda, S. Hosokawa, H. Kanai, H. Ando,

   Reaction Kinetics Catalysis Letter 76 (2002) 201.

2. **"State of Ru on CeO_2 and its catalytic activity in the wet oxidation of acetic acid,"**

   S. Hosokawa, H. Kanai, K. Utani, Y. Taniguchi, Y. Saito, S. Imamura,

   Applied Catalalysis B: Environmental 45 (2003) 181.

3. **"Oxidation characteristics of Ru/CeO_2 catalyst,"**

   S. Hosokawa, S. Nogawa, M. Taniguchi, K. Utani, H. Kanai, S. Imamura,

   Applied Catalalysis A: General 288 (2005) 67.

4. **"Affinity order among noble metals and CeO_2,"**

   S. Hosokawa, M. Taniguchi, K. Utani, H. Kanai, S. Imamura,

   Applied Catalalysis A: General 289 (2005) 115.

5. **"Reactivity of Ru=O species in RuO_2/CeO_2 catalysts prepared by a wet reduction method,"**

   S. Hosokawa, Y. Fujinami, H. Kanai,

   Journal of Molecular Catalysis A: Chemical 240 (2005) 49.

Acknowledgements

This thesis summarizes the author's studies made in the years of 2004-2007 at the Department of Energy and Hydrocarbon Chemistry, Graduate School of Engineering, Kyoto University.

First of all, the author wishes to express the greatest gratitude to Professor Masashi Inoue for his invaluable advice and suggestion all throughout the course of this work.

The author is also grateful to Professor Koichi Eguchi and Professor Toshinobu Yoko for their kind guidance and comments to complete this thesis.

Sincere gratitude is also made to Dr. Shinji Iwamoto for his helpful discussion and encouragement.

The author studied heterogeneous catalysis under the direction of Professor Seiichiro Imamura and Professor Hiroyoshi Kanai at the Department of Chemistry, Kyoto Institute of Technology during 1998-2004. The author would like to express special thanks to them for their valuable discussion and heartwarming kindness.

All members in the Inoue Laboratory with whom the author worked together in the years of 2004-2007 and those who worked in the Imamura Laboratory during 2002-2004 are gratefully acknowledged for their kind encouragement, support, and collaboration.

Finally, the author thanks many of his friends and his family, especially his parents Takahiro and Haruko Hosokawa, for their understanding, support, and encouragement.

Saburo Hosokawa

2007